FINAL TECHNICAL REPORT

Award #06HQGR0213

BROADBAND GROUND MOTION SIMULATIONS FOR SCENARIO EARTHQUAKES IN THE SAN FRANCISCO BAY REGION

Robert Graves
URS Group Inc.
566 El Dorado Street, 2nd Floor
Pasadena, CA 91101

Tel: 626-449-7650
Fax: 626-449-3536
Email: Robert_graves@urscorp.com

FINAL TECHNICAL REPORT

Award #06HQGR0213

BROADBAND GROUND MOTION SIMULATIONS FOR SCENARIO EARTHQUAKES IN THE SAN FRANCISCO BAY REGION

Robert Graves
URS Group Inc.
566 El Dorado Street, 2nd Floor
Pasadena, CA 91101

Tel: 626-449-7650
Fax: 626-449-3536
Email: Robert_graves@urscorp.com

Abstract

The 100th Anniversary Earthquake Conference (April 2006) commemorating the 1906 San Francisco earthquake documented the tremendous advances that have been made in seismology and earthquake engineering over the last century. The Conference also reiterated the continuing need to improve our level of preparedness, for it is inevitable that a major earthquake will strike the Bay Area again sometime in the future.

This eventuality has been assessed and quantified by the Working Group on California Earthquake Probabilities who recently determined that there is a 62% probability of a M_w 6.7 or greater earthquake occurring in the greater San Francisco Bay region during the 30 year period 2002-2031 (WG02, 2003). Of the main faults in this region, the Hayward-Rogers Creek system (27%) and the San Andreas fault (21%) have the highest individual probabilities.

Currently, the 1989 M_w 6.9 Loma Prieta earthquake provides the most detailed insight into the types of ground motion effects that may be expected in the San Francisco Bay region during rupture of these other faults. These effects include strong rupture directivity, trapping and amplification of basin waves, and amplification due to critical Moho reflections. However, rupture during the Loma Prieta earthquake was confined primarily to depths greater than about 5-10 km, so this event may have different ground motion characteristics than those expected for surface rupturing faults. In particular Somerville (2003) has shown that ground motions from surface rupturing earthquakes, on average, are about 30% lower than those observed for buried ruptures at periods between 0.3 to 3 seconds.

The objective of this project is to provide quantitative estimates of the ground motions expected from large earthquakes on major strike-slip faults of the San Francisco Bay region. Using broadband ground motion simulation procedures, we will quantify the ground motions that could be generated by different earthquake scenarios occurring on these faults, taking account of several important ground motion features. These include the effects of forward rupture directivity, the effects of basin trapped waves, and the characteristics of ground motions from shallow rupture.

We have extensive experience in the characterization and modeling of these effects in past earthquakes. This includes the analysis of rupture directivity effects from numerous earthquakes and the development of an empirical model of these effects (Somerville et al., 1997). We have performed detailed analyses of the strong motion records from shallow and buried rupturing events and have documented the differences in ground motions between these classes of earthquakes. We have also studied rupture characteristics of shallow and buried faults using both theoretical analyses and by examining published rupture models of past earthquakes. These studies suggest that the observed ground motion differences are related to lower slip velocities on shallow fault ruptures compared to those inferred for deeper fault ruptures.

Furthermore, we have recently developed an enhanced broadband time history simulation procedure that combines deterministic aspects at low frequencies ($f < 1$ Hz) with stochastic aspects at high frequencies ($f > 1$ Hz) (Graves and Pitarka, 2004 and 2010). The method uses a kinematic description of fault rupture, incorporating spatial heterogeneity in slip and rupture velocity by discretizing an extended finite-fault into a number of smaller subfaults. Differences in slip velocity between deep and shallow portions of the rupture are explicitly included in the parameterization. The stochastic approach sums the response for each subfault assuming a random phase, an omega-squared source spectrum and generic ray-path Green' functions (extension of Boore, 1983). We use the convolution operator of Frankel (1995) to ensure that the stochastic summation is not dependent on the choice of subfault dimensions. The deterministic approach sums the response for many point sources distributed across each subfault. Wave propagation at frequencies below 1 Hz is modeled using a 3D viscoelastic finite difference algorithm. This methodology has been successfully tested through the modeling of ground motion data from a number of recent earthquakes including the 1989 Loma Prieta earthquake, giving us confidence in the predictive capabilities of this approach in the San Francisco Bay region.

Our project will compliment ongoing USGS efforts to estimate the ground motions that might occur for scenario earthquakes in the San Francisco Bay region. The target of the proposed work is to use rigorous seismological modeling of broadband strong ground motions for additional earthquake scenarios on the Hayward-Rogers Creek and San Andreas faults in order to provide a more comprehensive framework for assessing earthquake hazards in the San Francisco Bay region. Direct products for earthquake loss reduction in northern California from this work include the development of scenario maps of ground motions from large earthquakes for use in emergency planning and loss estimation, and the development of broadband ground motion time histories and response spectra for use in the design and retrofit of structures.

Products for Earthquake Loss Reduction

The goal of our project is to use rigorous seismological modeling of broadband strong ground motions for scenario ruptures of the San Andreas fault in the San Francisco Bay region to help assess and quantify the expected ground shaking hazard for such events. Direct products for earthquake loss reduction in northern California from this work include:

- Scenario maps of ground motions from large earthquakes in the San Francisco Bay region for use in emergency planning and loss estimation.
- Broadband ground motion time histories and response spectra from large earthquakes in the San Francisco Bay region for use in the design and retrofit of structures.

All of the broadband time histories and maps generated in this project will be archived and made freely available to other researchers and investigators.

Publications

The work performed during this project has been described in a series of four papers that have been published/submitted to the Bulletin of the Seismological Society of America. The PI's contribution to the first two of these papers was also supported by USGS External Grant #06HQGR0132. These two papers have already been published:

Aagaard, B. T., T. M. Brocher, D. Dolenc, D. Dreger, R. W. Graves, S. Harmsen, S. Hartzell, S. Larsen, and M. L. Zoback (2008). Ground-motion modeling of the 1906 San Francisco earthquake, Part I: validation using the 1989 Loma Prieta earthquake, *Bull. Seism. Soc. Am.*, 98, 989-1011.

Aagaard, B. T., T. M. Brocher, D. Dolenc, D. Dreger, R. W. Graves, S. Harmsen, S. Hartzell, S. Larsen, Kathleen McCandless, Stefan Nilsson, N. Anders Petersson, Arthur Rodgers, Björn Sjögreen, and M. L. Zoback (2008). Ground-motion modeling of the 1906 San Francisco earthquake, Part II: Ground-Motion Estimates for the 1906 Earthquake and Scenario Events, *Bull. Seism. Soc. Am.*, 98, 1012-1046.

The second set of papers is focused on scenario ruptures of the Hayward fault system and these papers are in the final stages of review at BSSA and should be published in late 2010 or early 2011:

Aagaard, B. T., R. W. Graves, D. P. Schwartz, D. A. Ponce, and R. W. Graymer (2010). Ground-motion modeling of Hayward fault scenario earthquakes I: Construction of the suite of scenarios, submitted to *Bull. Seism. Soc. Am.*

Aagaard, B. T., R. W. Graves, A. Rodgers, T. M. Brocher, R. W. Simpson, D. Dreger, N. A. Petersson, S. C. Larsen, S. Ma, and R. C. Jachens (2010). Ground-motion modeling of Hayward fault scenario earthquakes II: Simulation of long-period and broadband ground motions, submitted to *Bull. Seism. Soc. Am.*

Preprints of the above two papers are appended to this final report. Once the papers are published, reprint copies will be submitted to the External Grants Office.

Ground-motion modeling of Hayward fault scenario earthquakes I: Construction of the suite of scenarios

by Brad T. Aagaard, Robert W. Graves, David P. Schwartz, David A. Ponce, and Russell W. Graymer

February 17, 2010

For submission to BSSA

Abstract We construct kinematic earthquake rupture models for a suite of 39 Mw 6.7–7.2 scenario earthquakes involving the Hayward, Calaveras, and Rodgers Creek faults. We use these rupture models in 3-D ground motion simulations as discussed in Part II (Aagaard *et al*., XXXX) to provide detailed estimates of the shaking for each scenario. We employ both geophysical constraints and empirical relations to provide realistic variation in the rupture dimensions, slip heterogeneity, hypocenters, rupture speeds, and rise times. The five rupture lengths include portions of the Hayward fault as well as combined rupture of the Hayward and Rodgers Creek faults and the Hayward and Calaveras faults. We vary rupture directivity using multiple hypocenters, typically three per rupture length, yielding north-to-south rupture, bilateral rupture, and south-to-north rupture. For each rupture length and hypocenter, we consider multiple random distributions of slip. We use two approaches to account for how aseismic creep might reduce coseismic slip. For one subset of scenarios, we follow the slip-predictable approach and reduce the nominal slip in creeping regions according to the creep rate and time since the most recent earthquake, whereas for another subset of scenarios we apply a vertical gradient in the nominal slip in creeping regions. The rupture models include local variations in rupture speed and use a ray-tracing algorithm to propagate the rupture front. Although we are not attempting to simulate the 1868 Hayward fault earthquake in detail, a few of the scenarios are designed to have source parameters that might be similar to this historical event.

Introduction

Forecasting the rupture behavior of faults is a primary consideration in estimating the seismic hazard and the ground motions they can generate. The Hayward and Rodgers Creek fault system is long and physically complex. It contains both creeping (Hayward) and primarily locked (Rodgers Creek) sections, a 4 km-wide right step between the Hayward and Rodgers Creek faults (Parsons *et al*., 2003), and a large historical earthquake in 1868 that ruptured only part of the Hayward fault. Models of how the Hayward fault has ruptured in the past and is likely to rupture in the future evolve through time as we learn more about its past ruptures and how strain accumulates along its length. Various Working Groups on California Earthquake Probabilities (WGCEP, 1988; WGCEP, 1990; WGCEP, 1999; WGCEP, 2003; WGCEP, 2008) developed segment rupture models for the fault. The first Working Group (WGCEP, 1988) divided the Hayward fault into two independent segments with a fixed boundary at San Leandro based largely on historical seismicity– the occurrence of the 1868 earthquake on the southern part of the fault and the presumption that a large earthquake in 1836 occurred on the northern part of the fault. Following the Loma Prieta earthquake the WGCEP (1990) added the Rodgers Creek fault, with a boundary in San Pablo Bay, as an additional independent segment.

New data and increased understanding of fault creep, recognition that the 1836 earthquake was not on the northern Hayward fault, paleoseismic dates of past earthquakes along the fault system, and a revised estimate of the length of the 1868 rupture using geodetic data, led the WGCEP (1999) to reevaluate Hayward-Rodgers Creek segmentation as part of its preliminary estimate of Bay Area-wide earthquake probabilities. The working group relaxed the fixed segment boundaries and allowed for uncertainty in the locations of rupture end points, but the most significant change was the incorporation of multiple segment ruptures. In addition to retaining three independent segments, southern Hayward, northern Hayward, and Rodgers Creek, the system was allowed to fail with a rupture of the full Hayward fault and a combined Hayward-Rodgers Creek rupture. The WGCEP (2003) completed the development of these models and estimated the mean 30-year probability (2002-2031) for a magnitude 6.7 or larger event on the Hayward-Rodgers Creek system at 27 percent. A California-wide probability study (WGCEP, 2008), which incorporated the WGCEP (2003) fault rupture models for the Hayward-Rodgers Creek faults and a modified overall methodology, increased the 30-year probability (2007-2036) to 31 percent. Based on earthquake-cycle simulations of repeating single segment ruptures with a viscoelastic model and a Coulomb failure criterion, Pollitz and Schwartz (2008) suggest that the probability may exceed 50 percent.

In this study we build upon the WGCEP (2003) model enhanced with new interpretations of fault geometry from 3-D geologic mapping, rupture parameters of the 1868 earthquake, and models of creep distribution on the fault plane. With the commemoration of the 140th anniversary of the 1868 earthquake in October, 2008 in mind, we consider a

suite of scenario earthquakes involving rupture of the Hayward fault. Our focus includes characterizing the ground motions from the earthquakes, and we build upon our experience simulating other earthquakes and scenario events in the San Francisco Bay area.

For the centennial of the 1906 earthquake, Aagaard *et al*. (2008b) estimated the ground motions for the 1906 earthquake and seven other scenario earthquakes rupturing the same northern section of the San Andreas fault. The modeling effort also included comparing two realizations of the 1989 Loma Prieta earthquake against the recorded long-period motions (Aagaard *et al*., 2008a). The two sets of simulations provide insight into the ground motions throughout the San Francisco Bay area for strike-slip ruptures along the San Andreas fault. The scenarios examined the sensitivity of the ground motions to the hypocenter and distribution of slip. Three scenarios used the same slip distribution as in the 1906 earthquake but a different hypocenter, and four scenarios used a random slip distribution with either the 1906 hypocenter or one of the three other hypocenters. The simulations highlighted amplification in several sedimentary basins, such as the Cupertino basin west of San Jose, the Cotati and Windsor basins under Santa Rosa, the Livermore basin, and the Great Valley, and also suggested a strong sensitivity to the hypocenter. Ruptures propagating north-to-south generated strong shaking across a larger fraction of the San Francisco Bay urban area than south-to-north ruptures.

In this study we expand the range of parameters and number of scenarios to include variation in the magnitude (through use of different rupture lengths), rupture speed, and rise time. We also consider two different approaches for accounting for creep in constructing the slip distributions. This selection of parameters that we vary across the suite of scenarios is based on both the sensitivity of ground motions to source characteristics established through kinematic source inversions and modeling parameter studies. For example, several studies that have shown the importance of including variation of the hypocenter when characterizing ground motions for a given site or area (Somerville *et al*., 1997; Aagaard *et al*., 2001; Olsen *et al*., 2006). Aagaard *et al*. (2001) also documented the sensitivity of near-source ground motions to subshear rupture speed and rise time in considering rupture of a generic vertical strike-slip fault and a shallow dipping reverse fault. Aagaard and Heaton (2004) illustrated the effects of sustained supershear rupture on the distribution of shaking.

Ideally, we would like to select values for each of these parameters using the appropriate probability density functions and use a Monte-Carlo approach to run thousands of simulations and produce probability functions for the ground motions. For many of the parameters, however, observations have yet to provide sufficient constraints on the probability density functions and how or whether they are correlated, so that only a mean value or a range of values is known. Additionally, due to time constraints we decided to limit the scope to a few dozen scenarios. Consequently, we selected a few reasonable choices for each parameter in developing a suite of 39 earthquake scenarios. In the following

sections we discuss the construction of the rupture models for this suite of scenarios. Part II (Aagaard *et al*., XXXX) discusses the results from three-dimensional ground-motion simulations of these scenarios.

Rupture Parameters

The 2003 WGCEP in the San Francisco Bay Area (WGCEP, 2003) provides the most extensive evaluation of rupture parameters for scenario earthquakes in the San Francisco Bay region. For ruptures involving the Hayward fault, they considered rupture of the southern portion of the fault, the northern portion of the fault, rupture of the entire fault, and combined rupture of the Hayward and Rodgers Creek faults (with participation of either the northern portion of the Hayward fault or the entire fault). We include four of these five rupture lengths (Figure 1 and Table 1) in our suite of scenarios with our rupture endpoints within the rupture segment boundaries developed by the working group. We did not include rupture of only the northern portion of the Hayward fault, because it has a much shorter rupture length and, as a result, a much smaller magnitude than the other cases.

Berkeley marks the southern endpoint of northern Hayward segment (Hayward North) and the northern endpoint of the southern Hayward segment (Hayward South). The discontinuity at Berkeley is located at a prominent seismicity cluster along the Hayward fault, the inferred northern extent of the 1868 rupture (Yu and Segall, 1996), and geologic complexity at seismogenic depths (Graymer *et al*., 2005; Graymer *et al*., 2007). Ponce *et al*. (XXXX) suggest this segment boundary is the most prominent discontinuity along the Hayward fault. Recent seismic, geologic, and geophysical evidence suggests that at depth the Hayward fault extends south to the Central Calaveras fault as a relatively smooth, continuous structure (Manaker *et al*., 2005; Graymer *et al*., 2007b). As a result, a rupture on the Hayward fault might continue south onto the Calaveras fault, or a rupture on the Calaveras fault might continue north onto the Hayward fault. Because this extends rupture south towards the densely populated San Jose area, we consider combined rupture of the southern portion of the Hayward fault and a 23 km section of the Calaveras fault. We allow rupture on the Calaveras fault from its junction with the Hayward fault south to the northern extent of the 1984 Morgan Hill earthquake. The southern extent of rupture in the Hayward South + Central Calaveras ruptures marks a change in Calaveras fault geometry near the northern end of zone III in Oppenheimer *et al*. (1990) and lies near the intersection of the Mount Lewis trend and the Calaveras fault (Watt *et al*., XXXX). Thus, the five rupture lengths considered in this study (shown in Figure 1) include (1) the southern portion of the Hayward fault (Hayward South), (2) the northern and southern portions of the Hayward fault (Hayward South + North), (3) a portion of the Calaveras fault and the southern portion of the Hayward fault (Central Calaveras + Hayward South), (4) the northern portion of the Hayward fault and the Rodgers Creek fault (Hayward North + Rodgers Creek), and (5) the southern and northern portions of the Hayward

fault and the Rodgers Creek fault (Hayward South + North + Rodgers Creek). The electronic supplement contains a table with the endpoints for each rupture segment.

We select the rupture width based on estimates of the base of the seismogenic zone as determined by microseismicity and heat flow data. These are the same constraints used by WGCEP (2003) and d'Alessio *et al.* (2005). For the Hayward, Rodgers Creek, and Calaveras faults the base of the seismogenic zone is relatively shallow, extending down to about 13 km depth for the Hayward fault and 10 km depth for the Rodgers Creek and Calaveras fault (WGCEP, 2003). We set the rupture width equal to the maximum depth of the seismogenic zone for the purposes of computing rupture areas. However, we impose a linear taper in the slip distribution at the lateral and bottom edges of the rupture. In order to maintain the same seismic potency as a uniform slip distribution extending to the maximum depth of the seismogenic zone, we place the center of the taper regions at the bottom of the seismogenic zone.

Fault Geometry

We construct a three-dimensional model of the Hayward fault system (including the Rodgers Creek and Calaveras faults) from (1) the active surface trace, (2) microseismicity, (3) potential field geophysical modeling, and (4) regional deformation. We use the active surface trace to control the top of the fault surface and generalize the surface traces from several faults maps (Lienkaemper, 1992; Graymer *et al.*, 1995; Graymer *et al.*, 1996; Graymer, 2000; Wentworth *et al.*, 1999; California Division of Mines and Geology, 2000) into a single surface trace. In regions with sufficiently dense microseismicity, the double-difference relocated hypocenters (Waldhauser and Ellsworth, 2002) define the fault surface (Simpson *et al.*, 2004; Graymer *et al.*, 2005; Phelps *et al.*, 2008). In several places we also utilize potential field geophysical modeling to define the fault in the subsurface. The gravity field constrains the releasing step between the Rodgers Creek and Hayward faults below San Pablo Bay (Parsons *et al.*, 2003). In the San Leandro area (between Oakland and Hayward), the presence of dense, magnetic gabbro in the Hayward fault zone allows the use of gravity and magnetic fields to model the broad fault zone (Ponce *et al.*, 2003). In this area microseismicity is sparse but appears to be concentrated along the west side of the steeply east dipping gabbro body, so we interpret the gabbro bounding surface to be the active fault at depth. Finally, in areas without dense microseismicity or geophysical anomalies, we project the fault surface to depth from its surface trace using a dip angle based on consideration of regional deformation. Outside of releasing stepovers, stress on the active fault is observed to have a slight compressional component, resulting in oblique reverse offset and uplift. The fault surface is interpreted as dipping steeply in the direction of the uplifted side.

At the surface the connection between the Hayward fault and the Calaveras fault is composed of a suite of oblique reverse right-lateral faults forming a complex restraining connection (Andrews *et al.*, 1993; Graymer *et al.*, 2007a).

At depths associated with large earthquakes (i.e., depths greater than about 5 km), however, the faults form a single continuous surface with only a slight bend (Simpson *et al*., 2004; Manaker *et al*., 2005; Graymer *et al*., 2007a). This direct connection led previous studies (Graymer *et al*., 2007a; Ponce *et al*., 2007) to suggest that through-going rupture on the southern portion of the Hayward fault and the central portion of the Calaveras fault could result in an earthquake as large as magnitude 7.2. On the other hand, there is no direct connection between the Rodgers Creek and the northern portion of the Hayward fault in the 3-D model. There is insufficient microseismicity in the San Pablo Bay region to define the active structure. However, there is a continuous rock body imaged in the magnetic field that extends from the Rodgers Creek fault to the northward extension of the Hayward fault beneath San Pablo Bay. This rock body marks the northward limit of a presumed suite of normal and oblique normal right-lateral faults that form a pull-apart basin in the right step (Jachens *et al*., 2002; Parsons *et al*., 2003).

Hypocenters

For the five rupture lengths we use a total of five hypocenters to provide variability in the direction of rupture propagation. In general, we place hypocenters at physical discontinuities that reflect changes in subsurface physical properties or changes in subsurface structure that might concentrate stress and thus, be more likely to generate earthquakes. We refine the hypocenters selected by the WGCEP (2003) by incorporating recent geologic and geophysical information. In the following paragraphs we summarize the rationale and criteria for the location of each hypocenter (Table 2); a more detailed description of possible discontinuities or segment boundaries along the Hayward fault, based on geologic, geophysical, and seismicity data, can be found in Ponce *et al*. (XXXX).

The San Pablo Bay hypocenter along with the southern endpoint of Rodgers Creek fault and the northern endpoint of Hayward North are located in the northern part of San Pablo Bay. The hypocenter is defined by the location of two aeromagnetic anomalies, one of which may be an offset counterpart of the San Leandro gabbro, based on its associated gravity anomaly (Jachens *et al*., 2002). At this location the sparse seismicity diverges from the strong linear trend of the recent trace of the Hayward fault (Jachens *et al*., 2002). Here, slip along the Hayward fault transfers to the Rodgers Creek fault across an approximately 4 km-wide right-stepover (Parsons *et al*., 2003), which is likely comprised of multiple normal and oblique normal right-lateral faults. Although geophysical evidence precludes a simple connection between the two faults, Parsons *et al*. (2003) cited evidence for a normal fault at this location. Our hypocenter corresponds to the approximate location of such a normal fault between the Hayward and Rodgers Creek faults. Rupture initiation at this location might be similar to the 1995 Kobe earthquake, which nucleated in a geometrically complex region at the intersection of the Nojima fault and the Suma and Suwayama fault (Zhao *et al*., 1996).

Scenarios for three rupture lengths nucleate at the San Pablo Bay hypocenter: a southward unilateral Hayward South + North rupture, a bilateral Hayward North + Rodgers Creek rupture, and a bilateral Hayward South + North + Rodgers Creek rupture. Slip in these rupture models begins on the Hayward and Rodgers Creek fault surfaces at the closest points to this hypocenter.

The Oakland hypocenter sits at the northern edge of the geophysically defined San Leandro gabbro (Ponce *et al*., 2003), a bend in the fault (Lienkaemper *et al*., 1991), and a shallow locked patch (Simpson *et al*., 2001; Schmidt *et al*., 2005). This boundary marks a dramatic change in physical properties along the fault that may extend throughout the seismogenic zone. Here, the San Leandro gabbro, which extends to a depth of at least 6–8 km, may concentrate stress and serve as a nucleation point for large earthquakes. Scenarios for three rupture lengths nucleate from the Oakland hypocenter: a southward unilateral Hayward South rupture, a southward unilateral Hayward South + Central Calaveras rupture, and a bilateral Hayward South + North rupture.

We locate the Hayward hypocenter in the central part of the Hayward fault where the fault surface bends at depths greater than about 5 km. This is near the junction of the Hayward fault with the Mission fault. Scenarios for two rupture lengths use this hypocenter: a bilateral Hayward South rupture and a bilateral Hayward South + Central Calaveras rupture.

The Fremont hypocenter lies near the southernmost extent of surface rupture of the 1868 earthquake and the southern extent of the mapped recently active surface trace of the Hayward fault (Lienkaemper *et al*., 1991). At seismogenic depths this hypocenter is approximately below the Mission seismicity trend, which represents seismicity on the Hayward fault at depths below about 5 km (Ponce *et al*., 2004; Simpson *et al*., 2004; Manaker *et al*., 2005). Scenarios for two rupture lengths nucleate at this hypocenter: a northward unilateral Hayward South rupture and a northward unilateral Hayward South + North rupture.

The Alum Rock hypocenter in our scenarios sits at the junction between the Hayward and Calaveras faults at depth (Graymer *et al*., 2007). This location correlates with a bend in the fault and lies about one kilometer north of the hypocenter of the 2007 Mw 5.4 Alum Rock earthquake. At this location seismicity at depths greater than 5 km connects to seismicity along the Central Calaveras fault (Ponce *et al*., 2004; Simpson *et al*., 2004; Manaker *et al*., 2005; Graymer *et al*., 2007a). The northward unilateral Hayward South + Central Calaveras rupture nucleates at this hypocenter.

Slip Distribution and Magnitude

We want to specify the slip distribution for our scenarios so that it conforms to the specified rupture lengths and widths and exhibits the heterogeneous character of slip found in kinematic source inversions. For the Hayward fault

we also must account for the effect of creep on the coseismic slip. The constraints on the rupture length and width and effect of creep on coseismic slip effectively constrain long length-scale features of the slip distribution. Shorter length scales are associated with the spatial variability of slip required to generate ground motions with spectral characteristics that match observations. This naturally leads to selecting a deterministic approach for setting the background (long length-scale) features of the slip distribution and a stochastic approach for setting the short length-scale features.

We include all deterministic contributions to the slip distribution in the background or nominal slip. The primary features include a uniform slip field with tapering along the lateral and bottom edges of the rupture and the effects of creep on the coseismic slip. We will discuss two different approaches that account for the effect of creep on the coseismic slip in the next section. The lateral edges use a linear taper over 5.0 km whereas the bottom edge uses a linear taper over 3.0 km. The widths of these tapers is somewhat arbitrary, and the primary purpose of the tapering is to prevent large asperities from the stochastic portion from occurring at the edges of the slip distributions. As mentioned earlier, we place the center of the taper at the rupture end points and base of the seismogenic zone. This yields the same seismic potency as the case of uniform slip. Allowing slip to extend slightly deeper than the maximum depth of microseismicity approximates the dynamics of large ruptures penetrating a few kilometers into regions of stable sliding.

For the short length-scale stochastic portion of the slip distribution, we use the characterization of kinematic source inversions by Mai and Beroza (2002). We create a zero-mean, random-phase normal distribution with a standard deviation equal to twice the nominal background slip. The power spectra for the magnitude in the wavenumber domain follows a von Karman distribution,

$$P(k) = \frac{a_s a_d}{(1+k^2)^{H+1}}, \tag{1}$$

$$k^2 = a_s^2 k_s^2 + a_d^2 k_d^2, \tag{2}$$

where H is the Hurst exponent, k_s and k_d are the along-strike and down-dip wavenumbers, and a_s and a_d are the along-strike and down-dip correlation lengths. We use the median value of 0.75 from Mai and Beroza (2002) for the Hurst exponent and their simple scaling of correlation lengths with magnitude,

$$\log a_s = -2.5 + \frac{1}{2} M_w, \text{ and} \tag{3}$$

$$\log a_d = -1.5 + \frac{1}{3} M_w. \tag{4}$$

We also incorporate random variations into the rake angle using a normal distribution with a standard deviation of 10 degrees. The magnitude of the slip includes spatial coherence via the von Karman distribution, but the variation in the rake angle does not. We do not believe this significantly affects the resulting ground motions because the variations in rake angle are relatively small.

An important parameter in the overall slip distribution is the length-scale that defines the cross-over between the background distribution and the stochastic distribution. Selecting too short of a length-scale for the cross-over results in only very short length-scale heterogeneity. This leads to excessive energy radiated at long periods and a deficiency of energy radiated at shorter periods. On the other extreme, selecting too long of a length-scale for the cross-over results in ruptures that do not have the desired dimensions due to large regions with zero slip. To choose a reasonable cross-over length scale, we generated broadband ($T > 0.1$ s) synthetics for a simple one-dimensional velocity structure and a suite of 50 sites ranging from 2 km to 70 km from the rupture, with the goal of minimizing the overall residual in spectral acceleration with respect to Next Generation Attenuation (NGA) ground-motion prediction models.

These simulations use the hybrid broadband ground-motion simulation methodology of Graves and Pitarka (2004) with a 1-D seismic velocity model based on the generic rock profile of Boore and Joyner (1997), deterministic ground-motion calculations at periods longer than 1.0 seconds, and stochastic ground-motion calculations for periods 0.10–1.0 seconds. We modify the generic rock profile to have an average shear-wave speed in the top 30 meters (Vs30) of 865 m/s, which minimizes the potential impact of non-linear amplification effects. We compute the peak horizontal acceleration and velocity and spectral acceleration at periods of 0.3, 1.0, and 3.0 s and compare against the NGA models from Abrahamson and Silva (2008), Boore and Aktinson (2008), Campbell and Bozorgnia (2008), and Chiou and Youngs (2008). For consistency with subsequent comparisons of our 3-D ground motion simulations (Aagaard *et al*., XXXX), we have not included the relation of Idriss (2008) in this calibration; it is not applicable to the soft-soil sites found throughout the Bay area because it limited to sites with Vs30 values greater than 450 m/s. In this calibration exercise, we use the Mw 6.76 Hayward South rupture dimensions.

Figure 2 shows the residuals for three different cross-over length scales: 25%, 33%, and 50% of the rupture length. All three exhibit similar trends at the shorter periods, but have noticeably different behavior at longer periods. The cross-over at 25% of the rupture length produces quite large long-period motions compared to the ground-motion prediction equations. This short length-scale cross-over corresponds to a slip distribution with small, short length-scale variations about the nominal slip value. This causes the rupture to be relatively smooth and coherent across the fault surface, which increases the radiation at longer periods. Employing a longer length-scale for the cross-over mitigates this effect. Using a cross-over of 50% of the rupture length provides the smallest residuals at periods of 1 and 2 seconds due to the increased spatial heterogeneity in the rupture as it propagates around the low slip regions. As a result of this calibration, we selected to cross-over from the background slip distribution to the stochastic slip distribution at a length scale equal to one-half of the rupture length.

Accounting for Creep

The Hayward fault differentiates itself from many faults by accommodating part of its long-term slip via aseismic creep. Development along the fault over the last century has created numerous man-made features that have been deformed or offset by creep at the surface. These include Memorial Stadium on the campus of the University of California at Berkeley, the Berkeley Hills Tunnel which carries BART subway trains, and the old city hall in Hayward, as well as numerous curbs, walls, and fences (Stoffer, 2008). Several studies have suggested demarcation of creeping and locked regions of the fault based on various combinations of microseismicity, alinement arrays, GPS surveys, and InSAR (Burgmann *et al*., 2000; Simpson *et al*., 2001; Wyss, 2001; Waldhauser and Ellsworth, 2002; Schmidt *et al*., 2005; Funning *et al*., 2007). The details vary among the models with those controlled primarily by seismicity (Wyss, 2001; Waldhauser and Ellsworth, 2002) having smaller locked patches than those controlled primarily by geodetic measurements (Burgmann *et al*., 2000; Simpson *et al*., 2001; Funning *et al*., 2007). All five of the models support a locked region underneath Oakland. The Funning *et al*. (2007) geodetic model provides the most recent demarcation of the locked and creeping regions and estimates the rate of slip within the creeping regions, making it possible to account for the existence and rate of creep in constructing our rupture models.

To what extent the creeping regions participate in earthquake ruptures of the Hayward fault remains an open question. Documentation of the mole-track from the 1868 Hayward fault earthquake (Lawson, 1908) fails to indicate whether it was the result of coseismic slip or postseismic deformation. The WGCEP (2003) assumed that the rupture area for a given magnitude earthquake on the Hayward fault might be about 25 percent larger than the same sized event on a completely locked fault, as a result of slip on the creeping areas contributing to the coseismic slip. Behavior on other faults with creeping patches provides little guidance. Both postseismic creep and coseismic surface rupture on the main trace of the San Andreas fault were documented in the 1966 Mw 6.0 Parkfield earthquake, whereas the 2004 Mw 6.0 Parkfield earthquake produced postseismic creep with very little coseismic surface rupture on the main trace of the San Andreas fault (Lienkaemper *et al*., 2006). Postseismic surface creep also appears to have been comparable to the coseismic surface slip in the 1987 Mw 6.6 Superstition Hills earthquake (Sharp *et al*., 1989). We consider two different approaches that account for how creep may affect coseismic rupture, which we incorporate into the nominal (long length scale) portion of the slip distribution. Recall that we also include a stochastic contribution that permits significant deviations from the nominal or background slip at short length scales.

The slip-predictable approach provides a simple model for forecasting the nominal slip in the next earthquake based on the long-term slip rate and elapsed time from the most recent event (Shimazaki and Nakata, 1980). Although it is not a reliable method, as shown by Murray and Segall (2002) and Murray and Langbein (2006) for the Parkfield, California region, it does allow direct inclusion of spatial variations in the creep rate, such that the nominal coseismic slip is much smaller in regions creeping closer to the long-term fault slip rate. Using the slip-predictable approach,

in the locked patches the nominal slip is equal to the product of the long-term slip rate and the elapsed time since the most recent event; in the creeping patches the nominal slip is equal to the product of the difference between the long-term slip rate and the creep rate and the elapsed time since the most recent event. As a result, spatial variations in creep rate generate spatial variations in nominal slip. If the creep rate equals the long-term slip rate, then the nominal slip is zero.

For the Hayward fault we use the 1868 earthquake as the most recent large event, a long-term slip rate of 9 mm/yr (WGCEP, 2003; WGCEP, 2008), and the creep rates from Funning *et al.* (2007) to construct the background slip distribution using the slip-predictable approach. Figure 3 shows the background slip distribution for the Hayward South + North rupture length generated with this approach. The electronic supplement contains plots for this approach applied to all of the rupture lengths. Because we do not know the timing of the most recent large event on the 23 km portion of the Calaveras fault that ruptures in our Hayward South + Central Calaveras scenarios, we also use 1868 as the time of the most recent rupture for that portion of the Calaveras fault. For the Rodgers Creek fault we use 230 years as the elapsed time since the most recent large earthquake; Hecker *et al.* (2005) propose that the elapsed time is probably between 232 and 292 years.

Recognizing the limitations of the slip-predictable approach for accounting for aseismic creep, we also develop a simple alternative approach. Because aseismic creep reduces the accumulated strain in the crust, we assume that creeping regions tend to inhibit rupture propagation and progressively reduce the coseismic slip as the rupture propagates further into a creeping region. Furthermore, we assume that ruptures generating greater slip will be able to propagate further into creeping regions. We incorporate these features into our nominal slip distribution via a constant, vertical gradient in the nominal slip in patches that approximate the creeping regions delineated by Funning *et al.* (2007). The outline of the creeping patches is evident in Figure 4 as the areas with a vertical gradient in slip along the shallow portion of the rupture. In contrast to the slip-predictable approach where the time since the most recent event and fault slip-rate determine the nominal slip, in this approach we set the average slip so that the moment magnitude matches the value predicted by the Hanks and Bakun (2008) magnitude-area relation. We compute the reduced area factor, R, developed by the (WGCEP, 2003) so that the magnitude-area relation uses an effective area. The effective area corresponds to the area with uniform slip and the same seismic potency as our ruptures that have regions of uniform slip and regions with reduced slip due to the vertical gradient associated with aseismic creep. For the range of magnitudes in our scenarios (6.8–7.2) other magnitude-area relations (Wells and Coppersmith, 1994; Somerville *et al.*, 1999) yield very similar slip values.

A vertical gradient of zero in the slip distribution corresponds to creep having no affect on the coseismic slip distribution, whereas an infinite gradient corresponds to creep completely eliminating coseismic slip in creeping areas. In terms of the reduced area factor, R, as the gradient increases the reduced area factor decreases, resulting in smaller

magnitude events with less nominal slip. This leads to a decrease in the recurrence interval. For a gradient of -0.15 m/km, the reduced area factor is about 0.7–0.8, which is close to the value of 0.6 for the Hayward fault used by the WGCEP (2003). However, this slip gradient implies that the recurrence interval for events that rupture nearly the entire Hayward fault (Hayward South + North) is about 150 years. With an average recurrence interval of 170 years for the most recent 11 large events on the Hayward fault, such a model would be consistent with these 11 large events rupturing nearly the entire Hayward fault. Paleoseismic study of trenches across the fault in El Cerrito (10 km south of Point Pinole) along the northern portion of the Hayward fault do not support this behavior (Lienkaemper *et al.*, 1999). A gradient of -0.12 m/km is consistent with earthquakes that do not rupture the entire fault and have recurrence intervals ranging from 140–170 years. The reduced area factors, on the other hand, are on the high side and fall between 0.8 and 0.9 for the Hayward fault. Our preferred vertical slip gradient is -0.12 m/km, which provides nearly the same recurrence intervals as a gradient of -0.12 m/km with slightly smaller reduced area factors. Figure 4 shows the nominal slip distribution for the Hayward South + North rupture models. The electronic supplement contains plots for this approach applied to all of the rupture lengths.

This approach does not account for variations in creep rate, only the size of the creeping regions. Given the limited ability to resolve the spatial variation of creep at depth from geodetic measurements, we do not think this is a significant shortcoming. Another simple alternative approach to the slip-predictable method involves reducing the nominal slip via a scaling factor in creeping regions. In contrast to our slip-gradient approach, in the slip-scaling approach ruptures propagate the same distance into creeping areas independent of the amount of slip that they generate. As a result, we favor the slip-gradient approach in which ruptures generating larger slip tend to propagate further into creeping areas than ruptures generating less slip.

We also consider two scenarios on each of the Hayward South and Hayward South + North rupture lengths for the end-member cases of how creep may affect the coseismic slip. Two scenarios ignore the potential influence of creep (slip distribution N01 and N04), whereas in the two other scenarios we do not allow any coseismic slip in creeping regions (slip distributions F01 and F04). Altering the vertical slip gradient while maintaining consistency with the Hanks and Bakun (2008) magnitude-area relation results in variation of the moment magnitude of the ruptures. These scenarios in combination with the slip-predictable and vertical slip-gradient scenarios permit quantifying the effects of creep on the coseismic slip distribution and ground motions.

The simulation of high frequency motions using the semi-stochastic approach of Graves and Pitarka (2004) also must account for the effect of creep. In the semi-stochastic simulation, the total moment release of the earthquake scales with the high frequency stress parameter, σ_p (Boore, 1983). Following self-similarity, the moment also scales as $A^{3/2}$, or similarly as $R^{3/2}$, where R is the reduced area factor developed by WGCEP (2003). Thus, in order to properly account for the creeping portions of these ruptures, the stress parameter must also be scaled by $R^{3/2}$. Our

default value for the stress parameter is 50 bars. For the Hayward South rupture, R = 0.79, which yields a stress parameter for this rupture of 35 bars.

Slip-Time Function

In our modeling of the 1906 and 1989 Loma Prieta earthquakes (Aagaard *et al*., 2008b), we used the Brune pulse (Brune, 1970) for the slip-time function. This slip-time function exponentially approaches the value of final slip. Several recent studies (Spudich and Guatteri, 2004; Graves and Pitarka, 2004; Tinti *et al*., 2005; Liu *et al*., 2006) favor a slightly faster onset of slip, a period of slower slip, and then termination of slip. In this study we use the cosine-sine time function developed by Liu *et al*. (2006) because it provides these features with a simple analytical form for both the slip and slip rate as a function of time. Calibration using broadband ground motion simulations with a 1-D seismic velocity model (analogous to those described in the previous section for calibration of the cross-over length scale between the nominal background slip and the stochastic slip) confirm that the sine-cosine slip-time function reduces residuals in the spectral acceleration at 1.0 s compared with the Brune slip-time function. For the cosine-sine slip-time function slip at a point follows

$$D(t) = \begin{cases} D_f C_n \left(0.7t - 0.7\frac{\tau_1}{\pi}\sin\frac{\pi t}{\tau_1} - 1.2\frac{\tau_1}{\pi}\left(\cos\frac{\pi t}{2\tau_1} - 1\right)\right) & 0 \le t < \tau_1 \\ D_f C_n \left(1.0t - 0.7\frac{\tau_1}{\pi}\sin\frac{\pi t}{\tau_1} + 0.3\frac{\tau_2}{\pi}\sin\frac{\pi(t-\tau_1)}{\tau_2} + \frac{1.2}{\pi}\tau_1 - 0.3\tau_1\right) & \tau_1 \le t < 2\tau_1 \\ D_f C_n \left(0.3t + 0.3\frac{\tau_2}{\pi}\sin\frac{\pi(t-\tau_1)}{\tau_2} + \frac{1.2}{\pi}\tau_1 + 1.1\tau_1\right) & 2\tau_1 \le t < \tau \end{cases} \tag{5}$$

$$\dot{D}(t) = \begin{cases} D_f C_n \left(0.7 - 0.7\cos\frac{\pi t}{\tau_1} + 0.6\sin\frac{\pi t}{2\tau_1}\right) & 0 \le t < \tau_1 \\ D_f C_n \left(1.0 - 0.7\cos\frac{\pi t}{\tau_1} + 0.3\cos\frac{\pi(t-\tau_1)}{\tau_2}\right) & \tau_1 \le t < 2\tau_1 \\ D_f C_n \left(0.3 + 0.3\cos\frac{\pi(t-\tau_1)}{\tau_2}\right) & 2\tau_1 \le t < \tau \end{cases} \tag{6}$$

$$C_n = \frac{\pi}{1.4\pi\tau_1 + 1.2\tau_1 + 0.3\pi\tau_2} \tag{7}$$

$$\tau = 1.525 t_{95} \tag{8}$$

$$\tau_1 = 0.13\tau \tag{9}$$

$$\tau_2 = \tau - \tau_1 \tag{10}$$

where $D(t)$ is the slip at time t, D_f is the final slip, t_{95} is the rise time (as measured by the time it takes for 95% of the slip to occur), and τ, τ_1, τ_2, and C_n are constants.

As we did in our 1906 and 1989 Loma Prieta earthquake simulations, we vary the rise time with the square root of the local slip so that we achieve the desired scaling of the average rise time with magnitude proposed by Somerville *et al*. (1999) through a completely local prescription, i.e., one that does not involve quantities associated with the

entire rupture, such as seismic moment. The rise time follows

$$\frac{t_{95}}{t_0} = C\sqrt{\frac{D_f}{D_0}}, \tag{11}$$

where t_0 = 1.0 s, D_0 = 1.0 m, and we vary C across the scenarios to investigate the sensitivity of the ground motions to the rise time. We select values of 1.0, 1.5, or 2.0. We also consider nominally uniform rise times of 1.0 s (for a Hayward South rupture) and 2.0 s (for a Hayward South + North rupture). Figure 5 shows the Liu *et al.* (2006) sine-cosine slip time function for a final slip of 2.0 m and C = 1.5. At the top and bottom of the rupture, we linearly increase the rise time (scale C) by a factor of two over a distance of 3.0 km. Lengthening the rise time at the top and bottom of the rupture also follows from our modeling of the 1906 earthquake, and is driven by empirical observations of longer rise times for large surface ruptures (Kagawa *et al.*, 2004) and longer rise times associated with stable sliding regions at the top and bottom of the seismogenic zone. The scenarios with a nominally uniform rise time also include this lengthening of rise times at the top and bottom of the seismogenic zone. For the scenarios that examine the sensitive of the other source parameters, we use C = 1.5, which provides intermediate values.

Rupture Speed

The specification of local rupture speed in our kinematic rupture models is guided by our desire to include fluctuations in the rupture propagation path and match seismic observations of average rupture speed. Several studies using spontaneous rupture models suggest that the ruptures do not expand with circular wave fronts from the hypocenter but have complex propagation paths as a result of local variations in the fault constitutive parameters and stress field (Olsen *et al.*, 1997; Peyrat *et al.*, 2001; Dunham *et al.*, 2003). We introduce complexity in the rupture propagation path by correlating the rupture speed with slip and employ ray tracing to propagate the rupture front over the fault surface. This allows local variations in rupture speed to alter the direction of rupture propagation; for example, ruptures propagate around regions with very slow rupture speeds. Because we also want to match average rupture speeds from seismic observations, we adjust the parameters controlling the correlation of rupture speed with slip to match seismic observations of the average rupture speed.

From seismic observations of rupture propagation we typically identify radiation of energy from a location on the fault surface at a specific time. Using multiple observations we estimate the average rupture speed between locations on the fault surface. Because we do not know the path of rupture propagation, we usually assume the rupture propagates along the shortest path between the locations. When the rupture propagation path deviates from the shortest path, the estimate of the average rupture speed differs from the local rupture speed and the actual average rupture speed along the path; hence, the seismic observations provide only an *estimate* of the average rupture speed. By measuring the

average rupture speed in our kinematic rupture models in a manner consistent with seismic observations, we calibrate the correlation of rupture speed with slip to yield the desired estimates of average rupture speed.

We obtain average rupture speed estimates for the kinematic rupture models by measuring the average rupture speed over the shortest path between 1000 pairs of points. The points are randomly selected from locations where the slip exceeds the average slip; these should be the locations that radiate most of the energy. In selecting pairs of points we impose the restriction that both points sit on the same side of the fault surface from the hypocenter. We assess what rupture speeds would be measured in typical seismic observations of the rupture via the peak in the histogram of rupture speed and the range of rupture speeds over distances approaching the rupture length. We found that setting the local rupture speed to the limiting mode-II rupture speed (Rayleigh wave speed or about 92% of the shear-wave speed) generally gives average rupture speeds in the range of 80–90% of the local shear wave speed. In terms of the correlation of local rupture speed with slip, this case corresponds to

$$\frac{v_r}{v_s} = \begin{cases} 0.1 + 0.82\frac{D_f}{D_{avg}} \text{ if } D_f < D_{avg} \\ 0.92 \text{ if } D_f \geq D_{avg}, \end{cases} \tag{12}$$

where v_r is the local rupture speed, v_s is the shear-wave speed, D_f is the final slip, and D_{avg} is the average slip. We also consider another case of subshear rupture with a slightly slower rupture speed,

$$\frac{v_r}{v_s} = \begin{cases} 0.1 + 0.72\frac{D_f}{D_{avg}} \text{ if } D_f < D_{avg} \\ 0.82 \text{ if } D_f \geq D_{avg}, \end{cases} \tag{13}$$

and a case in which the local rupture speed exceeds the shear wave speed in regions with large slip,

$$\frac{v_r}{v_s} = \begin{cases} 0.1 + 0.82\frac{D_f}{D_{avg}} \text{ if } D_f < D_{avg} \\ 0.92 + \frac{D_f - D_{avg}}{D_{max} - D_{avg}}(\sqrt{2} - 0.92) \text{ if } D_f \geq D_{avg}. \end{cases} \tag{14}$$

Figures 6 and 7 show the analysis of the rupture speed for Hayward South and Hayward South + North in which the local rupture speed follows equation (12). The electronic supplement contains the corresponding plots for all of the rupture models.

1868 Earthquake

We are not attempting to estimate the shaking in the 1868 earthquake, because very little is known about the slip distribution and hypocenter. Instead, we include a few scenarios that have rupture characteristics thought to be similar to the 1868 earthquake. The rupture length is reasonably well constrained to the southern two-thirds of the Hayward fault from observations of an approximately 32 km-long mole-track (Lawson, 1908), a geodetic analysis using triangulation surveys (Yu and Segall, 1996), trenching across the fault (Lienkaemper *et al.*, 1999; Liekaemper

and Williams, 1999; Liekaemper and Williams, 2007), and an analysis of the intensities using ShakeMap (Boatwright and Bundock, 2008). Furthermore, Boatwright and Bundock (2008) remarked that the north-south symmetry in the shaking intensities suggest that the rupture was bilateral. Thus, our scenarios with different slip distributions for a Hayward South rupture length and a Hayward epicenter roughly match the rupture parameters for the 1868 earthquake.

Rupture Models

From the selection of values for the five earthquake source parameters that vary across the suite of scenarios (rupture length, slip distribution, hypocenter, rupture speed, and rise time), we construct the suite of 39 rupture models given in Table 3. Figures 8 and 9 show the slip distribution and slip initiation time for two rupture models; the electronic supplement contains plots for all of the rupture models. These scenarios provide a range of hypothetical earthquakes that conform to geophysical constraints and empirical relations for rupture dimensions, slip heterogeneity, hypocenters, rupture speeds, and rise times. Additionally, the scenarios include two alternatives for how aseismic creep affects the coseismic slip distribution. Through systematic variation of the source parameters across the 39 scenarios, the effects of varying each parameter can be isolated. In many cases we have multiple scenarios for a given parameter value, permitting evaluation of the sensitivity of ground motions to joint variation of the parameters.

Example Ground Motions

Part II (Aagaard *et al*., XXXX) provides a detailed description and analysis of the ground motions simulations for all 39 scenarios, so we limit the discussion here to a brief overview of the ground motions in two of the scenarios. Both scenarios use the simple vertical slip-gradient approach to account for creep and involve bilateral rupture of the Hayward fault. Scenario HS G01 HypoH involves a Mw 6.76 event on the Hayward South rupture segment with an epicenter in Hayward, and scenario HS G04 HypoO involves a Mw 7.05 event on the Hayward South + North rupture segments with an epicenter in Oakland.

Figure 10 shows the Modified Mercalli Intensities (MMI) for Graves's broadband ($T > 0.1$ s) simulations of the two events. MMI is computed from peak horizontal velocities (PGV) and peak horizontal accelerations (PGA) following the relation developed by Wald *et al*. (2005) for use in ShakeMap. The shaking patterns reaffirm many well-known features as they apply to the San Francisco Bay area and rupture of the Hayward fault, such as (1) larger amplitude motions for larger events (the area subjected to shaking stronger than MMI VII increases from about 10% of the San Francisco Bay urban area for the Mw 6.76 scenario to more than 40% of the urban area for the Mw 7.05 scenario), (2) stronger shaking along the strike of the fault away from the epicenter as a result of rupture directivity, (3) amplification of motions in the several sedimentary basins scattered about the San Francisco Bay area (e.g., Livermore

basin, Evergreen basin east of San Jose, and the sedimentary basin underneath San Pablo Bay), and (4) sensitivity to the distribution of slip at sites close to the rupture (e.g., the high intensities surrounding the southern end of the rupture in scenario HS G01 HypoH).

The simulations also highlight some less common features that are important for understanding the seismic hazard in the San Francisco Bay area. For example, although the perimeter of the San Francisco Bay contains very soft soils, the sediment cover is relatively thin compared to the east side of the norther portion of the Hayward fault. This region is marked by deep, soft sediments, which causes the shaking intensities to be significantly higher east of the Hayward fault compared to west of the fault.

The velocity waveforms shown in Figure 11 further illustrate these trends. At site SF386 in Oakland a strong fault-normal velocity pulse dominates the ground-motion time history. For the Mw 6.76 Hayward South rupture the peak velocity is less than 0.5 m/s, but for the Mw 7.05 Hayward South + North rupture the peak velocity exceeds 1.0 m/s. The ground-motion time histories at site SF292 in Livermore and CT06085501400 in San Jose both exhibit long duration, large amplitude motions associated with surface waves in sedimentary basins. Site SF292 lies east of the rupture near the middle of the Livermore basin and site CT06085501400 lies south of the rupture near the edge of the Evergreen basin. At both sites the peak velocities exceed 0.6 m/s for the Hayward South + North rupture. For the Hayward South rupture, site CT06085501400 in San Jose experiences only slightly smaller peak velocities while site SF292 in Livermore experiences significantly smaller peak velocities compared to the Hayward South + North rupture. At each site the shapes of the waveform envelopes for the scenarios are quite similar, consistent with motions dominated by wave propagation rather than source effects. Thus, these three sites provide some examples of the many important features and trends observed in the ground motions from our suite of 39 scenarios.

Discussion and Conclusions

We construct 39 earthquake scenarios for the Hayward-Rodgers Creek fault system. The suite of scenarios capture variability in the source parameters consistent with geophysical and seismic observations as well as uncertainty in how creep may affect the distribution of coseismic slip on the Hayward fault. We use this suite of scenarios to identify important features in the ground motions, such as effects from the 3-D geologic structure and rupture directivity, and characterize the distribution of shaking and its sensitivity to variations in the earthquake source. The ground motions for the two scenarios discussed here (the ground motions from all of the scenarios are discussed in detail in Part II) demonstrate the strong sensitivity to the magnitude, distribution of slip, and amplification in soft sediments.

This study marks continued progress towards realizing the goal of constructing probabilistic seismic hazard maps that incorporate complex 3-D effects associated with geologic structure and rupture directivity. However, achieving

this goal will require appropriate sampling of the parameter space with probability density functions for all of the earthquake source parameters. Due to the large number of parameters, this necessary involves suites of scenarios with orders of magnitude more events than our suite of 39 earthquakes. More importantly, it requires moving beyond identifying correlations among seismic source parameters (Song *et al*., 2009; Schmedes *et al*.,) to quantify the variability of earthquake source parameters and develop the appropriate joint probability density functions. Only after we quantifying the variability in the seismic source parameters can we construct suites of scenarios that will accurately predict both the median and variance of ground motion while including the details of the seismic source and 3-D structure.

Data and Resources

The Funning *et al*. (2007) creep model was obtained directly from the authors. Janet Watt (U.S. Geological Survey) provided the updated Hayward fault geometry. All other fault geometry and a previous version of the Hayward fault geometry are available from the U.S. Geological Survey via http://earthquake.usgs.gov/regional/nca/3Dgeologic/ (last accessed February, 2010). All other data used in this paper came from published sources listed in the references. Many of the figures were generated using Generic Mapping tools (Wessel and Smith, 1998).

Acknowledgments

In developing the suite of scenario earthquakes, we benefited from discussions with Robert Simpson, James Lienkaemper, Paul Spudich, Jeanne Hardebeck, and Janet Watt. We thank Fred Pollitz and Thomas Hanks for careful reviews of the manuscript. Aagaard, Schwartz, Ponce, and Graymer were funded by the Earthquake Hazard Program of the U.S. Geological Survey. Graves was supported with funding from the Southern California Earthquake Center (SCEC). SCEC is funded by NSF Cooperative Agreement EAR-0529922 and USGS Cooperative Agreement 07HQAG0008. This is SCEC contribution number 1309.

References

Aagaard, B. T., T. M. Brocher, D. Dolenc, D. Dreger, R. W. Graves, S. Harmsen, S. Hartzell, S. Larsen, K. McCandless, S. Nilsson, N. A. Petersson, A. Rodgers, B. Sjögreen, and M. L. Zoback (2008b, April). Ground motion modeling of the 1906 San Francisco earthquake II: Ground motion estimates for the 1906 earthquake and scenario events. *Bulletin of the Seismological Society of America 98*(2), 1012–1046, doi: 10.1785/0120060410.

Aagaard, B. T., T. M. Brocher, D. Dolenc, D. Dreger, R. W. Graves, S. Harmsen, S. Hartzell, S. Larsen, and M. L. Zoback (2008a, April). Ground motion modeling of the 1906 San Francisco earthquake I: Validation using the 1989 Loma Prieta earthquake. *Bulletin of the Seismological Society of America 98*(2), 989–1011, doi: 10.1785/0120060409.

Aagaard, B. T., R. W. Graves, S. Ma, S. C. Larsen, A. Rodgers, N. A. Petersson, R. C. Jachens, T. M. Brocher, R. W. Simpson, and D. Dreger (XXXX). Ground motion modeling of Hayward fault scenario earthquakes II: Simulation of long-period and broadband ground motions. in preparation.

Aagaard, B. T., J. F. Hall, and T. H. Heaton (2001, May). Characterization of near-source ground motions with earthquake simulations. *Earthquake Spectra 17*(2), 177–207.

Aagaard, B. T. and T. H. Heaton (2004, December). Near-source ground motions from simulations of sustained intersonic and supersonic fault rupture. *Bulletin of the Seismological Society of America 94*(6), 2064–2078.

Abrahamson, N. and W. Silva (2008, February). Summary of the Abrahamson & Silva NGA ground-motion relations. *Earthquake Spectra 24*(1), 67–97, doi: 10.1193/1.2924360.

Andrews, D. J., D. H. Oppenheimer, and J. J. Lienkaemper (1993). The Mission link between the Hayward and Calaveras faults. *Journal of Geophysical Research - Solid Earth 98*(B7), 12083–12095.

Boatwright, J. and H. Bundock (2008). Modified Mercalli Intensity maps for the 1868 Hayward earthquake plotted in ShakeMap format. Open-File Report 2008-1121, U.S. Geological Survey. http://pubs.usgs.gov/of/2008/1121/ (last accessed 2/18/2009).

Boore, D. M. (1983, December). Stochastic simulation of high-frequency ground motions based on seismological models of the radiated spectra. *Bulletin of the Seismological Society of America 73*(6A), 1865–1894.

Boore, D. M. and G. M. Aktinson (2008, February). Ground-motion prediction equations for the average horizontal component of PGA, PGV, and 5%-damped PSA at spectral periods between 0.01 s and 10.0 s. *Earthquake Spectra 24*(1), 99–138, doi: 10.1193/1.2830434.

Boore, D. M. and W. B. Joyner (1997, April). Site amplifications for generic rock sites. *Bulletin of the Seismological Society of America 87*(2), 327–341.

Brune, J. N. (1970, September 10). Tectonic stress and spectra of seismic shear waves from earthquakes. *Journal of Geophysical Research 75*, 4997–5009.

Burgmann, R., D. Schmidt, R. M. Nadeau, M. d'Alessio, E. Fielding, D. Manaker, T. V. McEvilly, and M. H. Murray (2000, August 18). Earthquake potential along the northern Hayward fault, California. *Science 289*(5482), doi: 10.1126/science.289.5482.1178.

California Division of Mines and Geology (2000). *Digital images of Official Maps of Alquist-Priolo Earthquake Fault Zones of California, central coast region*. California Division of Mines and Geology. scale 1:24,000.

Campbell, K. W. and Y. Bozorgnia (2008, February). NGA ground motion model for the geometric mean horizontal component of PGA, PGV, PGD and 5% damped linear elastic response spectra for periods ranging from 0.01 to 10 s. *Earthquake Spectra 24*(1), 139–171, doi: 10.1193/1.2857546.

Chiou, B. S. and R. R. Youngs (2008, February). An NGA model for the average horizontal component of peak ground motion and response spectra. *Earthquake Spectra 24*(1), 173–215, doi: 10.1193/1.2894832.

d'Alessio, M. A., I. A. Johanson, R. Burgmann, D. A. Schmidt, and M. H. Murray (2005). Slicing up the San Francisco Bay Area: Block kinematics and fault slip rates from GPS-derived surface velocities. *Journal of Geophysical Research - Solid Earth 110*(B06403), doi: 10.1029/2004JB003496.

Dunham, E. M., P. Favreau, and J. M. Carlson (2003, March 7). A supershear transition mechanism for cracks. *Science 299*(5612), 1557–1559.

Funning, G. J., R. Burgmann, A. Ferretti, and F. Novali (2007). Asperities on the Hayward fault resolved by PS-InSAR, GPS and boundary element modeling. *EOS Trans. 88*(52). S23C-04.

Graves, R. W. and A. Pitarka (2004). Broadband time history simulation using a hybrid approach. In *13th World Conference on Earthquake Engineering Conference Proceedings*, Vancouver, Canada. paper no. 1098.

Graymer, R. W. (2000). *Geologic map and map database of the Oakland metropolitan area, Alameda, Contra Costa, and San Francisco Counties, California*. U.S. Geological Survey Map MF-2342. 1 sheet, scale 1:50,000, http://pubs.usgs.gov/mf/2000/2342/ (last accessed 2009/04/15).

Graymer, R. W., D. L. Jones, and E. E. Brabb (1995). Geologic map of the Hayward fault zone, Contra Costa, Alameda, and Santa Clara counties, California: a digital database. Open-File Report 95-597, U.S. Geological Survey.

Graymer, R. W., D. L. Jones, and E. E. Brabb (1996). Preliminary geologic map emphasizing bedrock formations in Alameda County, California: a digital database. Open-File Report 96-252, U.S. Geological Survey.

Graymer, R. W., V. E. Langenheim, R. W. Simpson, R. C. Jachens, and D. A. Ponce (2007a). Relatively simple through-going fault planes at large-earthquake depth may be concealed by the surface complexity of strike-slip faults, in tectonics of strike-slip restraining and releasing bends. In W. D. Cunningham and P. Mann (Eds.), *Tectonics of Strike-Slip Restraining and Releasing Bends*, Volume 290, pp. 189–201. Geological Society, London, Special Publications, doi: 10.1144/SP290.5.

Graymer, R. W., V. E. Langenheim, R. W. Simpson, R. C. Jachens, and D. A. Ponce (2007b). Relatively simple through-going fault planes at large-earthquake faults depth may be concealed by the surface complexity of strike-slip. In W. D. Cunningham and P. Mann (Eds.), *Tectonics of Strike-Slip Restraining and Releasing Bends*, Volume 290, pp. 189–201. London: Geological Society, doi: 10.1144/SP290.5.

Graymer, R. W., D. A. Ponce, R. C. Jachens, R. W. Simpson, and C. M. Wentworth (2005, June). Three-dimensional geologic map of the Hayward fault, northern California, correlation of rock units with variations in seismicity, creep rate, and fault dip. *Geology 33*(6), 521–524, doi: 10.1130/G21435.1.

Graymer, R. W., R. W. Simpson, R. C. Jachens, D. A. Ponce, G. A. Phelps, J. T. Watt, and C. M. Wentworth (2007). Segmentation of the Calaveras-Hayward fault system based on 3-D geometry and geology at large-earthquake depth. *EOS Trans. 88*(52). S21A-0239.

Hanks, T. C. and W. H. Bakun (2008). M-logA observations for recent large earthquakes. *Bulletin of the Seismological Society of America 98*(1), 490–494, doi: 10.1785/0120070174.

Hecker, S., D. Pantosti, D. P. Schwartz, J. C. Hamilton, L. M. Reidy, and T. J. Power (2005, June). The most recent large earthquake on the Rodgers Creek fault, San Francisco Bay Area. *Bulletin of the Seismological Society of America 95*(3), 844–860, doi: 10.1785/0120040134.

Idriss, M. (2008, February). An NGA empirical model for estimating the horizontal spectral values generated by shallow crustal earthquakes. *Earthquake Spectra 24*(1), 217–242, doi: 10.1193/1.2924362.

Jachens, R. C., C. M. Wentworth, M. L. Zoback, T. R. Bruns, and C. W. Roberts (2002). Concealed strands of the San Andreas fault system in central San Francisco Bay, as inferred from aeromagnetic anomalies, in crustal structure of the coastal marine San Francisco Bay region, California. In T. Parsons (Ed.), *Crustal Structure of the Coastal and Marine San Francisco Bay Region, California*, pp. 43–61. USGS Prof. Paper 1658.

Kagawa, T., K. Irikura, and P. G. Somerville (2004). Differences in ground motion and fault rupture process between the surface and buried rupture earthquakes. *Earth, Planets, and Space 56*(1), 3–14.

Lawson, A. (Ed.) (1908). *The California earthquake of April 18, 1906. Report of the State Earthquake Investigation Commission*. Washington, D.C.: Carnegie Institution of Washington.

Liekaemper, J. J. and P. L. Williams (1999). Evidence for surface rupture in 1868 on the Hayward fault in north Oakland and major rupturing in prehistoric earthquakes. *Geophysical Research Letters 26*(13), 1949–1952.

Liekaemper, J. J. and P. L. Williams (2007, December). A record of large earthquakes on the southern Hayward fault for the past 1800 years. *Bulletin of the Seismological Society of America 97*(6), 1803–1819, doi: 10.1785/0120060258.

Lienkaemper, J. J. (1992). *Map of recently active traces of the Hayward Fault, Alameda and Contra Costa Counties, California*. U.S. Geological Survey Miscellaneous Map MF-2196. scale 1:24,000, http://pubs.usgs.gov/mf/1992/2196/ (last accessed 2009/04/15).

Lienkaemper, J. J., B. Baker, and F. S. McFarland (2006, September). Surface slip associated with the 2004 Parkfield, California, earthquake measured on alinement arrays. *Bulletin of the Seismological Society of America 96*(48), S239–S249, doi: 10.1785/0120050806.

Lienkaemper, J. J., G. Borchardt, and M. Lisowski (1991). Historic creep rate and potential for seismic slip along the Hayward fault, California. *Journal of Geophysical Research - Solid Earth 96*(B11), 18261–18283.

Lienkaemper, J. J., D. P. Schwartz, K. I. Kelson, G. D. Simpson, J. R. Southon, J. A. Wanket, and P. L. Williams (1999). Timing of paleoearthquakes on the northern Hayward fault Preliminary evidence in El Cerrito, California. Open-File Report 99-318, U.S. Geological Survey. http://geopubs.wr.usgs.gov/open-file/of99-318/ (last accessed 4/27/2009).

Liu, P., R. J. Archuleta, and S. H. Hartzell (2006, December). Prediction of broadband ground-motion time histories: Hybrid low/high- frequency method with correlated random source parameters. *Bulletin of the Seismological Society of America 96*(6), 2118–2130, doi: 10.1785/0120060036.

Mai, P. M. and G. C. Beroza (2002, November 10). A spatial random field model to characterize complexity in earthquake slip. *Journal of Geophysical Research - Solid Earth 107*(B11), doi: 10.1029/2001JB000588.

Manaker, D. M., A. J. Michael, and R. Burgmann (2005, April). Subsurface structure and kinematics of the CalaverasHayward fault stepover from three-dimensional Vp and seismicity, San Francisco Bay region, California. *Bulletin of the Seismological Society of America 95*(2), 446–470, doi: 10.1785/0120020202.

Murray, J. and J. Langbein (2006, September). Slip on the San Andreas fault at Parkfield, California, over two earthquake cycles, and the implications for seismic hazard. *Bulletin of the Seismological Society of America 96*(4B), S283–S303, doi: 10.1785/0120050820.

Murray, J. and P. Segall (2002, September 19). Testing time-predictable earthquake recurrence by direct measurement of strain accumulation and release. *Nature 419*, 287–291, doi: 10.1038/nature00984.

Olsen, K. B., S. M. Day, J. B. Minster, Y. Cui, A. Chourasia, N. Faerman, R. Moore, P. Maechling, and T. Jordan (2006). Strong shaking in Los Angeles expected from southern San Andreas earthquake. *Geophysical Research Letters 33*(L07305), doi: 10.1029/2005GL025472.

Olsen, K. B., R. Madariaga, and R. J. Archuleta (1997, October 31). Three-dimensional dynamic simulation of the 1992 Landers earthquake. *Science 278*, 834–839.

Oppenheimer, D. H., W. H. Bakun, and A. G. Lindh (1990). Slip partitioning of the Calaveras fault, California, and prospects for future earthquakes. *Journal of Geophysical Research - Solid Earth 95*(B6), 8483–8498.

Parsons, T., R. Sliter, E. L. Geist, R. C. Jachens, B. E. Jaffe, A. Foxgrover, P. E. Hart, and J. McCarthy (2003, October). Structure and mechanics of the Hayward-Rodgers Creek fault step-over, San Francisco Bay, California. *Bulletin of the Seismological Society of America 93*(5), 2187–2200, doi: 10.1785/0120020228.

Peyrat, S., K. Olsen, and R. Madariaga (2001, November 10). Dynamic modeling of the 1992 Landers earthquake. *Journal of Geophysical Research - Solid Earth 106*(B11), 26467–26482, doi: 10.1029/2001JB000205.

Phelps, G. A., R. W. Graymer, R. C. Jachens, D. A. Ponce, R. W. Simpson, and C. M. Wentworth (2008). *Three-Dimensional Geologic Map of the Hayward Fault Zone, San Francisco Bay Region, California*. U.S. Geological Survey Scientific Investigations Map 3045. http://pubs.usgs.gov/sim/3045/ (last accessed 2009/04/15).

Pollitz, F. F. and D. P. Schwartz (2008). Probabilistic seismic hazard in the San Francisco Bay area based on a simplified viscoelastic cycle model of fault interactions. *Journal of Geophysical Research - Solid Earth 113*(B05409), doi: 10.1029/2007JB005227.

Ponce, D. A., R. W. Graymer, T. G. Hildebrand, R. C. Jachens, and R. W. Simpson (2007). Geophysical investigations along the Hayward fault, Northern California, and their implications on earthquake hazards. *EOS Trans. 88*(52). S21A-0241.

Ponce, D. A., R. W. Graymer, R. C. Jachens, and R. W. Simpson (XXXX). In search of segment boundaries along the Hayward fault and implications on earthquake hazards. In *Proceedings of the third conference on earthquake hazards in the eastern San Francisco Bay area: Science, hazard, engineering and risk*. California Geological Survey.

Ponce, D. A., T. G. Hildebrand, and R. C. Jachens (2003, February). Gravity and magnetic expression of the San Leandro gabbro with implications for the geometry and evolution of the Hayward fault zone, northern California. *Bulletin of the Seismological Society of America 93*(1), 14–26, doi: 10.1785/0120020013.

Ponce, D. A., R. W. Simpson, R. W. Graymer, and R. C. Jachens (2004). Gravity, magnetic, and high-precision relocated seismicity profiles suggest a connection between the Hayward and Calaveras faults, northern California. *Geochemistry, Geophysics, Geosystems 5*(Q07004), doi: 10.1029/2003GC000684.

Schmedes, J., R. J. Archuleta, and D. Lavalle. Correlation of earthquake source parameters inferred from dynamic rupture simulations. *Journal of Geophysical Research - Solid Earth*, doi: 10.1029/2009JB006689. in press.

Schmidt, D. A., R. Burgmann, R. M. Nadeau, and M. d'Alessio (2005). Distribution of aseismic slip rate on the Hayward fault inferred from seismic and geodetic data. *Journal of Geophysical Research - Solid Earth 110*(B08406), doi: 10.1029/2004JB003397.

Sharp, R. V., K. E. Budding, J. Boatwright, M. J. Ader, M. G. Bonilla, M. M. Clark, T. E. Fumal, K. K. Harms, J. J. Lienkaemper, D. M. Morton, B. J. O'Neill, C. L. Ostergren, D. J. Ponti, M. J. Rymer, J. L. Saxton, and J. Sims (1989, April). Surface faulting along the Superstition Hills fault zone and nearby faults associated with the earthquakes of 24 November 1987. *Bulletin of the Seismological Society of America 79*(2), 252–281.

Shimazaki, K. and T. Nakata (1980). Time-predictable recurrence model for large earthquakes. *Geophysical Research Letters 7*(4), 279–282.

Simpson, R. W., R. W. Graymer, R. C. Jachens, D. A. Ponce, and C. M. Wentworth (2004). Cross-sections and maps showing double-difference relocated earthquakes from 1984-2000 along the Hayward and Calaveras faults, California. Open-File Report 2004-1083, U.S. Geological Survey.

Simpson, R. W., J. J. Lienkaemper, and J. S. Galehouse (2001). Variations in creep rate along the Hayward fault, California, interpreted as changes in depth of creep. *Geophysical Research Letters 28*(11), 2269–2272.

Somerville, P. G., K. Irikura, R. Graves, S. Sawada, D. Wald, N. Abrahamson, Y. Iwasaki, T. Kagawa, N. Smith, and A. Kowada (1999, January/February). Characterizing crustal earthquake slip models for the prediction of strong ground motion. *Seismological Research Letters 70*(1), 199–222.

Somerville, P. G., N. F. Smith, R. W. Graves, and N. A. Abrahamson (1997, January/February). Modification of empirical strong ground motion attenuation relations to include the amplitude and duration effects of rupture directivity. *Seismological Research Letters 68*(1), 199–222.

Song, S. G., A. Pitarka, and P. Somerville (2009, August). Exploring spatial coherence between earthquake source parameters. *Bulletin of the Seismological Society of America 99*(4), 2564–2571, doi: 10.1785/0120080197.

Spudich, P. and M. Guatteri (2004, December). The effect of bandwidth limitations on the inference of earthquake slip-weakening distance from seismograms. *Bulletin of the Seismological Society of America 94*(6), 2028–2036, doi: 10.1785/0120030104.

Stoffer, P. (2008). Where's the Hayward fault? a green guide to the fault. Open-File Report 2008-1135, U.S. Geological Survey. http://pubs.usgs.gov/of/2008/1135/.

Tinti, E., E. Fukuyama, A. Piatanesi, and M. Cocco (2005, August). A kinematic source-time function compatible with earthquake dynamics. *Bulletin of the Seismological Society of America 95*(4), 1211–1223, doi: 10.1785/0120040177.

Wald, D., B. Worden, V. Quitoriano, and K. Pankow (2005, May). *ShakeMap Manual: Technical Manual, Users Guide, and Software Guide* (Version 1.0 ed.). United States Geological Survey. http://pubs.usgs.gov/tm/2005/12A01/.

Waldhauser, F. and W. L. Ellsworth (2002). Fault structure and mechanics of the Hayward fault, California, from double-difference earthquake locations. *Journal of Geophysical Research - Solid Earth 107*(B3), doi: 10.1029/2000JB000084.

Watt, J. T., D. A. Ponce, R. W. Graymer, R. W. Simpson, and R. C. Jachens (XXXX). The Mt. Lewis fault zone: Tectonic implications for eastern San Francisco Bay Area. In *Proceedings of the third conference on earthquake hazards in the eastern San Francisco Bay area: Science, hazard, engineering and risk*. California Geological Survey.

Wells, D. L. and K. J. Coppersmith (1994, August). New empirical relationships among magnitude, rupture length, rupture width, rupture area, and surface displacement. *Bulletin of the Seismological Society of America 84*(4), 974–1002.

Wentworth, C. M., J. Blake, M. C., R. J. McLaughlin, and R. W. Graymer (1999). Preliminary geologic map of the San Jose 30x60-minute quadrangle, California; a digital database. Open-File Report 98-795, U.S. Geological Survey.

Wessel, P. and W. H. F. Smith (1998). New, improved version of the generic mapping tools released. *EOS Transactions 79*, 579.

Working Group on California Earthquake Probabilities (WGCEP) (1988). Probabilities of large earthquakes occurring in California on the San Andreas fault. Open-File Report 88-398, U.S. Geological Survey.

Working Group on California Earthquake Probabilities (WGCEP) (1990). Probabilities of large earthquakes in the San Francisco Bay region, California. U.S. Geological Survey Circular 1053, U.S. Geological Survey.

Working Group on California Earthquake Probabilities (WGCEP) (1999). Earthquake probabilities in the San Francisco Bay region: 2000–2030 – a summary of findings. Open-File Report 99-517, U.S. Geological Survey.

Working Group on California Earthquake Probabilities (WGCEP) (2003). Earthquake probabilities in the San Francisco Bay region: 2002–2031. Open-File Report 03-214, U.S. Geological Survey.

Working Group on California Earthquake Probabilities (WGCEP) (2008). The uniform California earthquake rupture forecast, version 2 (UCERF 2). Open-File Report 2007-1437, U.S. Geological Survey. http://pubs.usgs.gov/of/2007/1437/ (last accessed 2/18/2009).

Wyss, M. (2001). Locked and creeping patches along the Hayward fault, California. *Geophysical Research Letters 28*(18), 3537–3540.

Yu, E. and P. Segall (1996). Slip in the 1868 Hayward earthquake from the analysis of historical triangulation data. *Journal of Geophysical Research - Solid Earth 101*(B7), 16101–16118, doi: 10.1029/96JB00806.

Zhao, D., H. Kanamori, H. Negishi, and D. Wiens (1996, December 13). Tomography of the source area of the 1995 Kobe earthquake: Evidence for fluids at the hypocenter? *Science 274*(5294), 1891–1894, doi: 10.1126/science.274.5294.1891.

U.S. Geological Survey, MS977
345 Middlefield Rd.
Menlo Park, CA 94025
(B.T.A., D.S.)

U.S. Geological Survey, MS975
345 Middlefield Rd.
Menlo Park, CA 94025
(R.W. Graymer)

U.S. Geological Survey, MS989
345 Middlefield Rd.
Menlo Park, CA 94025
(D.A.P.)

URS Corporation
566 El Dorado St.
Pasadena, CA 91101
(R.W. Graves)

Table 1. Rupture Dimensions and Epicenters

Rupture	Epicenters	Rupture length	Slip distribution			
			Slip-gradient	Slip-predictable	No creep	Full creep
HS	O, H, F	54 km	G01, G02 (Mw 6.76)	P01 (Mw 6.84)	N01 (Mw 6.89)	F01 (Mw 6.61)
HS+HN	SPB, H, F	83 km	G04 (Mw 7.05)	P03 (Mw 6.97)	N04 (Mw 7.12)	F04 (Mw 6.82)
CC+HS	O, H, AR	77 km	G03 (Mw 6.90)	P02 (Mw 6.94)	n/a	n/a
HN+RC	SPB	91 km	G05 (Mw 6.89)	P04 (Mw 7.11)	n/a	n/a
HS+HN+RC	SPB	145 km	G06 (Mw 7.16)	P05 (Mw 7.20)	n/a	n/a

The rupture segments are Hayward South (HS), Hayward North (HN), Central Calaveras (CC), and Rodgers Creek (RC). The epicenters (see Table 2 for precise locations) are San Pablo Bay (SPB), Oakland (O), Hayward (H), Fremont (F), and Alum Rock (AR). The different approaches accounting for creep result in different slip distributions and magnitude events for the same rupture area. The slip distributions G01 and G02 use the same background slip distribution but different stochastic distributions.

Table 2. Hypocenter Locations

Hypocenter	Longitude	Latitude	Comments
San Pablo Bay	-122.4080	38.0964	Right stepover
Oakland	-122.1786	37.8046	Northern extent of San Leandro gabbro
Hayward	-122.0452	37.6700	
Fremont	-121.9033	37.5349	Near southern extent of the 1868 rupture
Alum Rock	-121.7862	37.4416	Junction of the Hayward and Calaveras faults

All hypocenters are at an elevation of -8.0 km. Longitude and latitude are given in the WGS84 horizontal datum.

Table 3. Earthquake Scenarios

Name	Rupture Segments	Slip Distribution	Hypocenter	Rupture Speed	Rise Time	Moment Magnitude
HS G01 HypoO	HS	G01	Oakland	*Vr92*	*Tr15*	6.76
HS G01 HypoH	HS	G01	Hayward	*Vr92*	*Tr15*	6.76
HS G01 HypoF	HS	G01	Fremont	*Vr92*	*Tr15*	6.76
HS G02 HypoO	HS	G02	Oakland	*Vr92*	*Tr15*	6.76
HS G02 HypoH	HS	G02	Hayward	*Vr92*	*Tr15*	6.76
HS G02 HypoF	HS	G02	Fremont	*Vr92*	*Tr15*	6.76
HS P01 HypoO	HS	P01	Oakland	*Vr92*	*Tr15*	6.84
HS P01 HypoH	HS	P01	Hayward	*Vr92*	*Tr15*	6.84
HS P01 HypoF	HS	P01	Fremont	*Vr92*	*Tr15*	6.84
HS+HN G04 HypoSPB	HS+HN	G04	San Pablo Bay	*Vr92*	*Tr15*	7.05
HS+HN G04 HypoO	HS+HN	G04	Oakland	*Vr92*	*Tr15*	7.05
HS+HN G04 HypoF	HS+HN	G04	Fremont	*Vr92*	*Tr15*	7.05
HS+HN P03 HypoSPB	HS+HN	P03	San Pablo Bay	*Vr92*	*Tr15*	6.97
HS+HN P03 HypoO	HS+HN	P03	Oakland	*Vr92*	*Tr15*	6.97
HS+HN P03 HypoF	HS+HN	P03	Fremont	*Vr92*	*Tr15*	6.97
CC+HS G03 HypoO	CC+HS	G03	Oakland	*Vr92*	*Tr15*	6.90
CC+HS G03 HypoH	CC+HS	G03	Hayward	*Vr92*	*Tr15*	6.90
CC+HS G03 HypoAR	CC+HS	G03	Alum rock	*Vr92*	*Tr15*	6.90
CC+HS P02 HypoO	CC+HS	P02	Oakland	*Vr92*	*Tr15*	6.94
CC+HS P02 HypoH	CC+HS	P02	Hayward	*Vr92*	*Tr15*	6.94
CC+HS P02 HypoAR	CC+HS	P02	Alum Rock	*Vr92*	*Tr15*	6.94
HN+RC G05 HypoSPB	HN+RC	G05	San Pablo Bay	*Vr92*	*Tr15*	6.89
HN+RC P04 HypoSPB	HN+RC	P04	San Pablo Bay	*Vr92*	*Tr15*	7.11
HS+HN+RC G06 HypoSPB	HS+HN+RC	G06	San Pablo Bay	*Vr92*	*Tr15*	7.16
HS+HN+RC P05 HypoSPB	HS+HN+RC	P05	San Pablo Bay	*Vr92*	*Tr15*	7.20
HS Vr82	HS	*G01*	*Hayward*	Vr82	*Tr15*	6.76
HS Vr141	HS	*G01*	*Hayward*	Vr141	*Tr15*	6.76
HS+HN Vr82	HS+HN	*G04*	*Oakland*	Vr82	*Tr15*	7.05
HS+HN Vr141	HS+HN	*G04*	*Oakland*	Vr141	*Tr15*	7.05
HS Tr10	HS	*G01*	*Hayward*	*Vr92*	Tr10	6.76
HS Tr20	HS	*G01*	*Hayward*	*Vr92*	Tr20	6.76
HS Tr10u	HS	*G01*	*Hayward*	*Vr92*	Tr10u	6.76
HS+HN Tr10	HS+HN	*G04*	*Oakland*	*Vr92*	Tr10	7.05
HS+HN Tr20	HS+HN	*G04*	*Oakland*	*Vr92*	Tr20	7.05
HS+HN Tr20u	HS+HN	*G04*	*Oakland*	*Vr92*	Tr20u	7.05
HS N01	HS	N01	*Hayward*	*Vr92*	*Tr15*	6.89
HS F01	HS	F01	*Hayward*	*Vr92*	*Tr15*	6.61
HS+HN N04	HS+HN	N04	*Oakland*	*Vr92*	*Tr15*	7.12
HS+HN F04	HS+HN	F04	*Oakland*	*Vr92*	*Tr15*	6.82

Figure 1 shows the rupture lengths and epicenters. The rise time labels Tr10, Tr15, and Tr20 correspond to values of 1.0, 1.5, and 2.0 for C in the expression for the rise time, $t_{95}/t_0 = C\sqrt{D_f/D_0}$, and the labels Tr10u and Tr20u correspond to nominally uniform rise times of 1.0 s and 2.0 s. The rupture speed labels Vr92, Vr82, and Vr141 correspond to the correlations between rupture speed and slip. The maximum local rupture speeds for Vr92, Vr82, and Vr141 are 0.92 Vs, 0.82 Vs, and $\sqrt{2}$ Vs, respectively. We form the scenario names from abbreviations of the parameters but do not include parameters with significant redundancy (which are shown in italics).

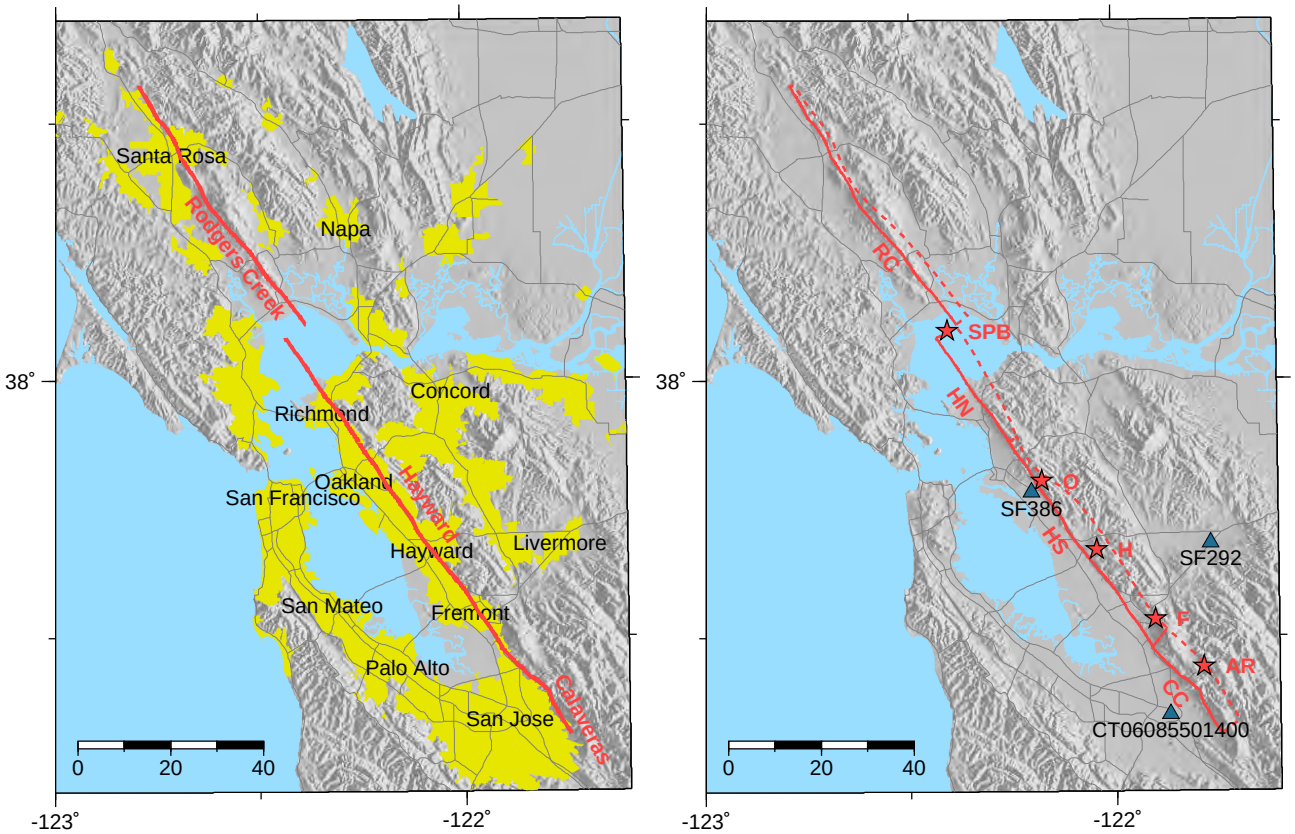

Figure 1. The left panel shows a map of the urban area (yellow shaded region) and the extent of rupture on the surface traces (red lines) of the scenarios for the Hayward, Rodgers Creek, and Calaveras faults. The right panel shows the four rupture segments (surfaces traces in solid red lines and down-dip extent of rupture in dashed red lines) which are combined into the five rupture lengths. The epicenters (stars) are offset from the surface trace due to the 3-D geometry of the fault surface. The rupture segments include the Central Calaveras (CC), Hayward South (HS), Hayward North (HN), and Rodgers Creek (RC). The epicenters include San Pablo Bay (SPB), Oakland (O), Hayward (H), Fremont (F), and Alum Rock (AR). We discuss velocity waveforms for the sites indicated by the blue triangles.

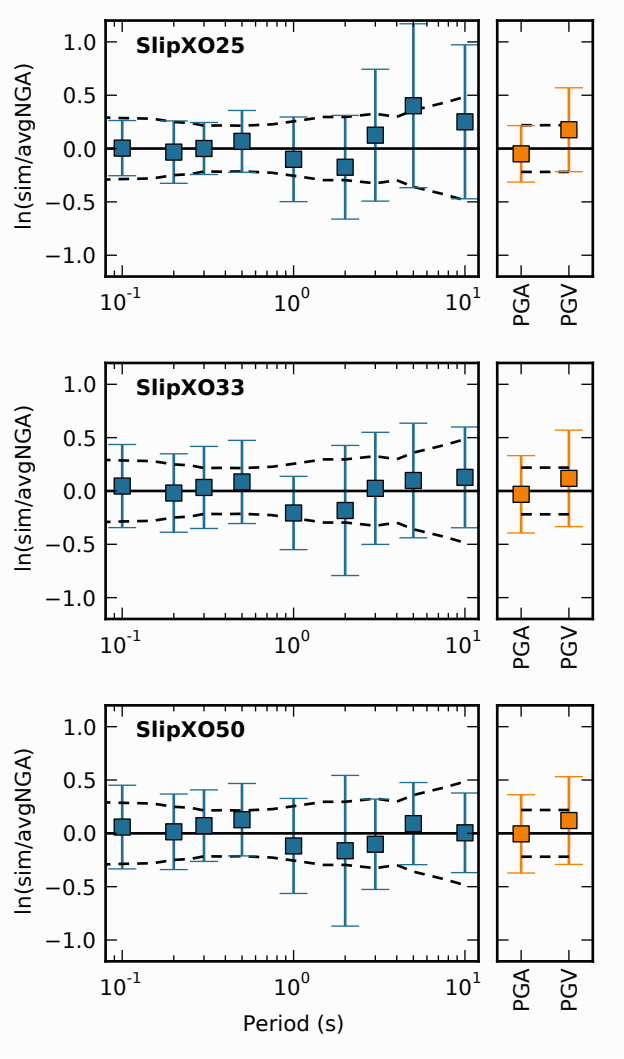

Figure 2. Residuals between 1-D simulation and the average of four ground-motion prediction equations for cross-over length scales between the background and stochastic slip distributions of 25% (SlipXO25), 33% (SlipXO33) and 50% (SlipXO50) of the rupture length. Error bars indicate one standard deviation for the residuals, and dashed lines indicate one standard deviation of the inter-event term of the CB08 ground-motion prediction equation.

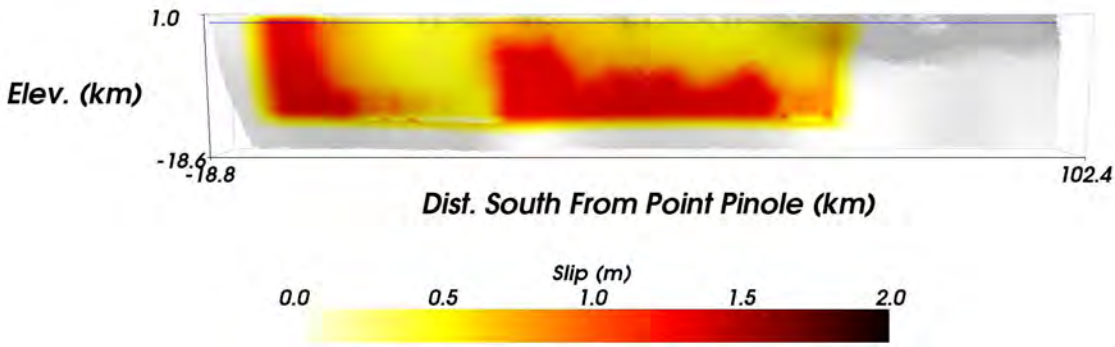

Figure 3. Plot of nominal slip distribution for the slip-predictable approach for accounting for creep for the Hayward South + North rupture length.

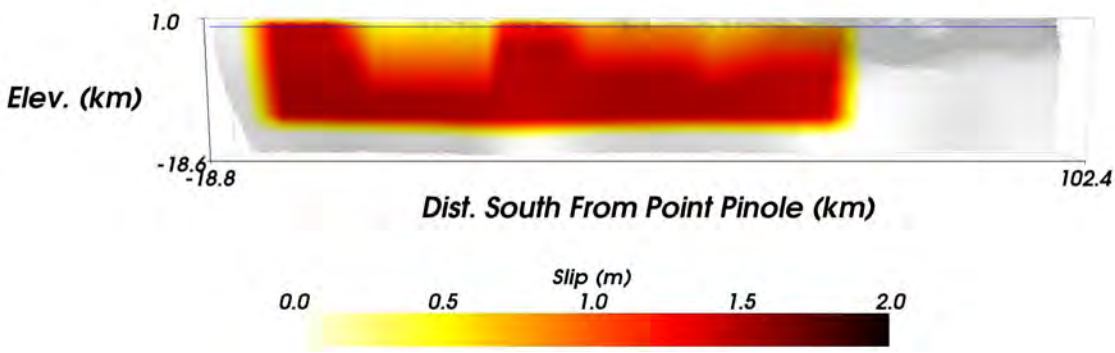

Figure 4. Plot of nominal slip distribution for the slip-gradient approach for accounting for creep for the Hayward South + North rupture length.

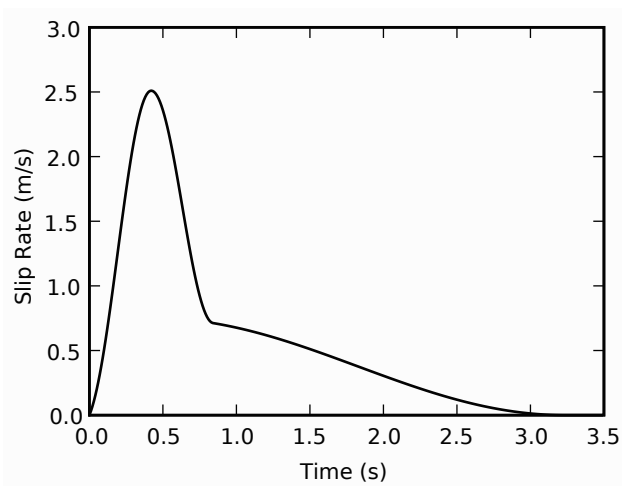

Figure 5. Plot of cosine-sine slip time function. The rise time corresponds to C = 1.5 in equation (11).

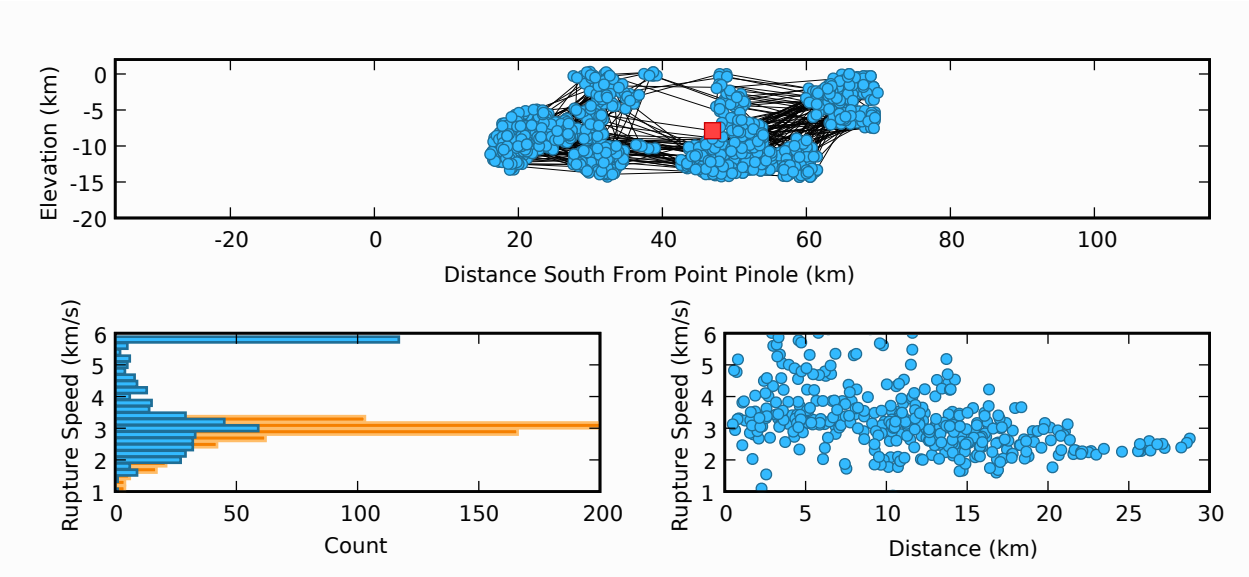

Figure 6. The top panel shows pairs of points used to assess the rupture speed for scenario HS G01 HypoH. The lower left panel displays a histogram of the rupture speed measured from the point pairs (blue) and the local rupture speed (orange). The lower right panel shows the rupture speeds as a function of distance between the points.

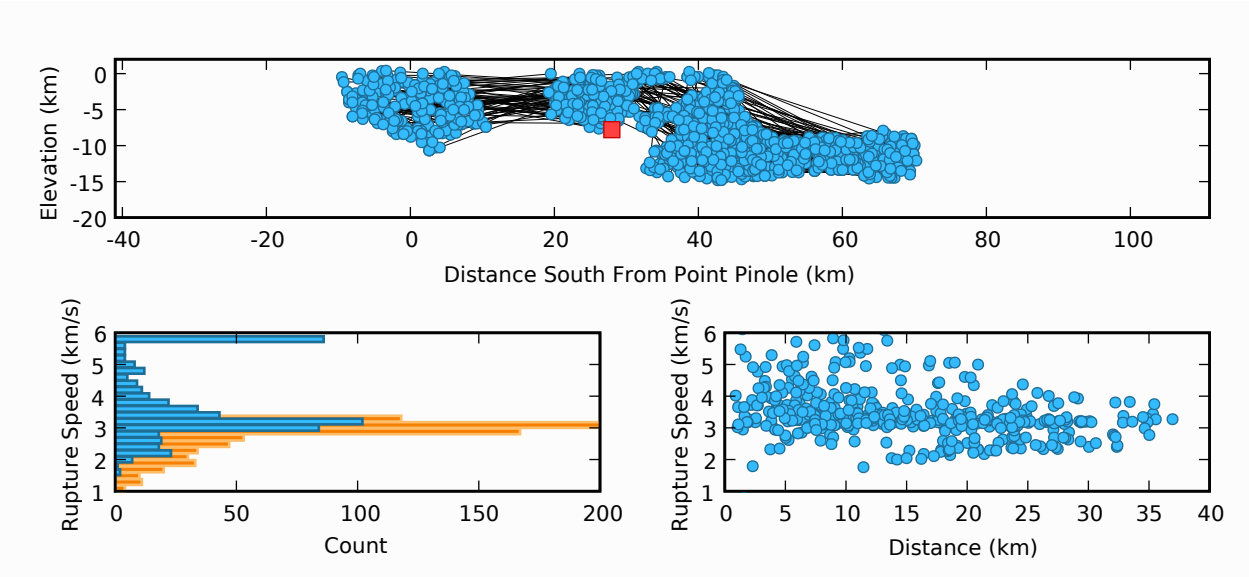

Figure 7. The top panel shows pairs of points used to assess the rupture speed for scenario HS+HN G04 HypoO. The lower left panel displays a histogram of the rupture speed measured from the point pairs (blue) and the local rupture speed (orange). The lower right panel shows the rupture speeds as a function of distance between the points.

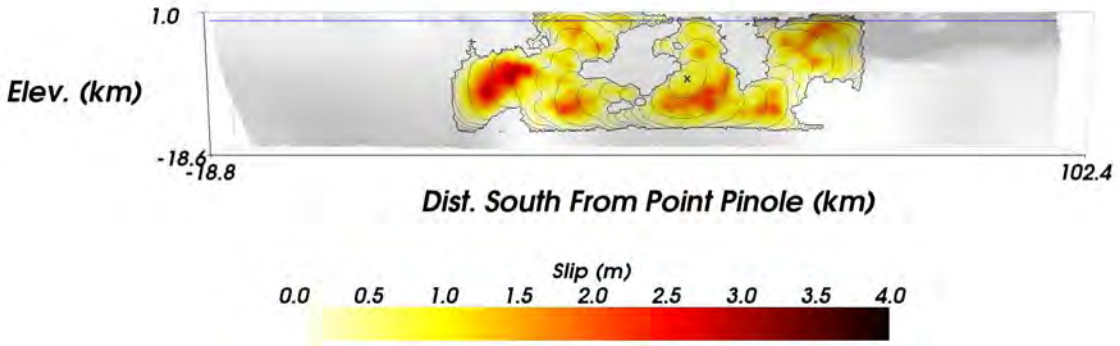

Figure 8. Plot of slip and slip initiation time (contour interval is 1.0 s) for the HS G01 HypoH rupture model. The black x denotes the hypocenter.

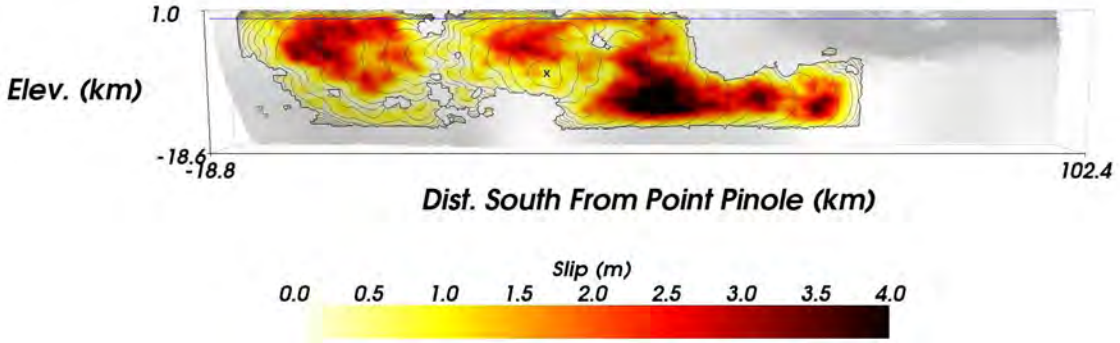

Figure 9. Plot of slip and slip initiation time (contour interval is 1.0 s) for the HS+HN G04 HypoO rupture model. The black x denotes the hypocenter.

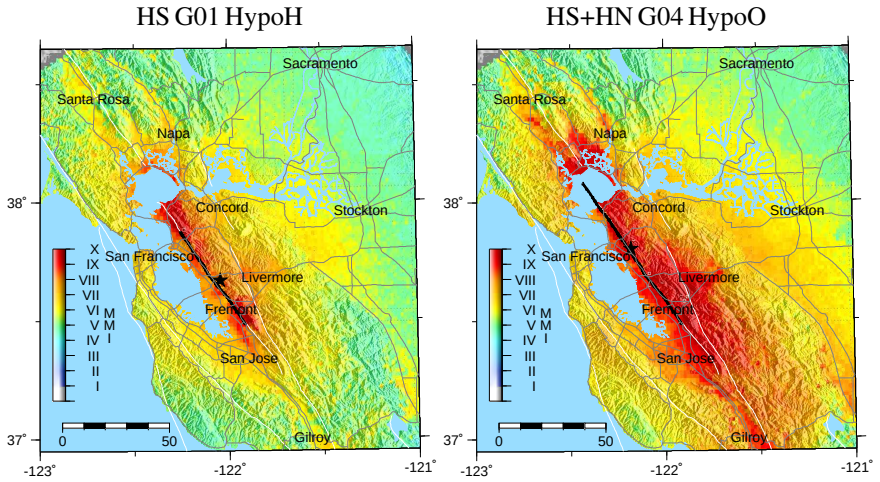

Figure 10. Maps of Modified Mercalli Intensity (MMI) for Graves's broadband (T > 0.1 s) simulations of a bilateral Mw 6.76 Hayward South scenario earthquake (scenario HS G01 HypoH) and a bilateral Mw 7.05 Hayward South + North scenario earthquake (scenario HS+HN G04 HypoO). The scenarios use the simple slip-gradient approach to account for creep.

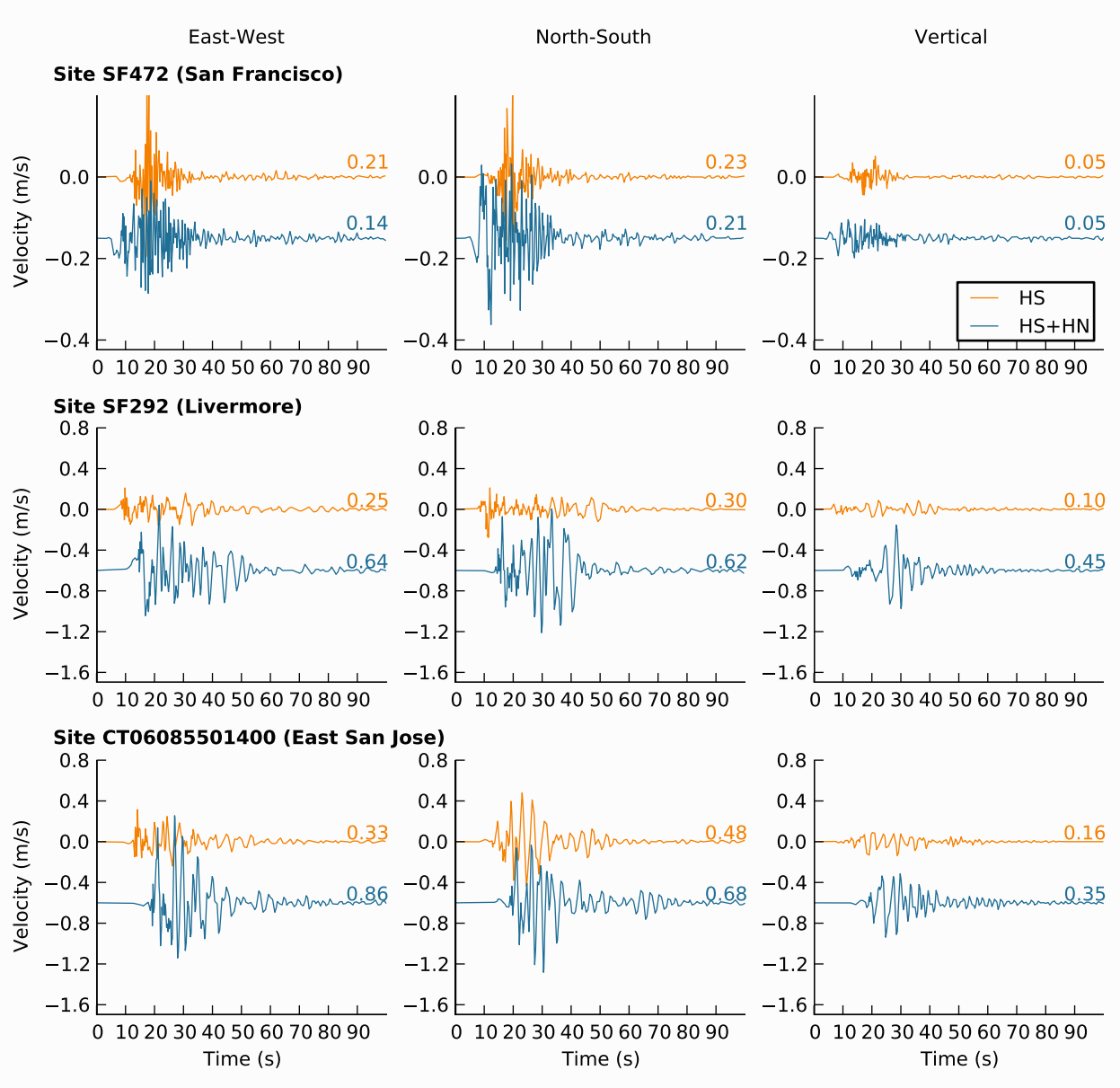

Figure 11. Velocity waveforms at sites in Oakland (SF386), Livermore (SF292), and San Jose (CT06085501400) from Graves's broadband (T > 0.1 s) simulations of a bilateral Mw 6.76 Hayward South scenario earthquake (scenario HS G01 HypoH, HS in legend) and a bilateral Mw 7.05 Hayward South + North scenario earthquake (scenario HS+HN G04 HypoO, HS+HN in legend). The traces for scenario HS+HN G04 HypoO are plotted on the same scale but offset vertically from the corresponding traces for scenario HS G01 HypoH. The value on the right side of each trace indicates the peak velocity. See Figure 1 for site locations.

Ground-motion modeling of Hayward fault scenario earthquakes II: Simulation of long-period and broadband ground motions

by Brad T. Aagaard, Robert W. Graves, Arthur Rodgers, Thomas M. Brocher, Robert W. Simpson, Douglas Dreger, N. Anders Petersson, Shawn C. Larsen, Shuo Ma, and Robert C. Jachens

May 13, 2010

For submission to BSSA

Abstract We simulate long-period (T > 1.0–2.0 s) and broadband (T > 0.1 s) ground motions for 39 scenarios earthquakes (Mw 6.7–7.2) involving the Hayward, Calaveras, and Rodgers Creek faults. For rupture on the Hayward fault we consider the effects of creep on coseismic slip using two different approaches, both of which reduce the ground motions compared with neglecting the influence of creep. Nevertheless, the scenario earthquakes generate strong shaking throughout the San Francisco Bay area with about 50% of the urban area experiencing MMI VII or greater for the magnitude 7.0 scenario events. Long-period simulations of the 2007 Mw 4.18 Oakland and 2007 Mw 5.45 Alum Rock earthquakes show that the USGS Bay Area Velocity Model version 08.3.0 permits simulation of the amplitude and duration of shaking throughout the San Francisco Bay area for Hayward fault earthquakes, with the greatest accuracy in the Santa Clara Valley (San Jose area). The ground motions exhibit a strong sensitivity to the rupture length (or magnitude), hypocenter (or rupture directivity), and slip distribution. The ground motions display a much weaker sensitivity to the rise time and rupture speed. Peak velocities, peak accelerations, and spectral accelerations from the synthetic broadband ground motions are, on average, slightly higher than the Next Generation Attenuation (NGA) ground-motion prediction equations. We attribute much of this difference to the seismic velocity structure in the San Francisco Bay area and how the NGA models account for basin amplification; the NGA relations may under-predict amplification in shallow sedimentary basins. The simulations also suggest that the Spudich and Chiou (2008) directivity corrections to the NGA relations could be improved by increasing the areal extent of rupture directivity with period.

Introduction

The most recent large rupture of the Hayward fault, a magnitude 6.8 event (Bakun, 1999), occurred on 21 October 1868 and caused widespread damage throughout the sparsely populated region east of San Francisco Bay and significant damage in the city of San Francisco (Boatwright and Bundock, 2008). Moreover, as a result of the level of damage in San Francisco, the 1868 earthquake was called the "Great San Francisco Earthquake" until the 18 April 1906 magnitude 7.9 earthquake (Stover and Coffman, 1993). The San Francisco Bay area is currently home to approximately seven million people (2000 census) with heavy urbanization along the entire length of the Hayward fault. In this study we compute ground motions for a wide variety of plausible ruptures on the Hayward-Rodgers Creek fault system, which carries the highest probability of producing a magnitude 6.7 or larger event in the next 30 years (WGCEP, 2008). We employ of a suite of 39 earthquake scenarios involving rupture of the Hayward fault. Part I (Aagaard *et al*., 2010) discusses the construction of the scenarios in detail. Some of the scenarios also involve rupture of a 23 km portion of the Calaveras fault (six scenarios) or rupture of the Rodgers Creek fault (four scenarios).

In previous work we estimated ground motions for the 1906 earthquake and scenarios rupturing that same 480 km portion of the northern San Andreas fault (Aagaard *et al*., 2008a) as well as the 1989 magnitude 6.9 Loma Prieta earthquake (Aagaard *et al*., 2008b). The simulations demonstrated consistent amplification of shaking associated with sedimentary basins, such as the Cupertino Basin west of San Jose, the Cotati and Windsor basins under Santa Rosa, the Livermore basin, and the Great Valley. The pattern of shaking within the San Francisco Bay urban region also displayed a strong sensitivity to the hypocenter with significantly stronger shaking for north-to-south rupture compared to south-to-north rupture. Although we attribute some of this observation to the location of a majority of the urban area lying south of San Francisco and Oakland, the geologic structure also appears to play a significant role. Having characterized the ground motions generated by ruptures along the San Andreas fault on the west side of San Francisco Bay, in this study we focus on ground motions generated by ruptures of the Hayward, Rodgers Creek, and Calaveras faults on the east side of San Francisco Bay.

Larsen *et al*. (2000) simulated long-period ground motions for 20 Mw 7.0 scenario events on the Hayward fault using a simple 3-D seismic velocity model. They found high amplitude motions in the sedimentary basins, such as the San Pablo basin underneath San Pablo Bay, the Evergreen basin in the Santa Clara Valley, and the Livermore basin in the Livermore Valley. Harmsen *et al*. (2008) improved the characterization of ground motions from large earthquakes on the Hayward fault by studying the long-period ($T > 1.0$ s) ground motions in the Santa Clara Valley from six scenario events that included variations in the magnitude, hypocenter, rupture speed, and seismic velocity model. These six scenarios were part of a large suite of 20 scenarios with ruptures on other faults in the region. The six Hayward earthquakes involved rupture of 57 km of the southern portion of the Hayward fault in Mw 6.9 and Mw

7.0 events. Harmsen *et al*. (2008) noted a strong dependence of the peak ground velocity on the hypocenter and significant basin amplification, particularly in the Evergreen basin east of San Jose.

Whereas Harmsen *et al*. (2008) focus on the variability of ground motions in the Santa Clara Valley for a variety of earthquake sources, including six Hayward fault ruptures, in this study we focus on the ground motions throughout the San Francisco Bay area for a larger suite of Hayward fault scenarios, some of which include rupture on additional faults. Harmsen *et al*. (2008) did not include the effects of large regions with creep (aseismic slip) on the coseismic slip distribution, but did prescribe a uniform tapering in slip at depths above 5 km to limit the contribution of shallow slip to the ground motions. As described in Aagaard *et al*. (2010) we include two different approaches that account for the effects of creep on the coseismic slip distribution. Thus, we build upon the efforts of Harmsen *et al*. (2008) in our suite of 39 scenarios by including variations in the rupture length, slip distribution, hypocenter, rise time, rupture speed, and how creep affects the coseismic slip distribution.

Wave Propagation Codes

Simulation of ground motions for the 39 scenario events involved five different ground-motion modeling groups, Aagaard, Graves, Larsen, Ma, and Rodgers, each using a different wave propagation code. As we will discuss later, each group computed ground motions for two well-recorded moderate earthquakes and a common subset of the scenario earthquakes. These simulations demonstrate consistency among the modeling groups and permit tying together results from the different modeling groups' exploration of a subset of the scenarios. The codes employed by Aagaard, Graves, Larsen, and Rodgers (Larsen and Schultz, 1995; Graves, 1996; Aagaard *et al*., 2001; Nilsson *et al*., 2007) were used in studies of the 1906 earthquake (Aagaard *et al*., 2008a) and the 1989 Loma Prieta earthquake (Aagaard *et al*., 2008b). Since the simulations of the 1906 earthquake, the code used by Rodgers has been improved to include topography using a curvilinear grid approach (Appelö and Petersson, 2008). Ma previously applied his code (Ma and Liu, 2006) to study wave propagation in the 3-D heterogeneous structure of southern California (Ma *et al*., 2008) and examine the effects of topography (Ma *et al*., 2007).

Table 1 and Figure 1 summarize the modeling domains and features of the wave propagation codes used in this study. The domains generally span the region covered by the detailed portion of the USGS Bay Area Velocity Model 08.3.0, which we discuss in the next section. Graves and Larsen resolve waves with periods greater than 1.0 s, whereas Aagaard, Ma, and Rodgers resolve periods greater than 2.0 s. Each of the modeling groups imposes a minimum shear-wave speed of 500 m/s to 700 m/s in their simulations. These choices for the minimum period and shear-wave speed reflect the computational resources available to each group and the overall efficiency of the wave propagation

implementation. The similar choices for the minimum shear-wave speed contribute to the strong consistency among the modeling groups.

The seismic velocity model includes topography, so the ground-motion simulations either explicitly include topography or warp the seismic velocity model by "squashing" the topography into a flat planar surface. In "squashing" the uppermost portion of the earth (usually a few kilometers thick) is deformed in the vertical direction so that the free-surface is flat and aligned at reference elevation, typically sea level (Harmsen *et al*., 2008; Aagaard *et al*., 2008b). At the bottom of this deformed surface layer, the physical properties are blended with those of the lower, undeformed region. This technique is preferable to the "bulldozing" approach which flattens the earth by stripping away all material above some elevation and filling in voids below this elevation with some generic material, because it retains near-surface low-velocity materials (Aagaard *et al*., 2008b). Including or excluding topography has relatively little effect on the ground motions in our suite of simulations due to the relatively low relief in the San Francisco Bay area and the long wavelengths considered in the simulations.

As discussed in Part I, we use the cosine-sine slip-time function developed by Liu *et al*. (2006),

$$D(t) = \begin{cases} D_f C_n \left(0.7t - 0.7\frac{\tau_1}{\pi}\sin\frac{\pi t}{\tau_1} - 1.2\frac{\tau_1}{\pi}\left(\cos\frac{\pi t}{2\tau_1} - 1\right)\right) & 0 \le t < \tau_1 \\ D_f C_n \left(1.0t - 0.7\frac{\tau_1}{\pi}\sin\frac{\pi t}{\tau_1} + 0.3\frac{\tau_2}{\pi}\sin\frac{\pi(t-\tau_1)}{\tau_2} + \frac{1.2}{\pi}\tau_1 - 0.3\tau_1\right) & \tau_1 \le t < 2\tau_1 \\ D_f C_n \left(0.3t + 0.3\frac{\tau_2}{\pi}\sin\frac{\pi(t-\tau_1)}{\tau_2} + \frac{1.2}{\pi}\tau_1 + 1.1\tau_1\right) & 2\tau_1 \le t < \tau \end{cases} \tag{1}$$

$$\dot{D}(t) = \begin{cases} D_f C_n \left(0.7 - 0.7\cos\frac{\pi t}{\tau_1} + 0.6\sin\frac{\pi t}{2\tau_1}\right) & 0 \le t < \tau_1 \\ D_f C_n \left(1.0 - 0.7\cos\frac{\pi t}{\tau_1} + 0.3\cos\frac{\pi(t-\tau_1)}{\tau_2}\right) & \tau_1 \le t < 2\tau_1 \\ D_f C_n \left(0.3 + 0.3\cos\frac{\pi(t-\tau_1)}{\tau_2}\right) & 2\tau_1 \le t < \tau \end{cases} \tag{2}$$

$$C_n = \frac{\pi}{1.4\pi\tau_1 + 1.2\tau_1 + 0.3\pi\tau_2} \tag{3}$$

$$\tau = 1.525 t_{95} \tag{4}$$

$$\tau_1 = 0.13\tau \tag{5}$$

$$\tau_2 = \tau - \tau_1 \tag{6}$$

where $D(t)$ is the slip at time t, D_f is the final slip, t_{95} is the rise time (as measured by the time it takes for 95% of the slip to occur), and τ, τ_1, τ_2, and C_n are constants.

Seismic Velocity Model

For this study we updated version 05.1.0 of the USGS Bay Area Velocity Model that we used for calculating the ground motions for the 1906 earthquake (Aagaard *et al*., 2008a; Aagaard *et al*., 2008b). Waveform modeling (30 s $>$ T $>$ 4 s) of moderate earthquakes (Mw 4–5) in the San Francisco Bay region showed that version 05.1.0 of the model

predicted surface waves arriving about 5% faster than observed (Rodgers *et al*., 2008). Analysis of arrival times for small to moderate earthquakes and refraction shots confirmed a bias of about 5% too fast for both dilatational-wave speed (Vp) and the shear-wave speed (Vs) in version 05.1.0 of the model (Douglas Dreger, written comm., 2007). To quantify the discrepancy in wave speeds, we compared the wave speeds for each geologic unit in the seismic velocity model with the corresponding wave speeds from the Thurber *et al*. (2007) seismic tomographic model. We updated the relations between seismic wave speed and depth to improve the fit to the wave speeds and gradients in the Thurber *et al*. (2007) tomography model at depths below several kilometers. We continued to use sonic well log data (Brocher, 2005) as the target at shallower depths where it provides tighter constraints.

Initial changes to the seismic velocity model did indeed reduce the travel times appropriately and significantly reduced the bias. However, several iterations were required to fine tune the velocities in the sedimentary units and to remove a spurious velocity contrast that had been introduced across the San Andreas fault in the La Honda Basin, which was inconsistent with 1989 Loma Prieta travel time observations. In the following paragraphs we summarize the major changes made to the velocity model to produce the updated 08.3.0 version used in this study. We applied these changes prior to simulating the two moderate earthquakes and scenario events discussed in the following sections. The electronic supplement contains the relations between wave speed and depth in version 08.3.0, which supersede the relations given in Brocher (2008).

1. For the upper mantle we decreased the wave speeds by 2.5% to better match the Thurber *et al*. (2007) tomographic model, and we added a small positive gradient based on seismic refraction results.

2. For the mafic lower crust/Great Valley ophiolite we reduced Vp in the upper 18 km by as much as 1 km/s and increased it below 18 km depth to a maximum of about 7.4 km/s.

3. For Franciscan units we reduced Vp at depths of 1–3 km by 1–2%, at depths of 4–10 km by 9%, and we increase Vp below 20 km by about 3%.

4. For granitic rocks above 2 km depth the velocities honor borehole sonic data (Brocher, 2005), which is considered more reliable, whereas below 2 km we honored the gradient observed in the Thurber *et al*. (2007) tomographic model.

5. For Great Valley sequence units below 3 km the velocities honor the Thurber *et al*. (2007) tomographic model.

6. For Tertiary-Cenozoic sedimentary units at depths above 750 m we attempted to honor the Vp relation of Hartzell *et al*. (2006) for the Cupertino basin; otherwise, above 4 km depth the wave speeds honor the sonic well log data (Brocher, 2005), which are considered more reliable than tomography at these depths; below 4 km the wave speeds honor the Thurber *et al*. (2007) tomography model.

7. For sedimentary units in the La Honda Basin, wave speeds were increased 10–20% except at depths greater than 6 km where it remains unchanged,

$$V_p = \begin{cases} 2.50 + 0.625d & \text{for } 0 < d \leq 4\text{km} \\ 5.00 + 0.200(d-4) & \text{for } 4\text{km} < d \leq 6\text{km} \\ 5.40 & \text{for } d > 6\text{km} \end{cases}, \tag{7}$$

where V_p is in km/s and d is depth in km. The sonic log for the Champlin Petroleum borehole indicates a Vp of 3.8 km/s at 1 km, a Vp of 4.2 km/s at 2 km, and a Vp of 4.7 at 3 km (Brocher *et al*., 1997). This borehole sampled a steeply dipping section of Butano sandstone for its entire length, so this sonic log may not be representative of the basin as a whole. Williams *et al*. (1999) interpret a seismic refraction line along the La Honda Basin with the upper three 3 km of the basin modeled with a Vp of 4 km/s. The relations given by equation (7) yield slightly faster wave speeds than those for the Great Valley sequence units to a depth of 4 km. Between 4 and 6 km, the Vp lies between that for the Great Valley sequence units and the new Tertiary-Cenozoic sedimentary unit relation from the Cupertino Basin.

8. For Cenozoic sedimentary rocks near Half Moon Bay, we applied separate relations compared to other older Tertiary deposits in order to prevent very strong amplification that does not fit observations from the Loma Prieta earthquake.

9. We updated the attenuation quality factors, Qp and Qs, to the values given in Brocher (2008).

Testing with Moderate Earthquakes

In order to examine the ability of our long-period ground-motion simulations to reproduce recorded waveforms throughout the San Francisco Bay area for earthquakes on the Hayward fault, we simulated two recent moderate earthquakes: the 31 October 2007 Mw 5.45 Alum Rock and 20 July 2007 Mw 4.18 Oakland events. These events occurred on the Hayward fault and were recorded throughout the area of interest for this study (Fig. 2). The Alum Rock event samples the crust around the southern end of the Hayward Fault, while the Oakland event samples the crust around the northern end of the fault. The ruptures we consider in this study span the region between these events.

These moderate earthquakes are much smaller than our scenario events so that the event rupture processes are much simpler, which allows us to evaluate the seismic velocity model and path propagation effects with relatively little bias due to source processes (e.g. spatial and temporal evolution of slip, rupture speed, and rise time). These events are large enough that some finite-source effects are evident, so we do use simple finite-source models. Furthermore, these events were recorded with a high signal-to-noise ratio and occur more frequently than large events. These simulations complement those done previously by Aagaard *et al*. (2008b) for the 1989 Mw 6.9 Loma Prieta earthquake, which

occurred along the San Andreas fault on the west side of San Francisco Bay and included 3-D source and basin effects. In simulating these two moderate earthquakes we are most interested in evaluating our ability to match arrival times, amplitudes, and dominant features of the waveforms. Consequently, we use only deterministic long-period (T > 1–2 s) simulations and compare against recorded waveforms and do not compare the synthetics against the Next Generation Attenuation (NGA) ground-motion prediction equations, which are limited to peak amplitudes.

The recorded motions for the Mw 5.45 Alum Rock earthquake show evidence of a finite-source process, so we construct a simple finite-source model for this event using the method of Dreger and Kaverina (2000). We compute Green's functions for the three-component displacement waveforms recorded at Berkeley Digital Seismic Network (BDSN) stations, BKS, CMB, PKD, and KCC with the GIL7 velocity model (Dreger and Romanowicz, 1994; Pasyanos *et al*., 1996). This 1-D velocity model is commonly used in earthquake location and moment tensor analyses in the San Francisco Bay area. The Green's functions are convolved with a 0.3 second triangular slip velocity function. Both the observed waveforms and Green's functions are bandpass filtered between 0.01 to 0.3 Hz using a two-pole acausal Butterworth filter. Assuming a rupture velocity of 2.8 km/s (approximately 0.80 Vs) yields a peak slip of 0.17 m, and a 7 km by 4 km (length by width) rupture patch. The slip extends down-dip and to the southeast of the hypocenter (9 km depth), and was located between 9 to 13 km depth. The directivity associated with this rupture model derived from the waveform modeling is consistent with the directivity inferred from the spatial variation in peak horizontal ground accelerations and peak horizontal velocities (Seekins and Boatwright, 2007). This slip patch was projected onto the Hayward-Calaveras fault surface, which results in a close match between the strike and dip of the Berkeley focal mechanism and the strike and dip of the fault surface.

Each modeling group computed the waveforms at 185 stations for this event using the rupture model described earlier and the USGS Bay Area Velocity Model 08.3.0. In general the simulations capture the main features of the observed ground motions and are consistent among modeling groups. Figure 2 shows the two earthquake locations and the stations for which we compare ground-motion time histories. Figure 3 illustrates the variation in shaking across the Santa Clara Valley that is accurately captured by the synthetic waveforms at stations CHR, Q32, H30, and CDOB for T > 2.0 s. The electronic supplement includes plots of the synthetic and observed waveforms low-pass filtered with corner frequencies of 0.25 Hz (T > 4.0 s) and 0.5 Hz (T > 2.0 s) for all 185 stations. For station CHR the observed horizontal velocities exceed the synthetic velocities by about 60%. Because this station sits only about 6.7 km from the epicenter, we attribute this discrepancy to our rupture model that simplifies the slip distribution and rupture propagation. For example, the rupture model may underestimate the amount of up-dip directivity.

The waveforms at station Q32, which sits in the Evergreen basin 10.8 km southwest of the epicenter, exhibit greater complexity than those at station CHR as a result of the complex basin response. The horizontal components are dominated by about 10 seconds of larger amplitude motion (peak velocities exceed 10 mm/s) followed by another 10

seconds of more moderate motion (peak velocities exceed 5 mm/s). The synthetic waveforms reproduce the variation in shaking but fail to capture details in the waveforms at periods near 2.0 s. This discrepancy may be associated with surface waves generated at the basin edge, which are sensitive to the contrast in shear modulus between the Evergreen basin and the adjoining Great Valley sequence. The synthetics closely agree with the observed waveforms at periods of 4.0 s and greater (see the electronic supplement). Moving west across the Santa Clara Valley the seismic waves leave the Evergreen basin and near the western edge of the valley enter the Cupertino basin. At station H30, which sits 25.6 km southwest of the epicenter, Love waves (north-south component) dominate the ground motions with over 20 seconds of significant motion (peak velocities are near 5 mm/s). The synthetics reproduce the onset, amplitude, and duration of the motion; however, the later surface wave arrivals in the synthetics are slightly delayed relative to the observations. The synthetics at periods of 2.0 s and longer match the observations nearly as well as the synthetics at periods of 4.0 seconds and longer. In addition to the mismatch in later surface wave arrivals, the primary discrepancy is that the synthetics contain one additional cycle of relatively large amplitude motion associated with the surface waves compared to the observations.

The southward directivity causes the seismic waves radiated north of the epicenter to arrive over a longer time window. As a result, the geologic structures tends to dominate the character of the shaking with less influence from the source. The southward directivity also yields lower amplitude ground motions north of the epicenter. In this region the synthetics generally reproduce the amplitude and duration of motion at periods of 4.0 s and longer but struggle to reproduce the waveforms at periods approaching 2.0 s. For example, at station CDOB in Livermore, 33.2 km north of the epicenter, reverberations within the Livermore sedimentary basin increases the duration of the shaking. The synthetics exhibit longer period motions than the observations even at periods of 4.0 s and longer, suggesting that the seismic velocity model does not adequately capture the geometry of the basin and/or variation of physical properties in and around the basin. Thus, the waveforms are not as accurate in this region as they are in the Santa Clara Valley.

In simulating the 20 July 2007 Mw 4.18 Oakland event we assess the ability of our simulations to reproduce the ground motions throughout the San Francisco Bay area to a source on the northern portion of the Hayward fault. In order to construct a finite-source model for this event, we employ empirical Green's function deconvolution of the records of a nearby Mw 2.7 event at two borehole stations, CMSB and SM2B. The observed moment-rate function at CMSB has much narrower pulse widths than SM2B, 0.14 s compared to 0.93 s. Based on the moment tensor of the event from the Berkeley Seismological Laboratory, the azimuth to CMSB and SM2B are 322 and 55 degrees, respectively; these stations sit nearly perfectly in the along-strike direction and the fault-perpendicular directions. Assuming a rupture speed of 2.8 km/s we determine the rupture length, l, from the fault-perpendicular directivity relationship,

$$l = \tau_p 2.8 km/s = 2.6 km, \tag{8}$$

where τ_p is the pulse width. Similar to the Alum Rock event, the directivity inferred from waveform modeling is consistent with that inferred from the spatial variation in peak horizontal accelerations and peak horizontal velocities (Seekins and Boatwright, 2007). We choose a rupture width of 0.8 km based on a stress drop of 1.0 MPa, and the vertical strike-slip fault relationship between stress drop, scalar moment, and source dimension. These rupture dimensions yield a slip of 0.09 m with a rake of 168 degrees from the Berkeley Seismological Laboratory moment tensor solution. As in the case of the Alum Rock event, we project this slip patch onto the nonplanar geometry of the Hayward fault surface.

Figure 4 displays the observed and synthetic velocity waveforms at four sites (2190, BRK, BRIB, and CTA) for this event. The ground motions at these stations illustrate the agreement between the synthetics and observed motions at locations with different source and wave propagation path characteristics. The waveforms have been low-pass filtered with a corner frequency of 0.5 Hz (T $>$ 2.0 s). The electronic supplement contains plots of the observed and synthetic velocity waveforms for 115 stations low-pass filtered with corner frequencies of 0.5 Hz (T $>$ 2.0 s) and 0.25 Hz (T $>$ 4.0 s). Station BRK lies 9.7 km northwest of the epicenter less than a kilometer west of the Hayward fault and station CMSB (which we used to construct the source model). At station BRK the synthetics reproduce the simple velocity pulse present in the observed waveforms. Although this site displays the best match between the synthetics and observed waveforms, the synthetics at several other sites north of the epicenter also provide a good fit to the observed amplitude and duration of shaking, especially at periods of 4.0 s and longer.

Station 2190 sits 5.8 km south of the epicenter less than 2 km from the edge of San Francisco Bay. The synthetics capture the relative amplitude with the greatest motion associated with the shear-wave arrival but under-predict the amplitude and complexity, especially in the east-west component. For periods greater than 2.0 s, the observed peak velocity for the north-south component exceeds 1 mm/s whereas the peak velocity for the synthetics are all about 0.5 mm/s. At longer periods (T $>$ 4.0 s) the discrepancy in amplitude between the observed and synthetic waveforms becomes smaller. We attribute this discrepancy to insufficient amplification in the simulations resulting from a combination of the minimum shear wave speed imposed in the simulations (which artificially stiffens the soft, near surface sediments) and complexity in the geologic structure not included in the seismic velocity model. For example, this region south of the epicenter between the San Francisco Bay and the Hayward fault may include locally softer or deeper alluvial sediments than regions north of the epicenter, where the synthetics closely follow the observed motions. The consistency among the modeling groups, however, remains excellent considering the variations in amplitude associated with different minimum shear wave speeds.

Shifting our focus to locations east of the Hayward fault, we find greater complexity in the observed waveforms, especially at shorter periods (T $>$ 2.0 s). The simulations have difficulty reproducing this greater complexity; for example, at station BRIB (12.4 km northeast of the epicenter) the observed waveforms include a sharp initial arrival

on the east-west component followed by an additional 15 s of shaking. The synthetics also include a sharp arrival on the east-west component but the arrival is more than a second later than the observed arrival. The synthetics display a similar overall duration of motion but do not replicate the details in the observed waveforms. Furthermore, we find slightly less consistency among the modeling groups but this is mainly confined to the vertical component. The greater complexity in the observed waveforms and delayed arrival of the shear wave in the synthetics suggests that the average shear wave speed east of the Hayward fault may be too slow in the seismic velocity model and the geologic structure may be significantly more complex than what is described by the seismic velocity model.

Further northeast at station CTA, 28.2 km from the epicenter, surface waves dominate the waveforms. The synthetics are able to replicate the amplitude and approximate duration of the surface waves but do a poor job of matching the details of the waveforms. In contrast to station BRIB, the arrival time of the shear wave in the synthetics for station CTA match the observed arrival time.

Accuracy of the Seismic Velocity Model

Examination of the waveforms across the region for these two moderate earthquakes suggests that the seismic velocity model has the greatest accuracy in the Santa Clara Valley; in this region the synthetics match detailed features of the observed waveforms, such as phase arrival times, duration, and waveform shape. In many other areas the synthetics are only able to closely match the initial phase arrival and the overall envelope of the waveform. Between the San Francisco Bay and the Hayward fault near Oakland, the simulations fail to capture amplification at periods close to 2.0 s. Examination of the near-surface physical properties in the seismic velocity model in this area indicates that the minimum shear wave speed imposed in the simulations does not explain adequately this discrepancy, but rather the thickness of the unconsolidated Quaternary deposits in the seismic velocity model may need adjustment. Frankel and Carver (2009) noted similar deficiencies in the seismic velocity model in the region further south between the San Francisco Bay and the Hayward fault using 3-D simulations of the ground motions for the 6 September 2008 Mw 4.0 Alamo earthquake. Thus, ground-motion simulations may under-predict the amplitude of the shaking in this region.

East of the Hayward fault our simulations are only able to reproduce the amplitude and duration of the shaking; the seismic velocity model lacks sufficient detail to reproduce detailed features of the waveforms. The geologic structure east of the Hayward fault has yielded a more complex volume of Cenozoic and Mesozoic rocks compared to the volume dominated by Mesozoic rocks to the west of the fault (Graymer, 2000), so it is not surprising that the seismic velocity model needs to incorporate greater detail in this region. Hence, simulated ground motions from this region east of the Hayward fault are less accurate and are limited to an estimate of the amplitude and duration of shaking. This means they are less suitable for use as inputs in analyses where the details of the waveforms may be

important. Ongoing efforts to refine the seismic velocity model should focus on this region east of the Hayward fault, and validation should continue using other moderate earthquakes and future large earthquakes throughout the San Francisco Bay region.

In summary, these comparisons show that the USGS Bay Area Velocity Model version 08.3.0 reproduces important 3-D wave propagation features of the observed ground motions throughout the San Francisco Bay region at periods down to 2–4 seconds for two events along the Hayward fault. Rodgers *et al*. (2008) drew similar conclusions using version 05.1.0 of the model but noted a persistent bias in the wavespeeds as discussed earlier. Kim *et al*. (2010) demonstrated that version 08.3.0 reduces the average bias in arrival times compared with version 05.1.0 while maintaining a good fit to the peak horizontal velocities over five orders of magnitude for moderate earthquakes. Furthermore, the consistency in ground motions among the five modeling groups using different numerical methods and implementations implies that we can use the results from any of the modeling groups to characterize the ground shaking in our large scenario events. The differences in ground motion associated with imposing slightly different minimum shear-wave speeds and including or excluding topography and attenuation are relatively small compared to the agreement in the amplitude, duration, and shape of the waveforms.

Scenario Earthquakes

Table 2 summarizes the 39 events in our suite of earthquake scenarios and Figure 5 shows the rupture lengths and epicenters. Aagaard *et al*. (2010) discuss each of the earthquake source parameters and the rationale for the choice of variation in detail. In this section we discuss the general trends in the ground motions and the sensitivity in the shaking to variation of the earthquake source parameters for the long-period ($T > 1$–2 s) simulations. The following section discusses the broadband ($T > 0.1$ s) simulations in the context of the 1868 earthquake and the Next Generation Attenuation (NGA) ground-motion prediction equations.

Base Cases

With the modeling groups examining a different subset of the suite of scenario earthquakes, we first demonstrate the consistency of the shaking intensity and velocity waveforms among the modeling groups for one of the scenarios. This extends the consistency we found for the Mw 5.45 Alum Rock and Mw 4.18 Oakland earthquakes to our larger scenarios that have more complex rupture models. Figure 6 shows maps of the Modified Mercalli Intensity (MMI) for scenario HS G01 HypoH from the Graves, Larsen, Ma, and Rodgers modeling groups and residuals with respect to Aagaard's MMI values; a map of MMI for Aagaard's simulation is shown in Figure 8.

We compute the MMI values from our simulations using relationships between PGV, PGA, and MMI developed for ShakeMap (Wald *et al*., 2005). We use this relationship for consistency with the ShakeMap generated for the 1868 earthquake by Boatwright and Bundock (2008). Refining this relationship with improved accuracy for large motions at long periods (T > 2 s) is an area of active research (Cua *et al*., 2010). For the broadband simulations,

$$MMI = \begin{cases} MMI_{PGA} & \text{if } MMI < \text{V} \\ \frac{1}{2}((\text{VII} - MMI_{PGA})MMI_{PGA} + (MMI_{PGA} - \text{V})MMI_{PGV}) & \text{if V} \leq MMI < \text{VII} \\ MMI_{PGV} & \text{if } MMI \geq \text{VII} \end{cases} \tag{9}$$

$$MMI_{PGA} = \begin{cases} 2.20\log(PGA) + 1.00 & \text{if } MMI < \text{V} \\ 3.66\log(PGA) - 1.66 & \text{if } MMI \geq \text{V} \end{cases} \tag{10}$$

$$MMI_{PGV} = \begin{cases} 2.10\log(PGV) + 3.40 & \text{if } MMI < \text{V} \\ 3.47\log(PGV) + 2.35 & \text{if } MMI \geq \text{V} \end{cases} \tag{11}$$

where peak ground acceleration is in g's and peak ground velocity is in cm/s. For the long-period simulations, we only use the PGV to MMI relation (equation (11)), because the simulations have artificially low PGA values due to the absence of short-period energy. In fact, because the intensities are above V at most locations, the intensities are relatively insensitive to the level of PGA. For this comparison among the modeling groups, we use the bandwidth of the deterministic long-period simulations (e.g., T > 1.0 s for Graves's broadband simulations). The permits evaluating the relative importance of including energy down to periods of 1.0 s, while simultaneously assessing the consistency among the modeling groups.

The amplitude and spatial variation of the shaking intensities are very similar among the groups with mean residuals less than 0.20 MMI units. The standard deviations in the residuals for Graves's and Larsen's simulations are about 0.50 MMI units because both of these simulations include periods down to 1.0 s compared to Aagaard's simulations which include periods down to only 2.0 s. The standard deviations in the residuals for Ma's and Rodgers's simulations are smaller with values of about 0.30 MMI units, because they use the same minimum period of 2.0 s as Aagaard's simulations. The largest discrepancies among the modeling groups arises in the Great Valley east of the San Francisco Bay. The longer propagation distances for this region coupled with greater attenuation results in lower amplitudes of shaking for the Larsen and Graves modeling groups which include intrinsic attenuation. Similar levels of agreement are obtained for the other scenarios, and the electronic supplement contains plots comparing the shaking intensities among the modeling groups for bilateral rupture of the Hayward South + North rupture length.

Velocity waveforms at sites throughout the San Francisco Bay area (plots for three sites are shown in Figure 7 with plots for 80 sites available in the electronic supplement) illustrate that, in addition to agreeing in amplitude, the modeling groups generate waveforms with the same features. The first arrivals are nearly identical. We find good

agreement in the amplitude and duration of most later arrivals, but inclusion/exclusion of attenuation and topography and different minimum shear wave speeds leads to small discrepancies in the arrival times for the surface waves. Larsen's waveforms include large secondary arrivals at some locations, which appears to be related to simulating ruptures with significant energy at 1.0 s while including fine-scale topography. In other words, the finite-difference grid is not quite fine enough to accurately resolve the interaction between topography and the seismic waves with periods near 1.0 s. This issue did not arise for ruptures radiating energy primarily at longer periods associated with Mw 7.8 earthquakes on the northern San Andreas fault (Aagaard *et al*., 2008a).

The close agreement in the amplitude, duration, and features of the waveforms across the modeling groups means that we can use scenarios HS G01 HypoH and HS+HN G04 HypoO to tie the results of the different modeling groups together. We use different groups to characterize the sensitivity of the ground motions to different source parameters, with Aagaard's simulations for rupture length and slip distribution, Graves's simulations for rupture length and hypocenter at broadband frequencies, Larsen's simulations for rise time, and Ma's simulations for rupture speed. While the results of each modeling group provide independent characterization of the sensitivity of the ground motions to a single parameter or a small subset of the parameters, we rely on the consistency among the modeling groups to establish the relative sensitivity of the ground motions to variation of the rupture length, slip distribution, hypocenter, rise time, and rupture speed.

Rupture Length, Slip Distribution, and Hypocenter

Aagaard's ($T > 2$ s) simulations include 25 earthquake scenarios that provide a comprehensive view of the ground motions for the five different rupture lengths with one to three hypocenters per rupture length and two to three slip distributions per hypocenter. The electronic supplement for Part I includes plots of the slip distribution and rupture time in each scenario. The rupture length (which correlates with magnitude) exerts the greatest influence on the amplitude of shaking, with longer rupture lengths (larger magnitude earthquakes) generating stronger shaking as evident in Figures 8 and 9. Scenario HS G01 HypoH causes shaking greater than or equal to MMI VII over about 24% of the San Francisco Bay urban area. MMI VII corresponds to the approximate shaking intensity when modern structures begin to suffer damage (Wald *et al*., 2005). The fraction of the urban area experiencing MMI VII increases to 33% in scenario CC+HS G03 HypoH, 58% in scenario HS+HN G04 HypoO, and 60% in scenario HS+HN+RC G06 HypoSPB. We attribute these high levels of shaking experienced by such large fractions of the urban area to the Hayward fault running directly through the urban corridor along the eastern edge of the San Francisco Bay.

The slip distribution has less influence on the overall distribution of shaking, but changes in location of large slip patches (see the electronic supplement of Part I for plots of the slip distributions) affect the shaking close to the

rupture. The features in the maps of MMI in Figure 8 closely resemble each other for corresponding rupture lengths and hypocenters with different slip distributions (one uses a background slip distribution with a vertical gradient in slip to account for creep paired with one stochastic distribution and the other uses a background slip distribution with the slip-predictable approach for accounting for creep paired with another stochastic distribution). These same observations hold for the other hypocenters for the Hayward South, Hayward South + North, and Central Calaveras + Hayward South rupture lengths and changing the random seed in the stochastic slip distribution with the same vertical gradient in slip for the Hayward South rupture length (see the electronic supplement).

For the Hayward South, Hayward South + North, and Central Calaveras + Hayward South rupture lengths, we consider three hypocenter locations. This yields cases with north-to-south rupture, bilateral rupture, and south-to-north rupture. As indicated in Table 2 the various rupture lengths use different slip distributions; this means the locations of large and small slip differ. As shown in Figure 10 rupture directivity along the strike of the fault causes the ground motions to be much smaller in the San Jose area for south-to-north rupture compared with north-to-south or bilateral rupture. For example, the peak horizontal velocity at site CT06085501400 in San Jose (location is shown in Figure 5) is 0.13 m/s in scenario HS G01 HypoF with south-to-north rupture compared with 0.31 m/s in scenario HS G01 HypoH with bilateral rupture. The difference is even more extreme for the Hayward South + North rupture; south-to-north rupture results in a peak velocity of only 0.05 m/s compared with 0.37 m/s for both bilateral and north-to-south rupture. Likewise, the ground motions around San Pablo Bay are much smaller for north-to-south rupture compared with bilateral or south-to-north rupture. These trends are consistent with previous studies of rupture directivity (Somerville *et al*., 1997; Aagaard *et al*., 2001; Spudich and Chiou, 2008). In our discussion of Graves's broadband ground motions in a later section, we will examine the spatial variation in spectral acceleration for the different hypocenters in the context of the Spudich and Chiou (2008) directivity corrections to the NGA ground-motion prediction equations.

Graves's broadband velocity waveforms (Figure 11) further illustrate these trends in rupture directivity. In San Francisco the ground motions are largest for south-to-north rupture (Fremont epicenter) for both the Hayward South and Hayward South + North rupture lengths with peak horizontal velocities of 0.14 m/s and 0.20 m/s, respectively. These peak velocities are about 50% larger than those for north-to-south rupture and bilateral rupture. This is consistent with larger ground motions for ruptures propagating towards the city. The waveforms in Livermore tend to be largest for north-to-south rupture, because Livermore lies north of the more rigid rock underneath the hills east of San Jose. This more rigid material tends to trap energy in the Livermore basin in north-to-south ruptures and shield Livermore from energy radiated in south-to-north ruptures. The waveforms in Livermore are also sensitive to the slip distribution. For the Hayward South + North rupture length and Fremont epicenter, the velocities are less than about 0.2 m/s with a duration of only about 15 s, whereas the amplitudes reach 0.8 m/s with 50 s of significant shaking for the San Pablo Bay epicenter; yet, the ground motion amplitudes and duration of shaking for the three epicenters and the Hayward

South rupture length are quite consistent, with amplitudes of about 0.15 m/s. We attribute these different sensitivities to the hypocenter to the different stochastic portions of the slip distribution in the two sets of scenarios. For the Hayward South + North rupture length, there are no large slip patches south of Livermore, so rupture starting in Fremont does not radiate significant energy until it is further north. In the case of the Fremont epicenter for the Hayward South rupture length, there is a large slip patch at the southern end of the rupture, so northward propagating ruptures radiate energy into the Livermore area.

Some features in the distributions of shaking persist as we vary the rupture length, slip distribution, and hypocenter. These features are related to geologic structure as opposed to source features. This includes higher intensity shaking extending 20–40 km east of the Hayward fault due to deeper soft material east of the fault compared to west of the fault. We also find higher intensity shaking in the sedimentary basins, such as the Livermore basin, the San Pablo basin under San Pablo Bay, the Evergreen basin east of San Jose, the Cupertino basin west of San Jose, and the San Leandro basin west of Hayward. The shaking intensities in the Evergreen and Cupertino basins reach values 1–2 MMI units higher than locations several kilometers outside the basins. Similarly, the river valleys north of San Francisco Bay (e.g., Napa River valley running northwest from Napa) tend to have intensities 1–2 MMI units higher than the surrounding areas.

Larsen *et al*. (2000) also found amplification of ground motions in the San Pablo, Evergreen, and Livermore basins for magnitude 7.0 Hayward fault scenario earthquakes using a very simple 3-D seismic velocity model. Using seismic velocity models defined nearly identical to the USGS Bay Area Velocity Model 08.3.0, Harmsen *et al*. (2008) observed persistent patterns of shaking very similar to those in this study for scenario earthquakes involving the Hayward and Calaveras faults. The ruptures excite surface waves that are amplified in the Livermore, Evergreen, and Cupertino basins. Furthermore, Harmsen *et al*. found high intensities extending south along the east side of the Santa Clara Valley from the Evergreen basin as we do in this study.

Rise Time and Rupture Speed

[ROB- PLEASE SUGGEST REVISIONS TO RESPOND TO REVIEW'S COMMENT. "Less sensitivity of rise time and rupture speed is one of the interesting conclusions in the article. From Part I, the rise time and rupture speed of the earthquake scenarios seem to include realistic complexity. Please add discussion why the Hayward simulations provide less sensitivity as Aagaard et al. (2001), not as Graves et al. (2008)."]

Larsen's simulation of eight scenarios with four different rise times for Hayward South and Hayward South + North bilateral ruptures characterize the sensitivity of the ground motions to the rise time in the slip time history (duration of slip at a point). For each rupture length, we consider three different scaling factors of 1.0, 1.5, and 2.0 in

the expression for the rise time as a function of slip,

$$\frac{t_{95}}{t_0} = C\sqrt{\frac{D_f}{D_0}}, \tag{12}$$

where t_{95} denotes the time for 95% of the slip to occur, D_f denotes the final slip, t_0 = 1.0 s, D_0 = 1.0 m, and C takes on values of 1.0, 1.5, or 2.0 (denoted by Tr10, Tr15, and Tr20 in the scenario labels). This provides a factor of two difference in rise times across the scenarios with the median rise time in each scenario similar to the value proposed by Somerville *et al.* (1999) for self-similar rupture. For example, with C equal to 1.5, a slip of 1.0 m yields a rise time of 1.5 s (Mw 6.7 for Somerville *et al.* (1999)) and a slip of 1.5 m yields a rise time of 1.8 s (Mw 7.2). We also consider uniform rise times, $t_{95} = 1.0s$ for the Hayward South rupture length (denoted by Tr10u in the scenario name) and $t_{95} = 2.0s$ for the Hayward South + North rupture length (denoted by Tr20u in the scenario name). Even though Larsen's simulations include periods down to 1.0 s, the limited bandwidth likely inhibits their ability to completely resolve differences in the ground motions for these rise times.

The ground motions exhibit very little sensitivity to the rise time. Figure 12 shows that varying the rise time without any corresponding changes in any of the other source parameters has no effect on the shape of the waveforms. Nevertheless, the velocity amplitudes can vary up to about 50% for variation in rise times by a factor of two. These variations are much less dramatic than the changes we observed for the variations in rupture length and hypocenter. The electronic supplement contains waveforms at 80 sites and maps of the shaking intensity which demonstrate that all of the sites display similarly weak sensitivities to the rise time. Aagaard *et al.* (2001) arrived at the same conclusion through variation of the peak slip rate in simpler rupture models in a model with 1-D structure.

We characterize the sensitivity of the ground motions to the rupture speed using Ma's six simulations with three rupture speeds for Hayward South and Hayward South + North bilateral earthquake ruptures. The scenarios include local rupture speeds in high slip regions at 82% of the local shear wave speed (denoted by Vr82 in the scenario name), 92% of the local shear wave speed (denoted by Vr92 in the scenario name), and supershear rupture (denoted by Vr141 in the scenario name). Part I (Aagaard *et al.*, 2010) discusses the details of the local rupture speed variation. The two subshear cases (Vr82 and Vr92) encompass the range of rupture speeds for many crustal strike-slip events. The supershear case includes locally supershear rupture where the slip exceeds the average slip with a maximum rupture speed of $\sqrt{2}$ times the local shear-wave speed at the location with the maximum slip. Most observations of supershear rupture involve large strike-slip rupture of nearly planar faults (Bouchon and Karabulut, 2008; Bouchon and Karabulut, 2009). Thus, the relatively short length of the Hayward fault, slightly complex geometry (e.g., variations in strike and dip along its length) as well as the presence of creep (i.e., stable sliding regions) suggest supershear rupture on the Hayward fault is unlikely. Thus, the scenarios with subshear rupture have substantially higher probabilities.

The ground motions exhibit a weak sensitivity to the variation in rupture speed. The amplitude of the velocity waveforms display roughly the same variation across the range in rupture speeds as they do for the range of rise times considered earlier. However, ruptures with faster rupture speeds radiate energy in a shorter time period, which results in sharper arrivals and shorter duration velocity pulses. This gives rise to some small changes in the shape of the waveforms as evident in Figure 13 for bilateral Hayward South + North ruptures. The waveforms in San Francisco and Livermore, which lie well off the strike of the Hayward fault display less variation in shape than those in San Jose, which lies close to the southern end of the rupture and is more sensitive to the rupture duration. The waveforms in San Francisco and Livermore have only subtle shifts in the duration of the velocity pulses with differences in peak velocity of less than 15%. On the other hand, in San Jose the different rupture speeds give rise to variations in the envelope of the waveform with fluctuations in amplitude of about 50–100%. Most other sites exhibit sensitivities to variations in rupture speed at more moderate levels between these examples. At sites very close to the rupture, we do not find evidence for rotation of the peak motion from fault-perpendicular to a more fault-parallel orientation (see velocity waveforms in the electronic supplement) as predicted in theoretical models of supershear rupture (Dunham and Archuleta, 2004; Aagaard and Heaton, 2004). This is likely due to the few relatively short bursts (about 15 km long) of supershear rupture in our rupture models and complexity of the velocity waveforms associated with the 3-D geologic structure.

Creep and Coseismic Slip

As discussed in Part I (Aagaard *et al*., 2010), in places the Hayward fault accommodates part of its long-term slip via aseismic creep. Creep generally occurs at shallow depths (from the ground surface down to about 3–5 km depth), but Funning *et al*. (2007) image a deep creeping region beneath Berkeley. Most of the earthquake scenarios use a vertical gradient in slip in creeping regions to account for how creep may affect the coseismic slip distribution. The vertical gradient decreases the slip in creeping regions as the rupture propagates into shallower regions. We chose the vertical gradient of -0.12 m/km for consistency with the paleoseismic record and the reduced area factor developed by the WGCEP (2003). Although we expect creep, which accommodates some of the long-term fault slip-rate, to exert some influence on the coseismic slip distribution, its effect could be minimal in large earthquakes. At the other end of the spectrum, perhaps very little or no coseismic slip occurs in the creeping regions. Neglecting the influence of creep corresponds to a vertical gradient in slip of zero, whereas preventing coseismic slip in creeping regions corresponds to an infinite vertical gradient in slip. As the vertical gradient in slip increases, slip in the creeping regions decreases, which reduces the average slip and earthquake magnitude. We consider both of these end-member cases for bilateral rupture of the Hayward South and Hayward South + North rupture lengths.

For the Hayward South + North rupture length, the moment magnitude of the scenario without coseismic slip in creeping regions (fully creeping) is 6.82, the moment magnitude of the scenario with a gradient of -0.12 m/km is 7.05, and the moment magnitude of the scenario neglecting creep is 7.12. This variation in the magnitudes of the scenarios as we vary the vertical slip gradient arises from maintaining consistency with the magnitude-area relation. Figure 14 displays maps of the MMI for these three scenarios and Figure 15 shows the velocity waveforms at three sites. The shaking intensity and velocity amplitudes follow the variation in magnitude. The values for the Mw 6.82 scenario are similar to those for the bilateral Mw 6.76 Hayward South scenario, and the values for the Mw 7.12 scenario are slightly higher than those for the Mw 7.05 scenario. Because we use the same random seed in the stochastic portion of the slip distribution, the differences are limited to the amount of slip and the relative distribution between the creeping and locked portions. In the fully-creeping scenario, very little slip occurs near the surface. Consequently, the rupture generates smaller amplitude surface waves, so the velocities in Livermore are about one-third to one-half of those in the scenarios in which creep exhibits less influence on coseismic slip. Similarly, the velocities are about 50% smaller in San Jose for the fully-creeping scenario. The corresponding ground motions for the Hayward South rupture length display similar trends.

The simulations suggest that the ground motions are only moderately sensitive to the presence of the creeping regions if creep has a moderate to minimal impact on the coseismic slip distribution. This would likely be the case in regions with only very shallow creep or regions where the creep rate is a small fraction of the long-term fault slip rate. On the other hand, if creeping regions have little or no coseismic slip with rise times comparable to locked regions, the expected magnitudes of Hayward fault events are about 0.1-0.2 units smaller with a corresponding decrease in the intensity of the shaking with even smaller excitation of surface waves.

Broadband Simulations

Graves extended his simulations of the six Hayward South and Hayward South + North scenarios to shorter periods using the hybrid procedure described in Graves and Pitarka (2004). This simulation technique combines a stochastic approach at short periods (0.1 s $<$ T $<$ 1 s) with the 3-D deterministic approach described earlier at long periods (T $>$ 1 s) to produce broadband ground-motion synthetics. The procedure has been validated using the 1989 Mw 6.9 Loma Prieta earthquake (Aagaard *et al*., 2008b) [ROB- ADD STUFF HERE]. We also employed this methodology to calibrate the wavenumber at which we cross-over from the nominal, background slip distribution to the stochastic slip distribution in Part I (Aagaard *et al*., 2010).

In the short-period simulations we sum the response for each subfault assuming a random phase, an omega-squared source spectrum, and simplified Green's functions calculated for a specified 1-D velocity structure. This

approach follows from Boore (1983) with the extension to finite faults given by Frankel (1995) and Hartzell *et al.* (1999). Each subfault ruptures with a moment proportional to the final slip of the subfault given by the original source model, and the values are scaled uniformly so that the moment matches that of the original source model.

As discussed in the previous section, the creeping portion of the fault requires special attention when developing the kinematic rupture model. The simulation of high frequency motions using the semi-stochastic approach of Graves and Pitarka (2004) also must account for this effect. In determining the effective area and magnitude of the rupture, we use the area reduction factor (R) developed by the WGCEP (2003). In the semi-stochastic simulation the moment release of each subfault scales with the high frequency stress parameter, σ_p (Boore, 1983). Following self-similarity the moment also scales as Area$^{3/2}$, or R$^{3/2}$. Thus, in order to properly account for the creeping portions of these ruptures, the stress parameter must also be scaled by R$^{3/2}$. Our default value for the stress parameter is 50 bars. For the Hayward South ruptures, R=0.79, which yields a stress parameter for these ruptures of 35 bars; for the Hayward South+North ruptures, R=0.86, which yields a stress parameter for these ruptures of 40 bars.

The formulation requires specification of a 1-D layered velocity model in calculating simplified Green's functions and impedance effects. In this study we create a 1-D velocity model that roughly follows the average depth variations in the 3-D structure, and we include both direct and Moho-reflected rays, which are attenuated by 1/Rp, where Rp is the total path length traveled by the particular ray. For each ray we compute a radiation pattern coefficient by averaging over a range of slip mechanisms and takeoff angles. Anelasticity is incorporated via a travel-time weighted average of the Q values for each of the material layers and a generic rock site spectral decay operator, κ=0.04 (Anderson and Hough, 1984). Finally, gross impedance effects are included using quarter wavelength theory (Boore and Joyner, 1997) to derive amplification functions that are consistent with the specified 1-D velocity structure.

To account for site-specific geology in the broadband motions, we apply frequency-dependent, non-linear amplification factors based on Vs30, the travel-time-weighted shear speed in the upper 30 m at the site. The site-specific Vs30 values were taken from the map of Wills *et al.* (2000). The form of the amplification factors were developed using equivalent linear site response analysis (Walling *et al.*, 2008) as implemented in the NGA ground-motion prediction equations of Campbell and Bozorgnia (2008).

Comparison with the 1868 Earthquake

Although we are not attempting to simulate the 1868 Hayward fault earthquake in detail (because little is known about its source parameters), several of the scenarios are designed to have source parameters that might be similar to this event. The Hayward South scenarios are consistent with the rupture length (Yu and Segall, 1996; Bakun,

1999) and magnitude (Bakun, 1999) of the 1868 earthquake. Boatwright and Bundock (2008) suggest that the north-south symmetry of the intensities is consistent with bilateral rupture compared with either predominantly north-to-south or south-to-north rupture. Our selection of three hypocenters permits further analysis to identify which rupture propagation pattern is most consistent with the shaking intensities from the 1868 event.

Figure 16 compares Modified Mercalli Intensity from Graves's broadband (T $>$ 0.1 s) simulations of three Mw 6.76 Hayward South ruptures (HS G01 HypoO, HS G01 HypoH, and HS G01 HypoF) with the intensities of the 1868 earthquake compiled by Boatwright and Bundock (2008). The limited number of intensity observations (125) and unknown slip distribution for the 1868 earthquake limit the level of agreement, but the simulation with bilateral rupture (Hayward epicenter) produces intensities most consistent with those from the 1868 earthquake. However, all three Mw 6.76 scenarios fit the 1868 intensities relative to the uncertainty in the slip distribution and our expectations based on our previous efforts to match MMI values for the Loma Prieta earthquake (Aagaard *et al.*, 2008b). The Mw 7.05 scenario earthquakes with the Hayward South + North rupture length (shown in the electronic supplement) exhibit significantly less consistency with the observed intensities from the 1868 earthquake. Thus, the simulations support previous studies (Bakun, 1999) that assign a magnitude of about 6.8 to the 1868 earthquake.

Comparison with NGA Models

Comparison of the broadband ground motions with ground-motion prediction equations, such as the NGA relations (Abrahamson and Silva, 2008; Boore and Aktinson, 2008; Campbell and Bozorgnia, 2008; Chiou and Youngs, 2008), provides an additional perspective from which to assess the ground motions for our scenario events. We will use AS08, BA08, CB08, CY08 to refer to these four NGA relations, respectively. In calibrating the earthquake source parameters via comparison of broadband synthetics from a 1-D velocity model with the NGA relations, we focused on minimizing the mean residual, not the variance or spatial variation. The broadband synthetics for the six scenarios that incorporate variability in the hypocenter (rupture directivity) and magnitude, permit a much more detailed comparison, including examination of effects due to basin response, local site conditions, and rupture directivity.

Figure 17 compares spectral accelerations (SA) at a period of 1.0 s from Graves's broadband simulation of the Mw 6.76 Hayward South bilateral rupture (scenario HS G01 HypoH) with those predicted by the AS08, BA08 and CB08 NGA relations. The mean residuals correspond to event terms in the ground-motion prediction models and express how the average ground motions from the 3-D simulations differ from the median of the ground-motion prediction model for the specified earthquake magnitude.

The mean residual for each of the three NGA relations for this bilateral Hayward South rupture is small with the peak in the histogram within about 0.2 $\log_2$ units (15%) of zero. The maps of the residuals clearly show that the 3-D

ground-motion simulations predict stronger shaking off the ends of the rupture than the NGA ground-motion prediction equations. The 3-D ground-motion simulations include strong along-strike directivity which is not explicitly included in the NGA relations. The NGA relations incorporate the distance from the rupture, so that the spectral values average the directivity effects along the fault strike. In the next section we examine this issue in more detail using Graves's broadband simulation of three Hayward South + North ruptures.

We examine the spatial variation in the residuals of the spectral acceleration with period for the BA08 NGA relation using the Graves's Hayward South + North ruptures (Figure 18). The electronic supplement contains similar plots for peak horizontal ground acceleration (PGA), peak horizontal ground velocity (PGV), and spectral acceleration at periods of 0.3 s, 1.0 s, and 3.0 s for each of Graves's broadband simulations and the AS08, BA08, and CB08 NGA ground-motion prediction equations.

At shorter periods (0.3 s) the mean bias is 0.43 $\log_2$ units (34%) with most of the positive residual values in the region east of the Hayward fault. The variance is relative small (0.44 $\log_2$ units or 36%). The mean residual is smaller at 1.0 s (0.27 $\log_2$ units or 21%) but increases at 3.0 s (0.81 $\log_2$ units or 75%). The variance increases with period and is 0.71 $\log_2$ units or 64% at 1.0 s and 1.06 $\log_2$ units or 110% at 3.0 s. At longer periods the largest residuals occur east of the Hayward fault, in the river valleys near Santa Rosa and Napa, and in the Santa Clara Valley around San Jose. A similar increase in residuals with period was seen in the analysis of the Mw 7.8 San Andreas ShakeOut simulations for Southern California (Graves *et al.*, 2008). In that study, as in the current study, the large variances at the longer periods are primarily due to the effects of rupture directivity and amplification within relatively low shear wave velocity material, such as sedimentary basins. These are robust features of the 3-D long-period deterministic ground-motion simulations that we associate with the 3-D geologic structure and source characteristics. The NGA models incorporate such effects via very simple approximations as we discuss in the following two sections.

We summarize the consistency of the simulations with the AS08, BA08, and CB08 NGA relations in Figure 19 by computing the median residual and its variance averaged over the three NGA relations for Graves's six broadband simulations (scenarios HS G01 HypoO, HS G01 HypoH, HS G01 HypoF, HS+HN G04 HypoSPB, HS+HN G04 HypoO, and HS+HN G04 HypoF). In general, the simulated motions fall about one standard deviation above the median value, suggesting that, on average, the simulations are within the expected range of event-to-event variability observed in recorded earthquakes of the same magnitude.

The average median residuals for the three Mw 7.05 Hayward South + North scenarios tend to be slightly larger than those for the three Mw 6.76 Hayward South scenarios. This may indicate that the ruptures associated with the G01 and G04 slip distributions radiate slightly more coherent energy than real earthquakes. Without similar analysis for broadband simulations of the rest of the suite of scenarios, we hesitate to conclude that this bias extends to the entire

suite of scenarios. The smallest average median residuals generally occur for the southernmost epicenter (Fremont) for both the Mw 6.76 and Mw 7.05 scenarios. We suspect this results from trade-offs between the assumed hypocenters, the kinematic slip distribution, and the interaction of the seismic waves with the 3-D geologic structure. Drawing any broad conclusions about the variations in the average median residuals would require applying the broadband simulation methodology to the entire suite of scenarios which incorporates greater variability in the rupture parameters. Furthermore, it is difficult to assess how one might adjust the NGA models to account for the effects of creep on coseismic slip beyond the effect on the magnitude for a given rupture area; creep also affects secondary features, such as the along-strike and down-dip distribution of slip.

Accounting for Directivity

As discussed earlier, at the longer periods the simulated motions generally exceed the empirical ground-motion relations in regions with strong forward directivity and fall slightly below the empirical relations in regions with backward directivity; consequently, the PGV and spectral acceleration at 1.0 s and 3.0 s at most sites are highly sensitive to the hypocenter. Figure 18 clearly illustrates this effect by comparing the Mw 7.05 bilateral Hayward South + North rupture with the BA08 NGA relation for spectral acceleration at 1.0 s. While the overall mean of the residuals for these cases is in the range of 10% to 20%, sites located in the forward rupture direction have simulated motions up to 2–3 times larger than the empirical relation, whereas sites in the backward rupture direction can have motions 2–3 times smaller than the empirical relation.

Somerville *et al*. (1997) was the first to develop a directivity model that could be applied as a correction to ground-motion prediction equations. Two additional directivity models have been developed in conjunction with the NGA program, Spudich and Chiou (2008) proposed a model based on isochrone theory and Rowshandel (XXXX) proposed a model based on rupture heterogeneity and source-site geometry. The Spudich and Chiou and Rowshandel corrections give similar results, although the Rowshandel model generally predicts stronger directivity effects, particularly for ruptures containing strong slip asperities.

Figure 20 shows the Spudich and Chiou directivity corrections for the three Mw 7.05 Hayward South + North scenarios applied to the BA08 NGA relation for 1.0 s SA. Although some of the locations with higher residuals lie in sedimentary basins, the pattern of these corrections corresponds quite well to the residuals shown in Figure 20, but the absolute level is smaller with the maximum correction not exceeding about 25%. Consequently, applying these corrections to the NGA relation only reduces the standard deviation of the residuals by a few percent. Similar results are found for PGV and 3.0 s SA, as well as for the other NGA relations (see the electronic supplement).

We attribute the differences in the strength of the rupture directivity to several factors, all of which arise from the fact that there are relatively few ground-motion recordings close to large strike-slip earthquake ruptures. We developed our rupture models using information gleaned from source inversions of past earthquakes as well as theoretical and laboratory analyses of rupture dynamics (see Aagaard *et al*. (2010)). We calibrated the models to match, on average, existing ground-motion records. However, the sparsity of data can leave some details of the rupture process rather poorly constrained. For example, it is generally accepted that ruptures tend to propagate at a speed of about 80% to 85% of the local shear-wave speed; however, it is not uncommon for ruptures to propagate slower than this and there are several cases where supershear rupture has been proposed (Olson and Apsel, 1982; Archuleta, 1984; Spudich and Cranswick, 1984; Anderson, 2000; Bouchon *et al*., 2000; Bouchon *et al*., 2001; Sekiguchi and Iwata, 2002; Bouchon and Vallee, 2003; Dunham and Archuleta, 2004; Ellsworth *et al*., 2004; Aagaard and Heaton, 2004). Unfortunately, the existing catalog of ground-motion records fails to provide comprehensive constraints on the nature of this variability.

This lack of data also led Spudich and Chiou to make simplifying assumptions in the development of their directivity model, such as truncating the data (and model) at a distance of 40 km from the rupture. This precluded any period dependence in the directivity pattern; we expect longer period ground motions, e.g., surface waves, to display directivity effects at much greater distances from the source than shorter period ground motions. Additionally, they assumed a fixed value for the rupture speed of 0.80 Vs. A more comprehensive directivity model should consider amplification variations as a function of distance and period. Spudich and Chiou found considerable variability in the amount of directivity in the observed data. For example, records from the 1979 Mw 6.5 Imperial Valley and 1989 Mw 6.9 Loma Prieta earthquakes exhibit a strong positive correlation with the isochrone directivity parameter, but the records from the 1995 Mw 6.9 Kobe earthquake exhibit a weak negative correlation. This suggests that the simulations with the G01 and G04 slip distributions may be consistent with strong directivity observed in some earthquakes, but this limited set of scenarios with two slip distributions and three hypocenters may not capture the variability in directivity observed across a large suite of earthquakes. Verifying whether our entire suite of earthquake scenarios produces the observed range of rupture directivity would require broadband simulations for the entire suite of scenarios and is beyond the scope of this study.

Basin Response

[ROB- PLEASE SUGGEST REVISED TEXT IN RESPONSE TO REVIEWER'S COMMENTS. "In discussion on the basin amplification, please add the effects of Q value and reference period, if possible."]

Within sedimentary basins the simulated PGV and spectral accelerations at 1.0 and 3.0 s consistently exceed the empirical predictions by a factor of up to 2 to 3. This is also true in some regions outside sedimentary basins, such as the area just east of the Hayward fault between Livermore and Concord (see Figure 18 and the electronic supplement),

which is composed of material with low shear-wave speeds compared to the surrounding rock. However, the amplitude of the synthetic ground motions for the Mw 5.45 Alum Rock and Mw 4.18 Oakland earthquakes closely match the observed amplitudes. Other studies (Rodgers *et al*., 2008; Kim *et al*., 2010) also find similar agreement using the USGS Bay Area Velocity Model. As a result, this discrepancy between the simulations and the NGA models may be related to how the NGA models account for basin effects. The NGA models account for basin amplification either through Vs30 alone (BA08) or through a combination of Vs30 and a basin depth term (AS08, CB08, CY08). However, most of the ground-motion data used to constrain these models come from deep basins (e.g., the Los Angeles basin) or theoretical studies within deep basin environments (Day *et al*., 2008). In addition, the models also do not explicitly account for basin-edge effects or the coupling of directivity and basin amplification.

In the development of their ground-motion model, Boore and Aktinson noted the strong correlation between Vs30 and basin depth in the NGA data set and argued that Vs30 can be used as a proxy for basin depth in the empirical regression. While this is true for the NGA data set in general, it may not hold for the greater San Francisco Bay area where the basins are relatively shallow compared to other regions (Figure 21). In this context basin depth is defined as the depth to the 1.5 km/s shear-wave isosurface, hereafter referred to as Z1.5. For the San Francisco Bay area we measured Z1.5 in the 3-D USGS Bay Area Velocity Model 08.3.0 on a grid of sites at 1 km spacing and estimated Vs30 for each site using Wills *et al*. (2000). The broadband simulations also use Vs30 values from Wills *et al*. (2000) in site corrections associated with imposing a minimum shear-wave speed in the simulations. Because Wills *et al*. classify sites into discrete Vs30 bins, we totaled the number of observations within each bin and scaled the symbols in Figure 21 by that number. While the NGA data set as a whole shows a clear and strong increase of Z1.5 with decreasing Vs30, the Bay area sites (both within the NGA data set and those for the 3-D model) exhibit a very weak correlation. This could reflect differences in the tectonic environments between the San Francisco Bay area and the sites in the NGA data set.

We explore the implications of this difference in correlation to determine how well it explains larger amplitude ground motions in the 3-D simulations compared with the NGA ground-motion prediction equations. We derive an approximate amplification correction to the Boore and Aktinson NGA model for our San Francisco Bay sites. For linear site response the BA08 amplification term is given by

$$A_{site} = \left(\frac{Vs30_{site}}{V_0} \right)^x \tag{13}$$

where $Vs30_{site}$ would be the site-specific Vs30 value (from Wills *et al*., for example). For periods longer than about 1 second x is approximately constant and equal to -0.725. From this relation we define an approximate amplification correction to the BA08 NGA relation for our sites as

$$A_{cor} = \frac{A_{pred}}{A_{site}} = \left(\frac{Vs30_{pred}}{Vs30_{site}} \right)^x, \tag{14}$$

where $Vs30_{pred}$ is the Vs30 value predicted by the correlation between Z1.5 and Vs30 noted by Boore and Aktinson. The amplification correction has the effect of replacing the Vs30 values from Wills *et al.* with Vs30 values ($Vs30_{pred}$) predicted by Z1.5 and the correlation between Vs30 and Z1.5 in the NGA data set. We determine the correlation using the following relational form:

$$\log_{10}(Vs30/V_0) = A + B\log_{10}(Z1.5/Z_0), \tag{15}$$

where V_0 = 760 m/s, Z_0 = 1 km, A = -0.375, and B = -0.211.

Figure 21 shows the spatial distribution of A_{cor} for our model region. Comparing this to the residuals for spectral acceleration at 3.0 s for the Mw 7.05 Hayward South + North scenario shown in Figure 18, we see many similarities both in terms of spatial pattern and amplitude (keeping in mind that the residuals in the figures also contain the effects of rupture directivity). The residuals indicate amplification of motions along the eastern side of the Hayward fault, which extends north into the San Pablo basin and south toward Gilroy. The region immediately east of the Hayward fault has relatively high Vs30, but also relatively deep Z1.5; thus, the NGA relations (without the amplification correction) tend to under-predict the simulated motions in this region. Likewise, regions surrounding the margins of the San Francisco Bay and the Sacramento River Delta have relatively low Vs30 but a relatively shallow Z1.5. Consequently, the BA08 NGA relations (and likely the others as well) over-predict the simulated motions in these regions. Other regions where Vs30 and Z1.5 tend to be correlated, such as the Cupertino and Evergreen basins near San Jose and the Great Valley, the NGA relations are similar to the simulated motions. This suggests that refinement of the ground-motion prediction models may be required in order to adequately account for the effects of amplification across the diverse range of tectonic environments, including shallow basins.

Conclusions

These ground-motion simulations demonstrate that large Hayward fault earthquakes generate strong shaking throughout the San Francisco Bay area with about 50% of the urban area experiencing MMI VII or larger for magnitude 7.0 earthquakes. The details of the shaking are strongly dependent on the rupture length (earthquake magnitude), hypocenter (rupture directivity), and slip distribution. The ground motions exhibit a relatively weak sensitivity to variations in the rise time, consistent with results from a previous study using a generic 1-D variation in material properties (Aagaard *et al.*, 2001). The ground motions also display less sensitivity to the rupture speed; we do not find evidence for regions in the San Francisco Bay area with a strong sensitivity to the rupture speed, such as that found in the Los Angeles basin for northwest rupture of the southern San Andreas fault (Graves *et al.*, 2008). Thus, these simulations provide further evidence for significant variability in ground motions associated with earthquake source parameters that are difficult to forecast, such as the rupture extent and hypocenter, while highlighting the ability to

capture the effects of 3-D sedimentary basins, which can be constrained *a priori*; the simulations also emphasize the difficulty in constraining rise times and rupture speed due to the relatively weaker sensitivity of ground motions to these parameters.

The simulations predict ground motions consistent with the Abrahamson and Silva (2008), Boore and Aktinson (2008), and Campbell and Bozorgnia (2008) NGA ground-motion prediction equations with two areas of departure. The 3-D simulations generate stronger rupture directivity than that predicted by the Spudich and Chiou (2008) directivity correction to the NGA relations, although the spatial variation in ground motion in the simulations associated with rupture directivity closely matches the spatial variation in the Spudich and Chiou model. Similar discrepancies exist with respect to individual events used to construct the Spudich and Chiou model, suggesting that the simulations may be realistic and the accuracy of the model could be improved by incorporating a period dependence on the areal extent of directivity effects. Analysis of ground-motion amplification in sedimentary basins from our simulations indicates that amplification in shallow basins (e.g., the Cupertino and Evergreen basins near San Jose, the San Pablo and San Leandro basins near Oakland, and the Cotati and Windsor basins near Santa Rosa) and regions with deep soft material but relatively fast Vs30 values (e.g., the region immediately east of the Hayward fault between Hayward and Richmond) may exceed that predicted by the NGA relations. This appears to arise from the strong correlation between Vs30 and basin depth for the sites recording ground motions used to construct the NGA relations. In these same areas, peak amplitudes from our simulations of two moderate earthquakes agree quite well with the observed amplitudes. Verifying this discrepancy and the greater accuracy of the 3-D simulations requires further testing, especially in areas outside of Southern California with shallow sedimentary basins.

Our ground-motion simulations include a reduction of the coseismic slip in creeping regions through either a slip-predictable approach or a vertical gradient in slip in the creeping regions. Both of these approaches reduce the earthquake magnitude for a given rupture area. Consideration of the end-member cases for the vertical-gradient approach (creep having no affect on coseismic slip and creep preventing any slip in creeping regions) demonstrates that considering creep when computing ground motions for Hayward fault scenario earthquakes reduces the amplitude of the ground motions compared to when creep is neglected. In the extreme case of no coseismic slip in creeping regions, the ground motions in Livermore and San Jose are about 50% smaller as a result of reduced excitation of surfaces waves associated with the limited amount of shallow slip. This highlights the important role of continued and improved characterization of the spatial extent and rates of creep along the Hayward fault for accurate assessment of the seismic hazard associated with the Hayward fault.

Data and Resources

Observed ground motions for the 2007 Mw 5.45 Alum Rock and 2007 Mw 4.18 Oakland earthquakes can be obtained from the IRIS Data Management Center at www.iris.edu (last accessed October 2009) and the USGS National Strong Motion Program at nsmp.wr.usgs.gov (last accessed October 2009). The USGS Bay Area Velocity Model 08.3.0 can be obtained from www.sf06simulation.org (last accessed October 2009). All other data used in this paper came from published sources listed in the references. Many of the figures were generated using Generic Mapping tools (Wessel and Smith, 1998) and the low-pass filtering of the waveforms was performed using SAC2000 (Goldstein *et al*., 2003).

Acknowledgments

In analyzing the ground motions we benefited from discussions with Paul Spudich, David Boore, and Ken Campbell. We thank Gail Atkinson, Steve Hartzell, and Paul Spudich for careful reviews of the manuscript. Aagaard, Brocher, Simpson, and Jachens were funded by the Earthquake Hazard Program of the U.S. Geological Survey. Graves and Ma were supported with funding from the Southern California Earthquake Center (SCEC). SCEC is funded by NSF Cooperative Agreement EAR-0529922 and USGS Cooperative Agreement 07HQAG0008. Rodgers, Petersson, and Larsen were supported with funding from the Department of Energy and was performed under the auspices of the U.S. Department of Energy by Lawrence Livermore National Laboratory under Contract DE-AC52-07NA27344. This is SCEC contribution number 1425 and LLNL contribution LLNL-JRNL-419883.

References

Aagaard, B. T., T. M. Brocher, D. Dolenc, D. Dreger, R. W. Graves, S. Harmsen, S. Hartzell, S. Larsen, K. McCandless, S. Nilsson, N. A. Petersson, A. Rodgers, B. Sjögreen, and M. L. Zoback (2008, April). Ground motion modeling of the 1906 San Francisco earthquake II: Ground motion estimates for the 1906 earthquake and scenario events. *Bulletin of the Seismological Society of America 98*(2), 1012–1046, doi: 10.1785/0120060410.

Aagaard, B. T., T. M. Brocher, D. Dolenc, D. Dreger, R. W. Graves, S. Harmsen, S. Hartzell, S. Larsen, and M. L. Zoback (2008, April). Ground motion modeling of the 1906 San Francisco earthquake I: Validation using the 1989 Loma Prieta earthquake. *Bulletin of the Seismological Society of America 98*(2), 989–1011, doi: 10.1785/0120060409.

Aagaard, B. T., R. W. Graves, D. P. Schwartz, D. A. Ponce, and R. W. Graymer (2010). Ground motion modeling of Hayward fault scenario earthquakes I: Construction of the suite of scenarios. submitted to BSSA.

Aagaard, B. T., J. F. Hall, and T. H. Heaton (2001, May). Characterization of near-source ground motions with earthquake simulations. *Earthquake Spectra 17*(2), 177–207.

Aagaard, B. T. and T. H. Heaton (2004, December). Near-source ground motions from simulations of sustained intersonic and supersonic fault rupture. *Bulletin of the Seismological Society of America 94*(6), 2064–2078.

Abrahamson, N. and W. Silva (2008, February). Summary of the Abrahamson & Silva NGA ground-motion relations. *Earthquake Spectra 24*(1), 67–97, doi: 10.1193/1.2924360.

Anderson, J. G. (2000, December). *Kocaeli, Turkey, earthquake of August 17, 1999: Reconnaissance report*, Volume 16, Chapter 6: Implications for seismic hazard analysis, pp. 113–137. Earthquake Engineering Research Institute.

Anderson, J. G. and S. E. Hough (1984, October). A model for the shape of the fourier amplitude spectrum of acceleration at high frequencies. *Bulletin of the Seismological Society of America 74*(5), 1969–1993.

Appelö, D. and N. A. Petersson (2008). A stable finite difference method for the elastic wave equation on complex geometries with free surfaces. *Communications in Computational Physics 5*(1), 84–107.

Archuleta, R. J. (1984, June 10). A faulting model for the 1979 Imperial-Valley earthquake. *Journal of Geophysical Research - Solid Earth 89*(B6), 4559–4585.

Bakun, W. H. (1999). Seismic activity of the San Francisco Bay region. *Bulletin of the Seismological Society of America 89*(3), 764–784.

Boatwright, J. and H. Bundock (2008). Modified Mercalli Intensity maps for the 1868 Hayward earthquake plotted in ShakeMap format. Open-File Report 2008-1121, U.S. Geological Survey. http://pubs.usgs.gov/of/2008/1121/ (last accessed 2/18/2009).

Boore, D. M. (1983, December). Stochastic simulation of high-frequency ground motions based on seismological models of the radiated spectra. *Bulletin of the Seismological Society of America 73*(6A), 1865–1894.

Boore, D. M. and G. M. Aktinson (2008, February). Ground-motion prediction equations for the average horizontal component of PGA, PGV, and 5%-damped PSA at spectral periods between 0.01 s and 10.0 s. *Earthquake Spectra 24*(1), 99–138, doi: 10.1193/1.2830434.

Boore, D. M. and W. B. Joyner (1997, April). Site amplifications for generic rock sites. *Bulletin of the Seismological Society of America 87*(2), 327–341.

Bouchon, M., M. P. Bouin, H. Karabulut, M. N. Toksoz, M. Dietrich, and A. J. Rosakis (2001, July 15). How fast is rupture during an earthquake? New insights from the 1999 Turkey earthquakes. *Geophysical Research Letters 28*(14), 2723–2726.

Bouchon, M. and H. Karabulut (2008, June 6). The aftershock signature of supershear earthquakes. *Science 320*(5881), 1323–1325, doi: 10.1126/science.1155030.

Bouchon, M. and H. Karabulut (2009, March/April). What characterizes supershear fault segments? *Seismological Research Letters 80*(2), 299. Abstract, 2009 SSA Annual Meeting.

Bouchon, M., N. Toksoz, H. Karabulut, M. P. Bouin, M. Dietrich, M. Aktar, and M. Edie (2000, September 15). Seismic imaging of the 1999 Izmit (Turkey) rupture inferred from the near-fault recordings. *Geophysical Research Letters 27*(18), 3013–3016.

Bouchon, M. and M. Vallee (2003, August 8). Observation of long supershear rupture during the magnitude 8.1 Kunlunshan earthquake. *Science 301*(5634), 824–826.

Brocher, T. (2008, April). Compressional and shear-wave velocity versus depth relations for common rock types in northern California. *Bulletin of the Seismological Society of America 98*(2), 950–968, doi: 10.1785/0120060403.

Brocher, T. M. (2005, December). A regional view of urban sedimentary basins in northern California based on oil industry compressional-wave velocity and density logs. *Bulletin of the Seismological Society of America 95*(6), 2093–2114, doi: 10.1785/0120050025.

Brocher, T. M., A. L. Ruebel, and E. E. Brabb (1997). Compilation of 59 sonic and density logs from 51 oil test wells in the San Francisco Bay area, California. Open-File Report 97-687, U.S. Geological Survey. http://geopubs.wr.usgs.gov/open-file/of97687/ (last accessed 4/27/2009).

Campbell, K. W. and Y. Bozorgnia (2008, February). NGA ground motion model for the geometric mean horizontal component of PGA, PGV, PGD and 5% damped linear elastic response spectra for periods ranging from 0.01 to 10 s. *Earthquake Spectra 24*(1), 139–171, doi: 10.1193/1.2857546.

Chiou, B. S. and R. R. Youngs (2008, February). An NGA model for the average horizontal component of peak ground motion and response spectra. *Earthquake Spectra 24*(1), 173–215, doi: 10.1193/1.2894832.

Cua, G. B., D. J. Wald, K. Marano, T. Allen, D. Garcia, M. C. Gerstenberger, and C. B. Worden (2010, March/April). Best practices for using macroseismic intensity and ground motion to intensity conversion equations for hazard and loss models. *Seismological Research Letters 81*(2), 292. Abstract, 2010 SSA Annual Meeting.

Day, S. M., R. Graves, J. Bielak, D. Dreger, S. Larsen, K. B. Olsen, A. Pitarka, and L. Ramirez-Guzman (2008, February). Model for basin effects on long-period response spectra in southern California. *Earthquake Spectra 24*(1), 257–277, doi: 10.1193/1.2857545.

Dreger, D. and A. Kaverina (2000). Seismic remote sensing for the earthquake source process and nearsource strong shaking: A case study of the October 16, 1999 Hector Mine earthquake. *Geophysical Research Letters 27*(13), 1941–1944.

Dreger, D. S. and B. Romanowicz (1994). Source characteristics of events in the San Francisco Bay region. Open-File Report 94-176, U.S. Geological Survey.

Dunham, E. M. and R. J. Archuleta (2004, December). Evidence for a supershear transient during the 2002 Denali earthquake. *Bulletin of the Seismological Society of America 68*(6B), S256–S268, doi: 10.1785/0120040616.

Ellsworth, W. L., M. Celebi, J. R. Evans, E. G. Jensen, M. C. Metz, D. J. Nyman, J. W. Roddick, P. Spudich, and C. D. Stephens (2004, August). Near-field ground motions of the M 7.9 November 3, 2002, Denali Fault, Alaska, earthquake recorded at pump station 10. *Earthquake Spectra 20*(3), 597–615.

Frankel, A. (1995, August). Simulating strong motions of large earthquakes using recordings of small earthquakes: the Loma Prieta mainshock as a test case. *Bulletin of the Seismological Society of America 85*(4), 1144–1160.

Frankel, A. D. and D. L. Carver (2009, March/April). Basin surface waves and ground-motion amplification in the San Leandro and Livermore basins, California: Implications for seismic hazard. *Seismological Research Letters 80*(2), 315. Abstract, 2009 SSA Annual Meeting.

Funning, G. J., R. Burgmann, A. Ferretti, and F. Novali (2007). Asperities on the Hayward fault resolved by PS-InSAR, GPS and boundary element modeling. *EOS Trans. 88*(52). S23C-04.

Goldstein, P., M. Dodge, D. Firpo, and L. Minner (2003). *The IASPEI International Handbook of Earthquake and Engineering Seismology*, Chapter SAC2000: Signal processing and analysis tools for seismologists and engineers. London: Academic Press.

Graves, R. W. (1996, August). Simulating seismic-wave propagation in 3-D elastic media using staggered-grid finite-differences. *Bulletin of the Seismological Society of America 86*(4), 1091–1106.

Graves, R. W., B. T. Aagaard, K. W. Hudnut, L. M. Star, J. P. Stewart, and T. H. Jordan (2008, November). Broadband simulations for Mw 7.8 southern San Andreas earthquakes: Ground motion sensitivity to rupture speed. *Geophysical Research Letters 35*(L22302), doi: 10.1029/2008GL035750.

Graves, R. W. and A. Pitarka (2004). Broadband time history simulation using a hybrid approach. In *13th World Conference on Earthquake Engineering Conference Proceedings*, Vancouver, Canada. paper no. 1098.

Graymer, R. W. (2000). *Geologic map and map database of the Oakland metropolitan area, Alameda, Contra Costa, and San Francisco Counties, California*. U.S. Geological Survey Map MF-2342. 1 sheet, scale 1:50,000, http://pubs.usgs.gov/mf/2000/2342/ (last accessed 2009/04/15).

Harmsen, S., S. Hartzell, and P. Liu (2008, June). Simulated ground motion in Santa Clara Valley, California, and vicinity from m$\geq$6.7 scenario earthquakes. *Bulletin of the Seismological Society of America 98*(3), 1243–1271, doi: 10.1785/0120060230.

Hartzell, S., S. Harmsen, A. Frankel, and S. Larsen (1999, December). Calculation of broadband time histories of ground motion: Comparison of methods and validation using strong-ground motion from the 1994 Northridge earthquake. *Bulletin of the Seismological Society of America 89*(6), 1484–1504.

Hartzell, S., S. Harmsen, R. A. Williams, D. Carver, A. Frankel, G. Choy, R. C. Jachens, T. M. Brocher, and C. M. Wentworth (2006, October). Modeling and validation of a 3D velocity structure for the Santa Clara Valley, California, for seismic-wave simulations. *Bulletin of the Seismological Society of America 96*(5), 1851–1881, doi: 10.1785/0120050243.

Kim, A., D. S. Dreger, and S. Larsen (2010, April). Moderate earthquake ground-motion validation in the San Francisco Bay area. *Bulletin of the Seismological Society of America 100*(2), 819–825, doi: 10.1785/0120090076.

Larsen, S. and C. A. Schultz (1995). Elas3d: 2D/3D elastic finite-difference wave propagation code. Technical Report UCRL-MA-121792, Lawrence Livermore National Laboratory. 19 p.

Larsen, S. C., D. Dreger, M. Antolik, and C. Stidham (2000). 3-D simulations of scenario earthquake along the Hayward fault. Technical Report UCRL-ID-137645, Lawrence Livermore National Laboratory. 8 p.

Liu, P., R. J. Archuleta, and S. H. Hartzell (2006, December). Prediction of broadband ground-motion time histories: Hybrid low/high- frequency method with correlated random source parameters. *Bulletin of the Seismological Society of America 96*(6), 2118–2130, doi: 10.1785/0120060036.

Ma, S., R. J. Archuleta, and M. J. Page (2007, December). Effects of large-scale surface topography on ground motions, as demonstrated by a study of the San Gabriel Mountains, Los Angeles, California. *Bulletin of the Seismological Society of America 97*(6), 2066–2079, doi: 10.1785/0120070040.

Ma, S. and P. Liu (2006, October). Modeling of the perfectly matched layer absorbing boundaries and intrinsic attenuation in explicit finite-element methods. *Bulletin of the Seismological Society of America 96*(5), 1779–1794, doi: 10.1785/0120050219.

Ma, S., G. A. Prieto, and G. C. Beroza (2008, December). Testing community velocity models for Southern California using the ambient seismic field. *Bulletin of the Seismological Society of America 98*(6), 2694–2714, doi: 10.1785/0120080947.

Nilsson, S., N. A. Petersson, B. Sjögreen, and H. O. Kreiss (2007). Stable difference approximations for the elastic wave equation in second order formulation. *SIAM Journal on Numerical Analysis 45*(5), 1902–1936.

Olson, A. H. and R. J. Apsel (1982, December). Finite faults and inverse-theory with applications to the 1979 Imperial-Valley earthquake. *Bulletin of the Seismological Society of America 72*(6), 1969–2001.

Pasyanos, M. E., D. Dreger, and B. Romanowicz (1996, October). Toward real-time estimation of regional moment tensors. *Bulletin of the Seismological Society of America 86*(5), 1255–1269.

Rodgers, A., N. A. Petersson, S. Nilsson, B. Sjogreen, and K. McCandless (2008, April). Broadband waveform modeling of moderate earthquakes in the San Francisco Bay Area and preliminary assessment of the USGS 3-D seismic velocity model. *Bulletin of the Seismological Society of America 98*(2), 969–988, doi: 10.1785/0120060407.

Rowshandel, B. (XXXX). Fault rupture directivity effects in the next generation attenuation relations. submitted to Earthquake Spectra.

Seekins, L. and J. Boatwright (2007). Rupture directions for selected northern California earthquakes. http://earthquake.usgs.gov/regional/nca/rupture/. last accessed November, 2009.

Sekiguchi, H. and T. Iwata (2002, February). Rupture process of the 1999 Kocaeli, Turkey, earthquake estimated from strong-motion waveforms. *Bulletin of the Seismological Society of America 92*(1), 300–311.

Somerville, P. G., K. Irikura, R. Graves, S. Sawada, D. Wald, N. Abrahamson, Y. Iwasaki, T. Kagawa, N. Smith, and A. Kowada (1999, January/February). Characterizing crustal earthquake slip models for the prediction of strong ground motion. *Seismological Research Letters 70*(1), 199–222.

Somerville, P. G., N. F. Smith, R. W. Graves, and N. A. Abrahamson (1997, January/February). Modification of empirical strong ground motion attenuation relations to include the amplitude and duration effects of rupture directivity. *Seismological Research Letters 68*(1), 199–222.

Spudich, P. and B. S. J. Chiou (2008, February). Directivity in NGA earthquake ground motions: Analysis using isochrone theory. *Earthquake Spectra 24*(1), 279–298, doi: 10.1193/1.2928225.

Spudich, P. and E. Cranswick (1984, December). Direct observation of rupture propagation during the 1979 Imperial Valley earthquake using a short baseline accelerometer array. *Bulletin of the Seismological Society of America 74*(6), 2083–2114.

Stover, C. W. and J. L. Coffman (1993). Seismicity of the United States, 1568–1989 (revised). Professional Paper 1527, U.S. Geological Survey.

Thurber, C. H., T. M. Brocher, H. Zhang, and V. E. Langenheim (2007). Three-dimensional P wave velocity model for the San Francisco Bay region, California. *Journal of Geophysical Research - Solid Earth 112*(B07313), doi: 10.1029/2006JB004682.

Wald, D., B. Worden, V. Quitoriano, and K. Pankow (2005, May). *ShakeMap Manual: Technical Manual, Users Guide, and Software Guide* (Version 1.0 ed.). United States Geological Survey. http://pubs.usgs.gov/tm/2005/12A01/.

Walling, M., W. Silva, and N. Abrahamson (2008, February). Nonlinear site amplification factors for constraining the nga models. *Earthquake Spectra 24*(1), 243–255, doi: 10.1193/1.2934350.

Wessel, P. and W. H. F. Smith (1998). New, improved version of the generic mapping tools released. *EOS Transactions 79*, 579.

Williams, A. J., T. M. Brocher, W. D. Mooney, and A. Boken (1999). Data report for seismic refraction surveys conducted from 1980 to 1982 in the Livermore Valley and the Santa Cruz mountains, California. Open-File Report 99-146, U.S. Geological Survey. http://geopubs.wr.usgs.gov/open-file/of99-146/ (last accessed 4/27/2009).

Wills, C. J., M. Petersen, W. A. Bryant, M. Reichle, G. J. Saucedo, S. Tan, G. Taylor, and J. Treiman (2000, December). A site-conditions map for California based on geology and shear-wave velocity. *Bulletin of the Seismological Society of America 90*(6B), S187–S208, doi: 10.1785/0120000503.

Working Group on California Earthquake Probabilities (WGCEP) (2003). Earthquake probabilities in the San Francisco Bay region: 2002–2031. Open-File Report 03-214, U.S. Geological Survey.

Working Group on California Earthquake Probabilities (WGCEP) (2008). The uniform California earthquake rupture forecast, version 2 (UCERF 2). Open-File Report 2007-1437, U.S. Geological Survey. http://pubs.usgs.gov/of/2007/1437/ (last accessed 2/18/2009).

Yu, E. and P. Segall (1996). Slip in the 1868 Hayward earthquake from the analysis of historical triangulation data. *Journal of Geophysical Research - Solid Earth 101*(B7), 16101–16118, doi: 10.1029/96JB00806.

U.S. Geological Survey, MS977
345 Middlefield Rd.
Menlo Park, CA 94025
(B.T.A., T.M.B., R.W.S.)

URS Corporation
566 El Dorado St.
Pasadena, CA 91101
(R.W.G.)

Deptartment of Geol. Sciences
San Diego State University
5500 Campanile Dr.
San Diego, CA 92182-1020
(S.M.)

Lawrence Livermore National Laboratory
Box 808, L-103
Livermore, CA 94551-0808
(S.C.L.)

Center for the Study of Imaging and Dynamics of the Earth
University of California, Santa Cruz
Santa Cruz, CA 95064
and Lawrence Livermore National Laboratory
7000 East Ave, L-046
Livermore, CA 94551
(A.R.)

Center for Applied Scientific Computing
Computations Directorate
Lawrence Livermore National Laboratory
Box 808, L-422
Livermore, CA 94551-0808
(N.A.P.)

U.S. Geological Survey, MS989
345 Middlefield Rd.
Menlo Park, CA 94025
(R.J.)

Seismological Laboratory
University of California, Berkeley
215 McCone Hall
Berkeley, CA 94720
(D.D.)

Table 1. Wave Propagation Codes and Modeling Domains

	Aagaard	Graves	Larsen	Ma	Rodgers
Domain					
Length	210 km	220 km	220 km	200 km	200 km
Width	126 km	280 km	150 km	120 km	120 km
Max. depth	40 km	45 km	45 km	36 km	40 km
NW corner	-123.4900, 38.2106	-123.6806, 38.1748	-123.5538, 38.3068	-123.4900, 38.2100	-123.3592, 38.1664
NE corner	-122.3313, 38.8890	-121.6198, 39.3223	-122.1802, 39.0988	-122.3800, 38.8500	-122.2500, 38.8000
SE corner	-120.9265, 37.3568	-119.9391, 37.3956	-120.7000, 37.5000	-121.0300, 37.4000	-120.9216, 37.3465
SW corner	-122.0742, 36.6920	-121.9729, 36.2774	-122.0669, 36.7080	-122.1400, 36.7600	-122.0206, 36.7129
Projection	transverse Mercator	oblique Mercator	spheroidal	spheroidal	spheroidal
Discretization	unstructured FE	staggered-grid FD	staggered-grid FD	structured FE	node-centered FD
Space	2nd order	4th order	4th order	2nd order	2nd order
Time	2nd order	2nd order	2nd order	2nd order	2nd order
Resolution	variable	125 m	100 m	variable	100 m
Bandwidth	T > 2.0 s	T > 1.0 s	T > 1.0 s	T > 2.0 s	T > 2.0 s
Min. Vs	700 m/s	620 m/s	500 m/s	500 m/s	500 m/s
Features					
Topography	yes	"squashed"	yes	yes	yes
Water	air filled	N/A	included	air filled	air filled
Mat. Properties	USGS 08.3.0	USGS 08.3.0	USGS 08.3.0	USGS 08.3.0	USGS 08.3.0
Attenuation	no	Graves	USGS VM08.3.0	no	no
Eq source	offset in mesh	point sources	point sources	point sources	point sources
# pt. sources	N/A	31,460	31,460	31,460	10,500
Fault surface	3-D geologic model	3-D geologic model	3-D geologic model	3-D geologic model	3-D geologic model

The corners of the bounding boxes of each domain are given in longitude and latitude (WGS84 horizontal datum).

Table 2. Earthquake Scenarios

Name	Rupture Segments	Slip Distribution	Hypocenter	Rupture Speed	Rise Time	Moment Magnitude	Modeling Groups
HS G01 HypoO	HS	G01	Oakland	*Vr92*	*Tr15*	6.76	A,G,L,M,R
HS G01 HypoH	HS	G01	Hayward	*Vr92*	*Tr15*	6.76	A,G,L,M,R
HS G01 HypoF	HS	G01	Fremont	*Vr92*	*Tr15*	6.76	A,G,L,M,R
HS G02 HypoO	HS	G02	Oakland	*Vr92*	*Tr15*	6.76	A
HS G02 HypoH	HS	G02	Hayward	*Vr92*	*Tr15*	6.76	A
HS G02 HypoF	HS	G02	Fremont	*Vr92*	*Tr15*	6.76	A
HS P01 HypoO	HS	P01	Oakland	*Vr92*	*Tr15*	6.84	A
HS P01 HypoH	HS	P01	Hayward	*Vr92*	*Tr15*	6.84	A
HS P01 HypoF	HS	P01	Fremont	*Vr92*	*Tr15*	6.84	A
HS+HN G04 HypoSPB	HS+HN	G04	San Pablo Bay	*Vr92*	*Tr15*	7.05	A,G,L,R
HS+HN G04 HypoO	HS+HN	G04	Oakland	*Vr92*	*Tr15*	7.05	A,G,L,M,R
HS+HN G04 HypoF	HS+HN	G04	Fremont	*Vr92*	*Tr15*	7.05	A,G,L,R
HS+HN P03 HypoSPB	HS+HN	P03	San Pablo Bay	*Vr92*	*Tr15*	6.97	A
HS+HN P03 HypoO	HS+HN	P03	Oakland	*Vr92*	*Tr15*	6.97	A
HS+HN P03 HypoF	HS+HN	P03	Fremont	*Vr92*	*Tr15*	6.97	A
CC+HS G03 HypoO	CC+HS	G03	Oakland	*Vr92*	*Tr15*	6.90	A
CC+HS G03 HypoH	CC+HS	G03	Hayward	*Vr92*	*Tr15*	6.90	A
CC+HS G03 HypoAR	CC+HS	G03	Alum rock	*Vr92*	*Tr15*	6.90	A
CC+HS P02 HypoO	CC+HS	P02	Oakland	*Vr92*	*Tr15*	6.94	A
CC+HS P02 HypoH	CC+HS	P02	Hayward	*Vr92*	*Tr15*	6.94	A
CC+HS P02 HypoAR	CC+HS	P02	Alum Rock	*Vr92*	*Tr15*	6.94	A
HN+RC G05 HypoSPB	HN+RC	G05	San Pablo Bay	*Vr92*	*Tr15*	6.89	A
HN+RC P04 HypoSPB	HN+RC	P04	San Pablo Bay	*Vr92*	*Tr15*	7.11	A
HS+HN+RC G06 HypoSPB	HS+HN+RC	G06	San Pablo Bay	*Vr92*	*Tr15*	7.16	A
HS+HN+RC P05 HypoSPB	HS+HN+RC	P05	San Pablo Bay	*Vr92*	*Tr15*	7.20	A
HS Vr82	HS	*G01*	*Hayward*	Vr82	*Tr15*	6.76	M
HS Vr141	HS	*G01*	*Hayward*	Vr141	*Tr15*	6.76	M
HS+HN Vr82	HS+HN	*G04*	*Oakland*	Vr82	*Tr15*	7.05	M
HS+HN Vr141	HS+HN	*G04*	*Oakland*	Vr141	*Tr15*	7.05	M
HS Tr10	HS	*G01*	*Hayward*	*Vr92*	Tr10	6.76	L
HS Tr20	HS	*G01*	*Hayward*	*Vr92*	Tr20	6.76	L
HS Tr10u	HS	*G01*	*Hayward*	*Vr92*	Tr10u	6.76	L
HS+HN Tr10	HS+HN	*G04*	*Oakland*	*Vr92*	Tr10	7.05	L
HS+HN Tr20	HS+HN	*G04*	*Oakland*	*Vr92*	Tr20	7.05	L
HS+HN Tr20u	HS+HN	*G04*	*Oakland*	*Vr92*	Tr20u	7.05	L
HS N01	HS	N01	*Hayward*	*Vr92*	*Tr15*	6.89	A
HS F01	HS	F01	*Hayward*	*Vr92*	*Tr15*	6.61	A
HS+HN N04	HS+HN	N04	*Oakland*	*Vr92*	*Tr15*	7.12	A
HS+HN F04	HS+HN	F04	*Oakland*	*Vr92*	*Tr15*	6.82	A

Figure 5 shows the rupture lengths and epicenters. The rise time labels Tr10, Tr15, and Tr20 correspond to values of 1.0, 1.5, and 2.0 for C in the expression for the rise time, $t_{95}/t_0 = C\sqrt{D_f/D_0}$, and the labels Tr10u and Tr20u correspond to nominally uniform rise times of 1.0 s and 2.0 s. The rupture speed labels Vr92, Vr82, and Vr141 correspond to the correlations between rupture speed and slip. The maximum local rupture speeds for Vr92, Vr82, and Vr141 are 0.92 Vs, 0.82 Vs, and $\sqrt{2}$ Vs, respectively. The modeling groups are Aagaard (A), Graves (G), Larsen (L), Ma (M), and Rodgers (R). We form the scenario names from abbreviations of the parameters but do not include parameters with significant redundancy (which are shown in italics).

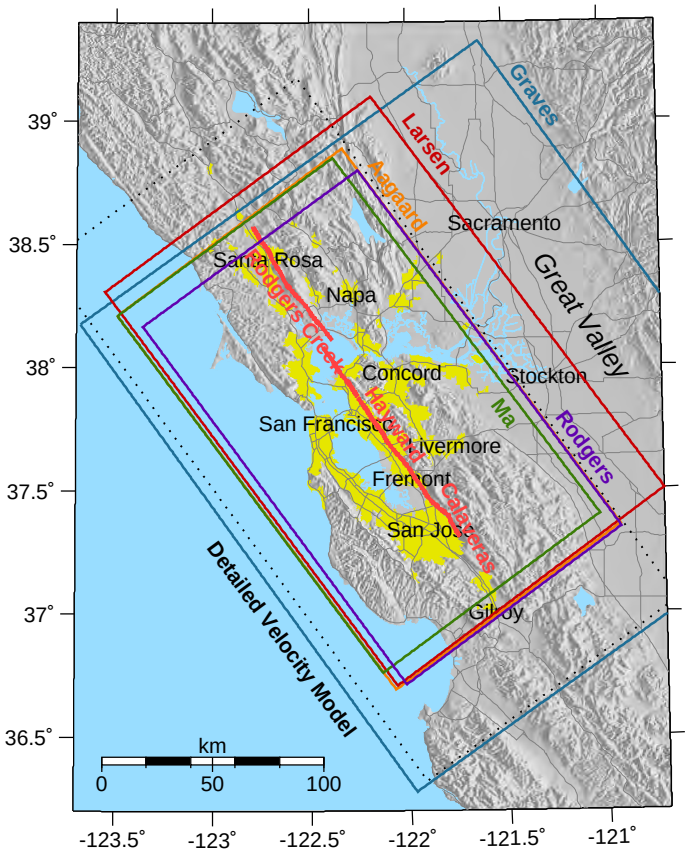

Figure 1. Bounding boxes of the domains (colored boxes) used by the five ground-motion modeling groups and the detailed portion of the USGS Bay Area Velocity Model 08.3.0. (dotted black box). The red lines show the extent of rupture on the surface traces in our scenario earthquakes on the Hayward, Rodgers Creek, and Calaveras faults. The shaded yellow region delineates the San Francisco Bay urban area.

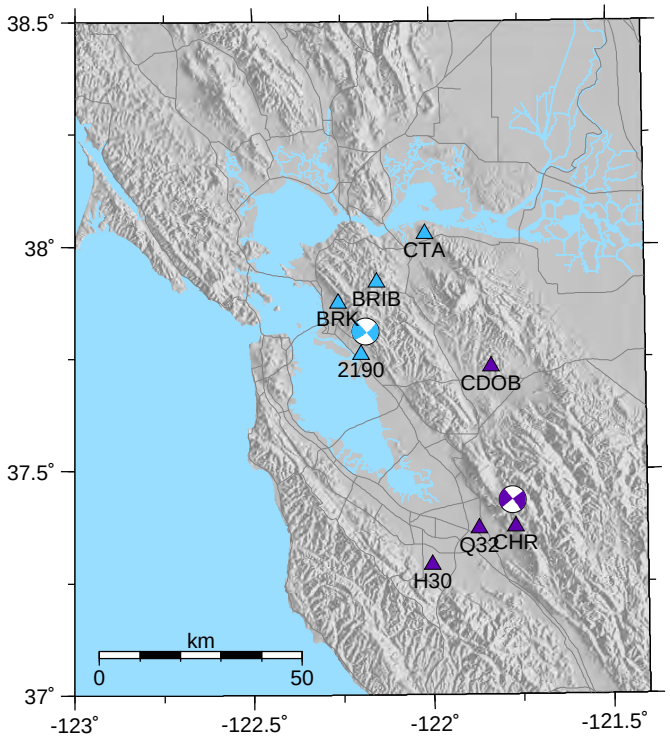

Figure 2. Map of the San Francisco Bay Area showing the double couple focal mechanisms for the two moderate earthquakes we modeled for validation: 2007/10/31 Alum Rock (Mw 5.45) in purple and 2007/07/20 Oakland (Mw 4.18) in blue. Also shown are seismic stations (triangles, color coded by event) used for waveform comparisons in Figures 3 and 4.

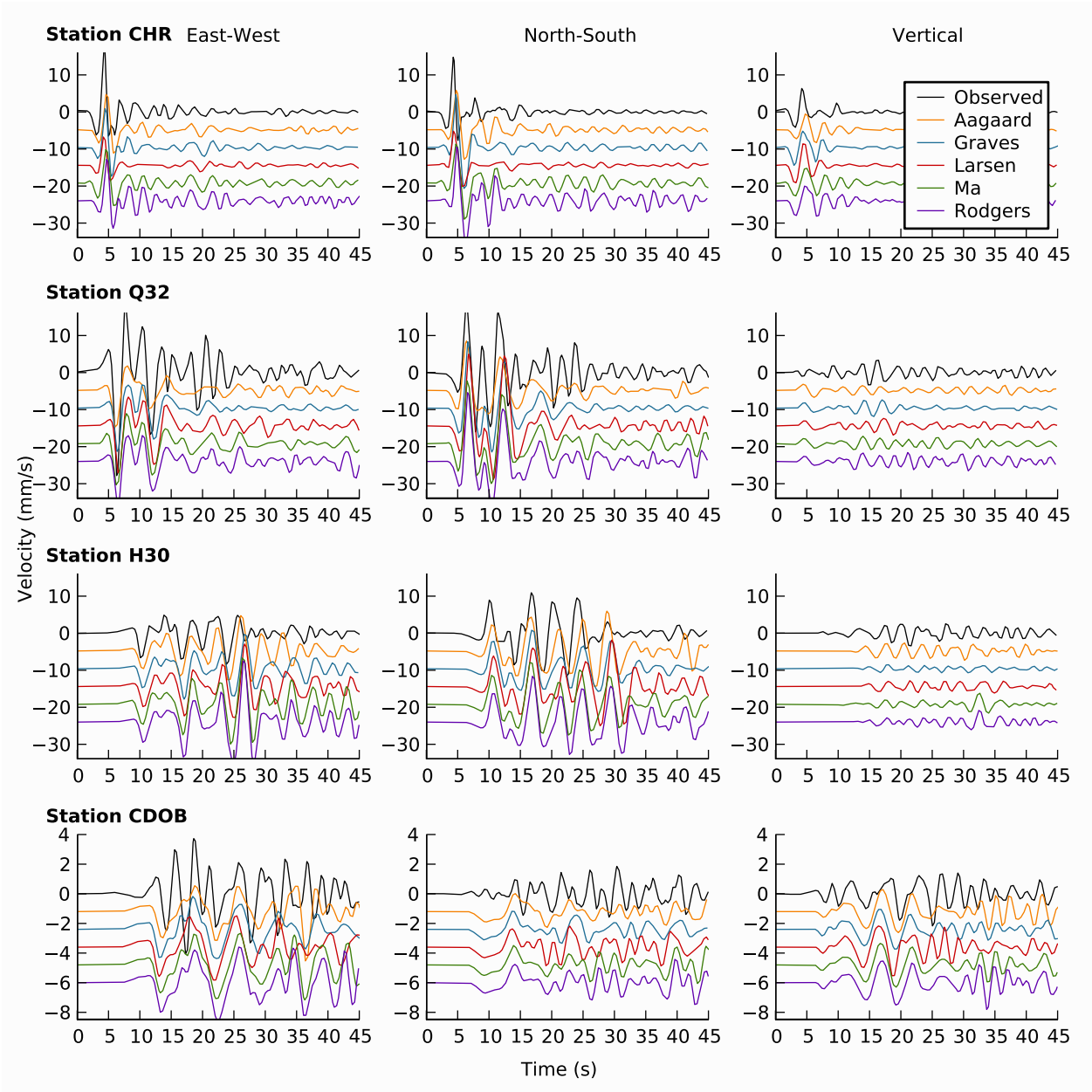

Figure 3. Observed (black) and simulated (color-coded by modeling group) velocity waveforms at four stations in the San Francisco Bay area for the 2007/10/31 Alum Rock earthquake. The velocity waveforms have been low-pass filtered to a common bandwidth of T > 2.0 s using two passes of a two-pole Butterworth filter with a corner frequency of 0.5 Hz.

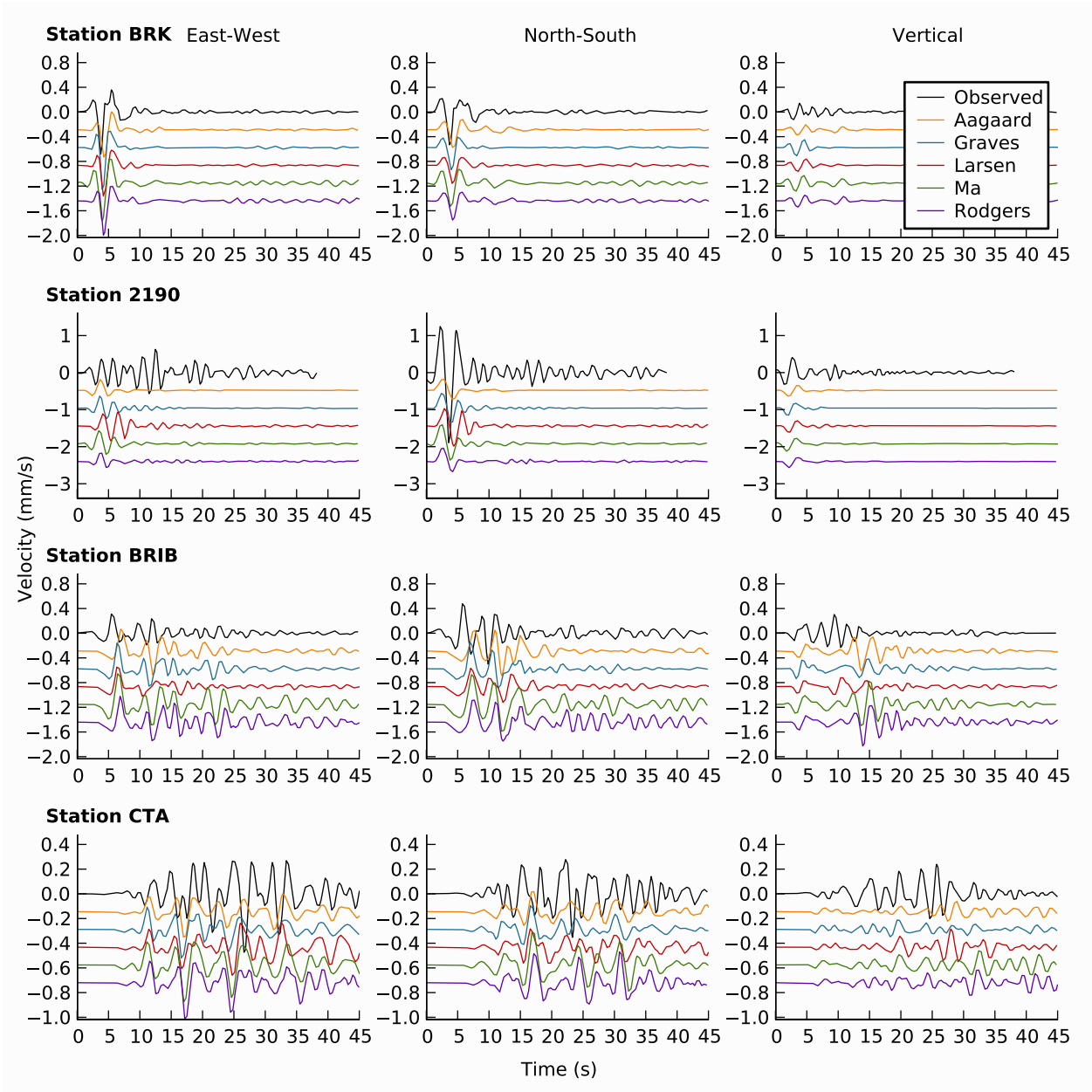

Figure 4. Observed (black) and simulated (color-coded by modeling group) velocity waveforms at four stations in the San Francisco Bay area for the 2007/07/20 Oakland earthquake. The velocity waveforms have been low-pass filtered to a common bandwidth of T > 2.0 s using two passes of a two-pole Butterworth filter with a corner frequency of 0.5 Hz.

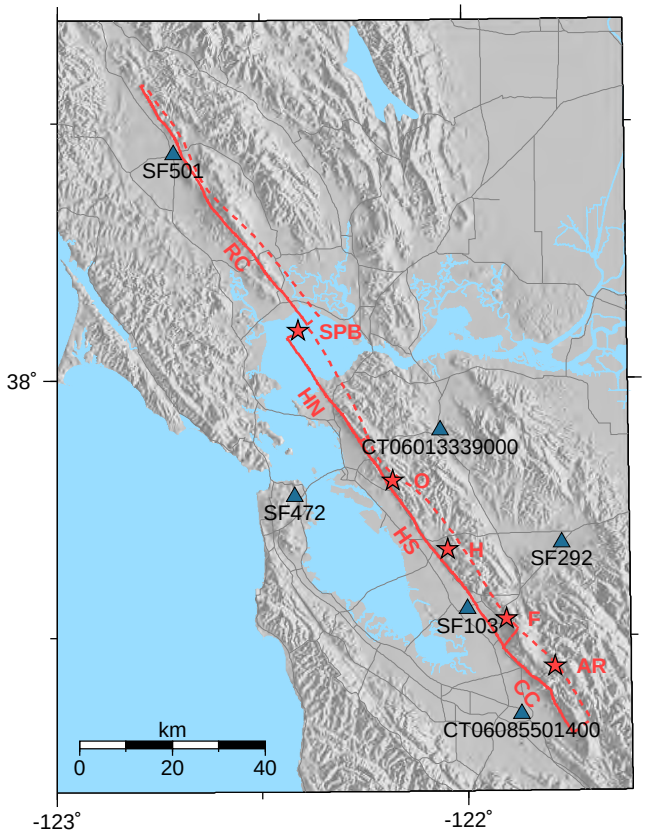

Figure 5. Rupture segments (surfaces traces in solid lines and down-dip extent of rupture in dashed lines) which are combined into the five rupture lengths. The epicenters (stars) are offset from the surface trace due to the 3-D geometry of the fault surface. The rupture segments include the Central Calaveras (CC), Hayward South (HS), Hayward North (HN), and Rodgers Creek (RC). The epicenters include San Pablo Bay (SPB), Oakland (O), Hayward (H), Fremont (F), and Alum Rock (AR).

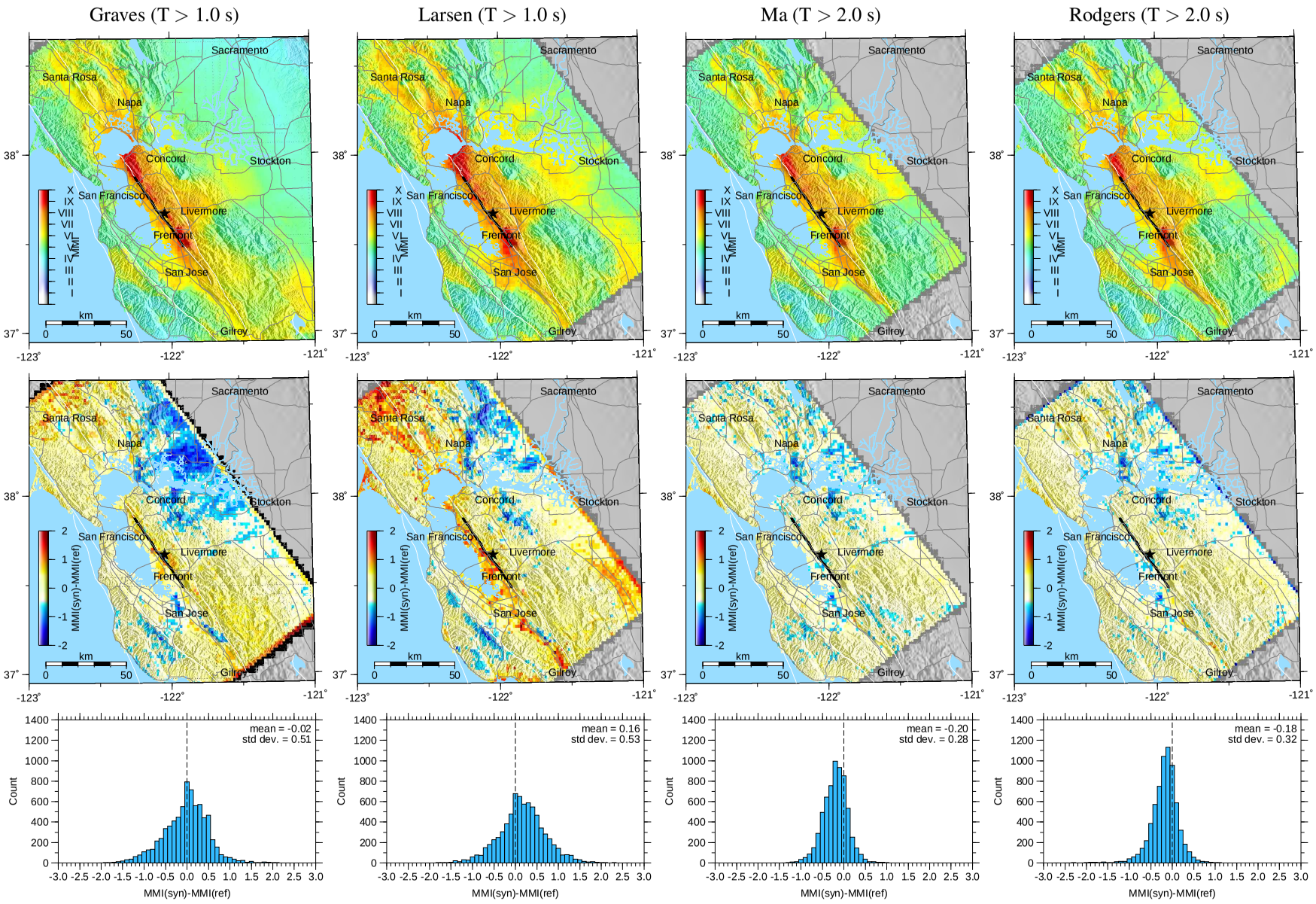

Figure 6. Comparison of Modified Mercalli Intensity (MMI) across the modeling groups for scenario HS G01 HypoH. The lower two rows show the residuals with respect Aagaard's MMI values (see Figure 8). The black line indicates the rupture and the black star identifies the epicenter. Aagaard, Ma, and Rodgers use the same minimum period and similar minimum shear wave speeds without intrinsic attenuation, resulting in very small residuals. Larsen and Graves include shorter periods and intrinsic attenuation, resulting in lower amplitudes in the Great Valley.

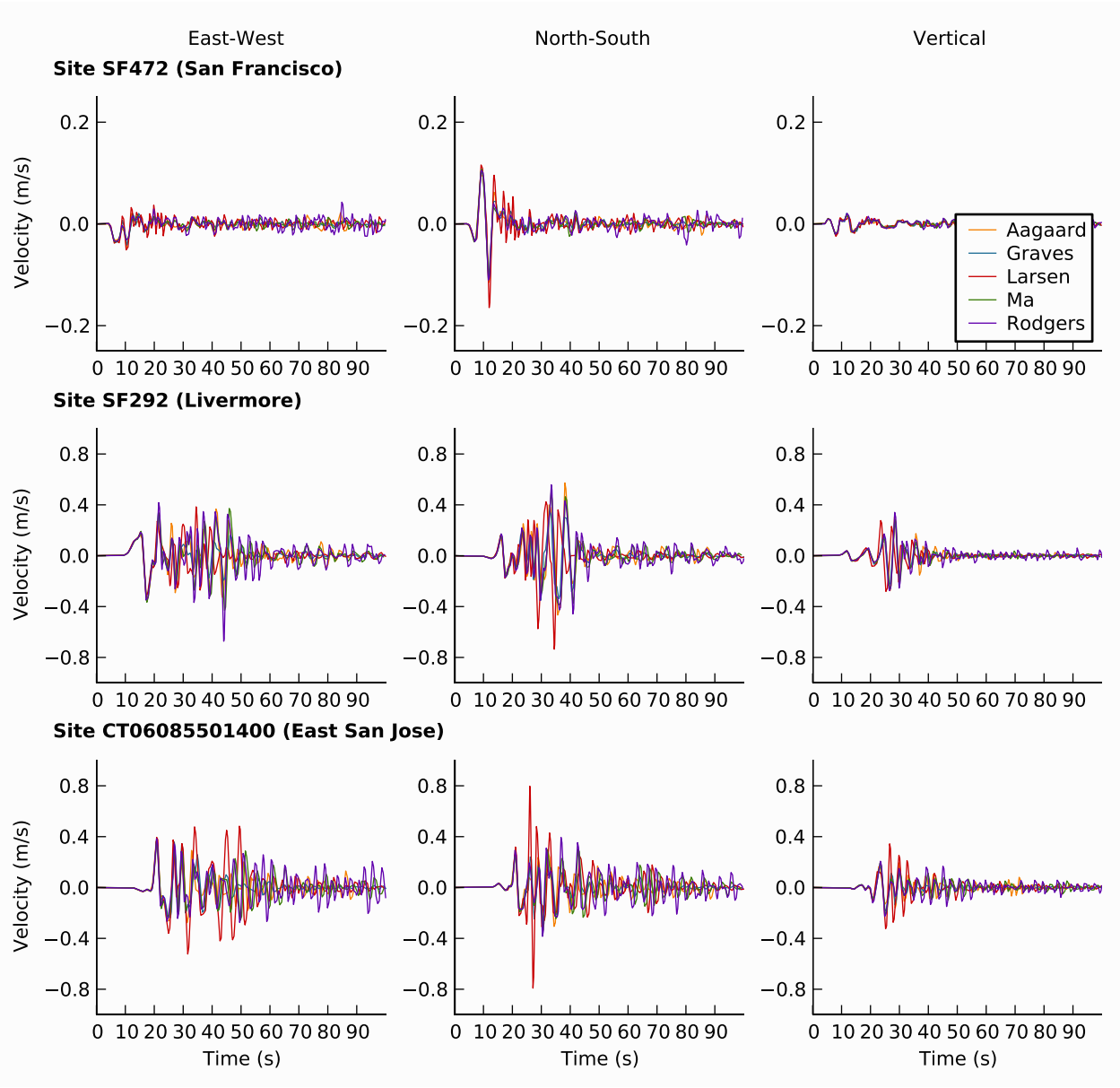

Figure 7. Velocity waveforms at three sites (see Figure 5) for scenario HS G01 HypoH for each of the five modeling groups. We have low-pass filtered the waveforms to a common bandwidth of T > 2.0 s using two passes of a two-pole Butterworth filter with a corner frequency of 0.5 Hz. The waveforms demonstrate consistency in the amplitude and duration of shaking with nearly identical initial arrivals and some secondary arrivals.

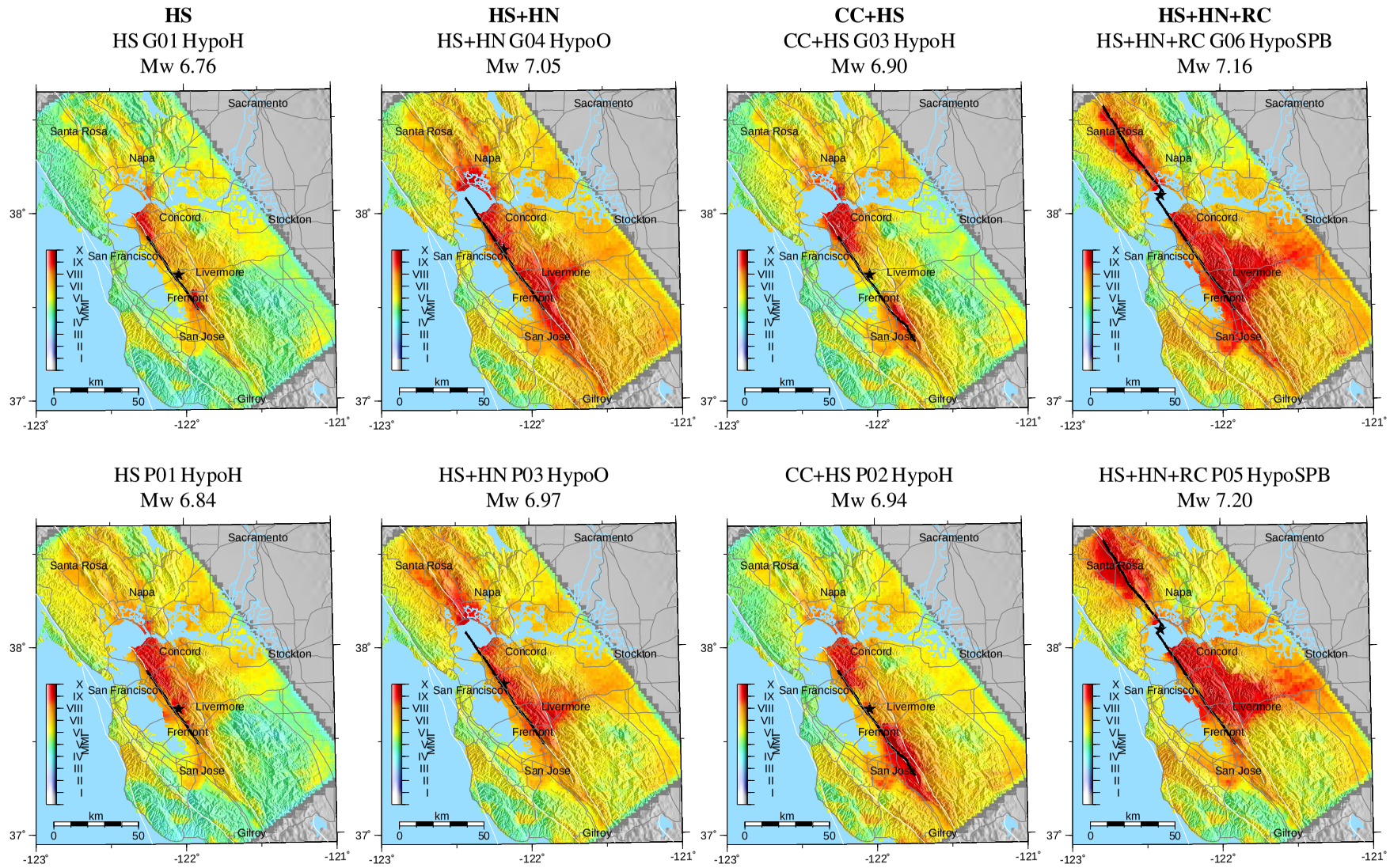

Figure 8. Modified Mercalli Intensities from Aagaard's long-period (T > 2.0 s) simulations of eight scenario earthquakes with different rupture lengths and slip distributions. Top row uses the slip-gradient approach for accounting for the effects of creep on the slip distribution, and the bottom row uses the slip-predictable approach. The black line indicates the rupture and the black star identifies the epicenter.

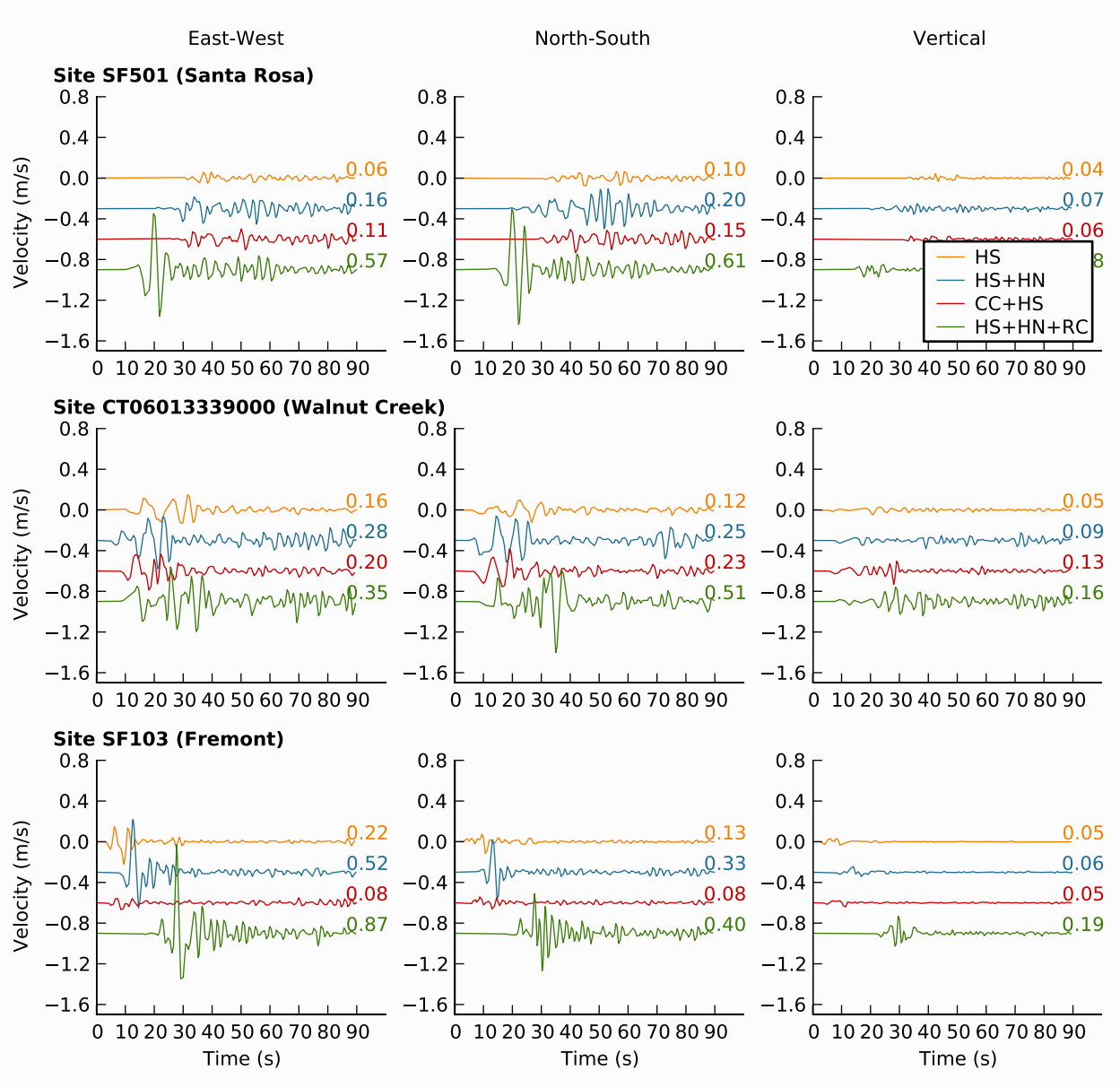

Figure 9. Velocity waveforms from Aagaard's long-period (T > 2.0 s) simulations of four scenario earthquakes with different rupture lengths and slip distributions. The scenarios are identified by their rupture lengths and include HS G01 HypoH (Mw 6.76), HS+HN G04 HypoO (Mw 7.05), CC+HS G03 HypoH (Mw 6.90), and HS+HN+RC G05 HypoSPB (Mw 7.16). The value on the right side of each trace indicates the peak velocity.

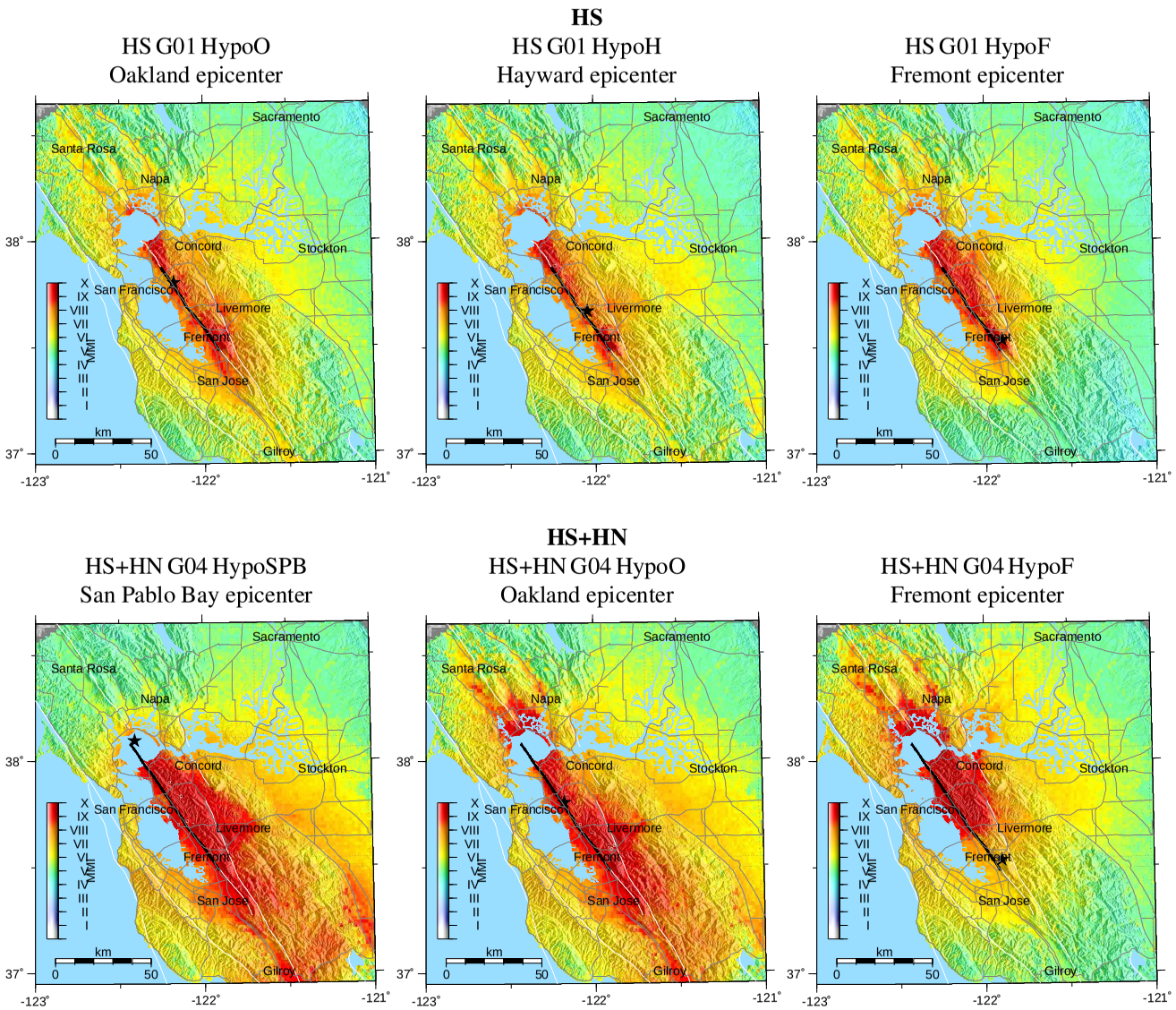

Figure 10. Modified Mercalli Intensities from Graves's broadband (T > 0.1 s) simulations of six scenario earthquakes with different hypocenters for the Hayward South rupture length (top row) and the Hayward South + North rupture length (bottom row). The black line indicates the rupture and the black star identifies the epicenter. Changing the hypocenter has a strong impact on the distribution of shaking by altering the rupture directivity. The Hayward South scenarios use slip distribution G01 which differs significantly from slip distribution G04 used in the Hayward South + North simulations.

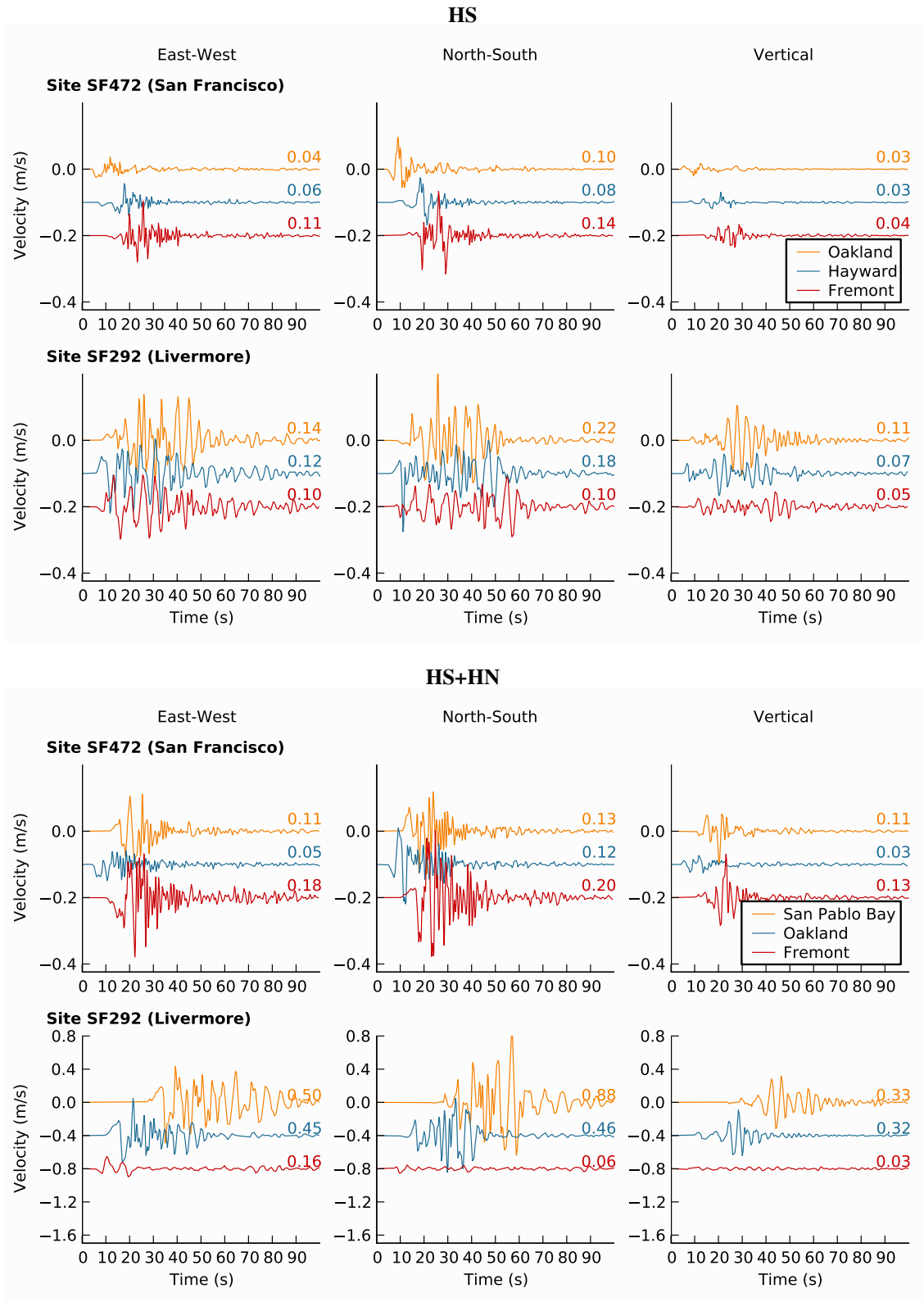

Figure 11. Velocity waveforms from Graves's broadband (T > 0.1 s) simulations of six scenario earthquakes with different hypocenters. The top two rows show waveforms for the Hayward South rupture length (scenarios HS G01 HypoO, Oakland epicenter; HS G01 HypoH, Hayward epicenter; and HS G01 HypoF, Fremont epicenter) and the bottom two rows show waveforms for the Hayward South + North rupture length (scenarios HS+HN G04 HypoSPB, San Pablo Bay epicenter; HS+HN G04 HypoO, Oakland epicenter; and HS+HN G04 HypoF, Fremont epicenter). The value on the right side of each trace indicates the peak velocity.

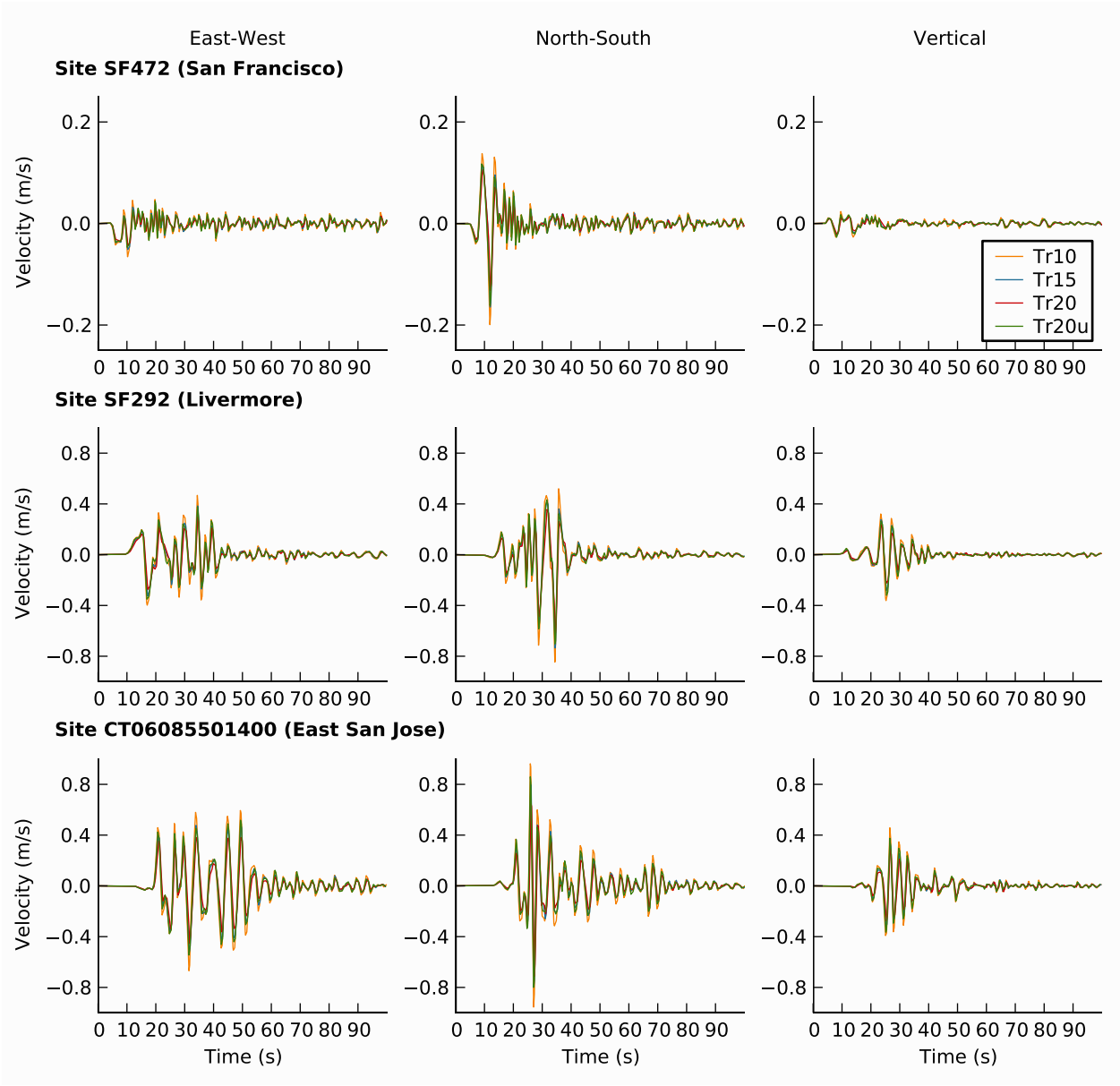

Figure 12. Velocity waveforms from Larsen's long-period (T > 1.0 s) simulations of four scenario earthquakes with different rise time distributions. The scenarios are identified by the rise time and include HS+HN Tr10, HS+HN G04 HypoO (Tr15), HS+HN Tr20, and HS+HN Tr20u. The ground motions exhibit a relatively weak sensitivity to the variation in the rise time distribution.

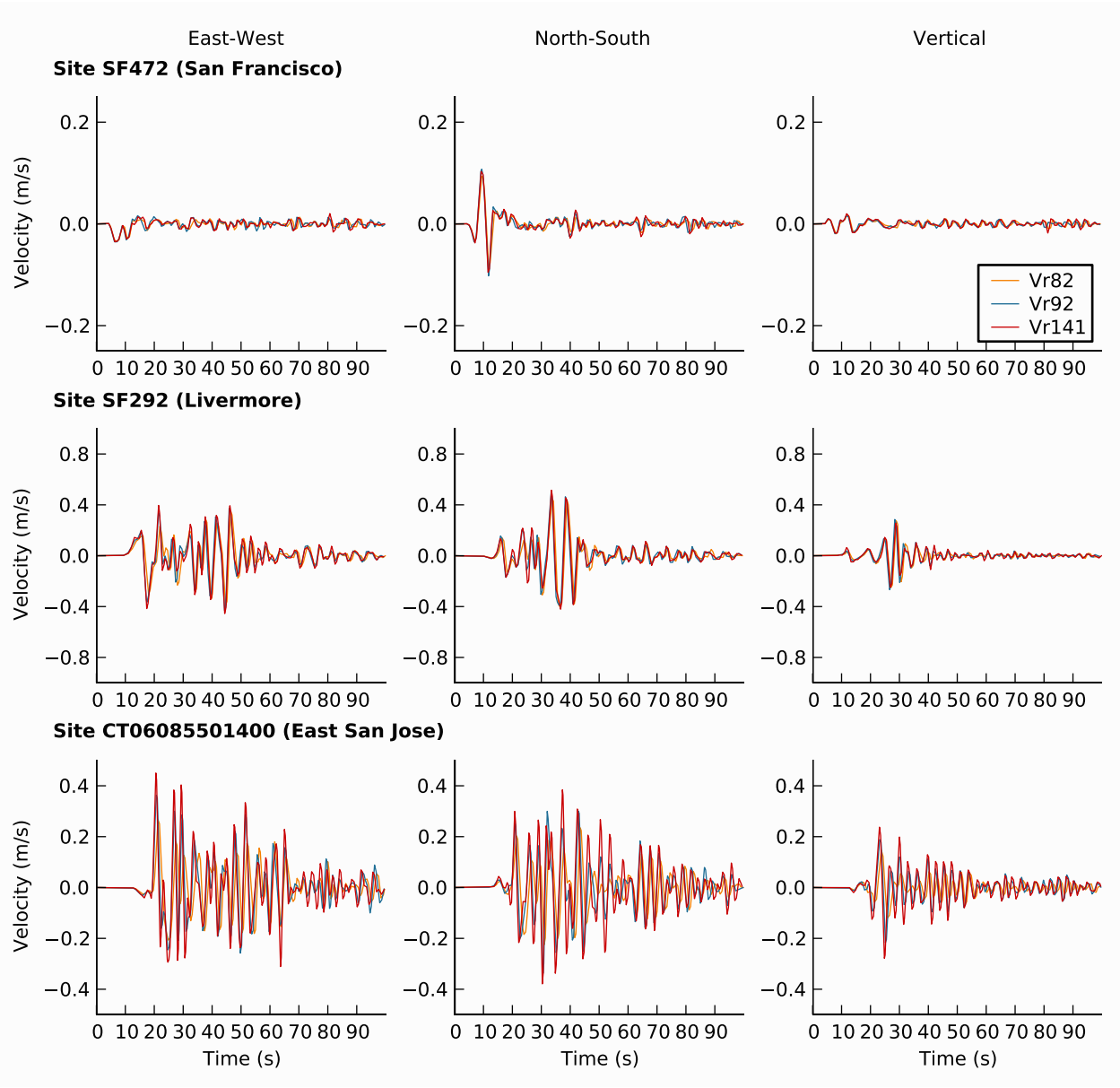

Figure 13. Velocity waveforms from Ma's long-period (T > 2.0 s) simulations of three scenario earthquakes with different rupture speed distributions. The scenarios are identified by the rupture speed and include HS+HN Vr82, HS+HN G04 HypoO (Vr92), and HS+HN Vr141. The ground motions exhibit a relatively weak sensitivity to the variation in the rupture speed distribution.

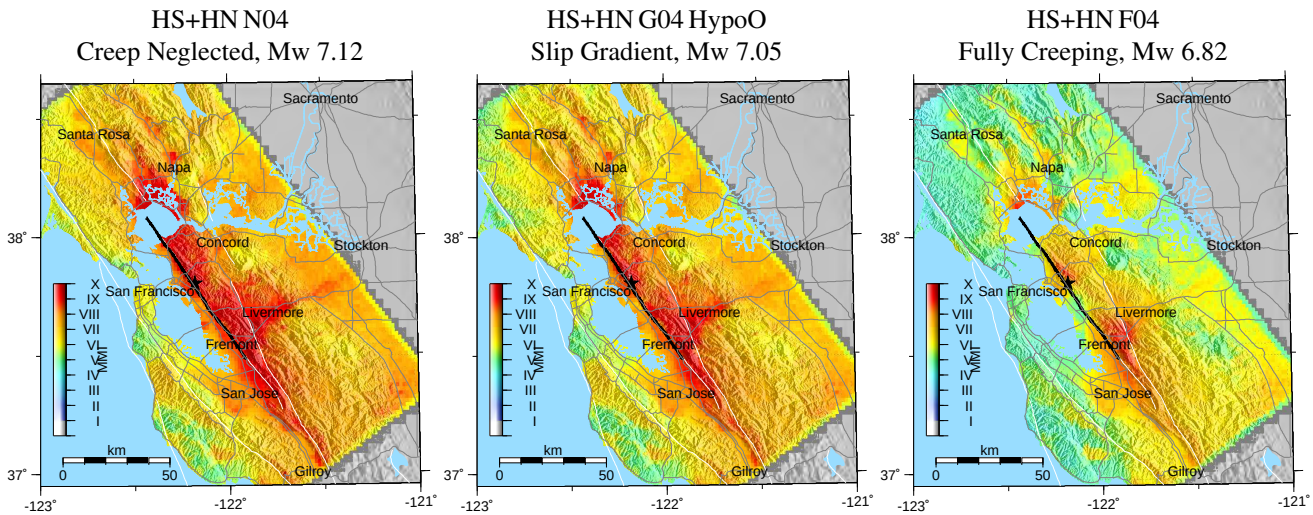

Figure 14. Modified Mercalli Intensities from Aagaard's long-period (T > 2.0 s) simulations of three scenario earthquakes with different vertical gradients in the slip distribution in creeping regions. Scenario HS+HN N04 uses to a vertical gradient of 0 (neglecting creep), scenario HS+HN G04 HypoO uses a vertical gradient of -0.12 m/km, and scenario HS+HN F04 uses an infinite vertical gradient (preventing coseismic slip in creeping regions). The black line indicates the rupture and the black star identifies the epicenter. Creep reduces the coseismic slip in creeping regions, which lowers the magnitude and decreases the efficiency of radiating surface waves.

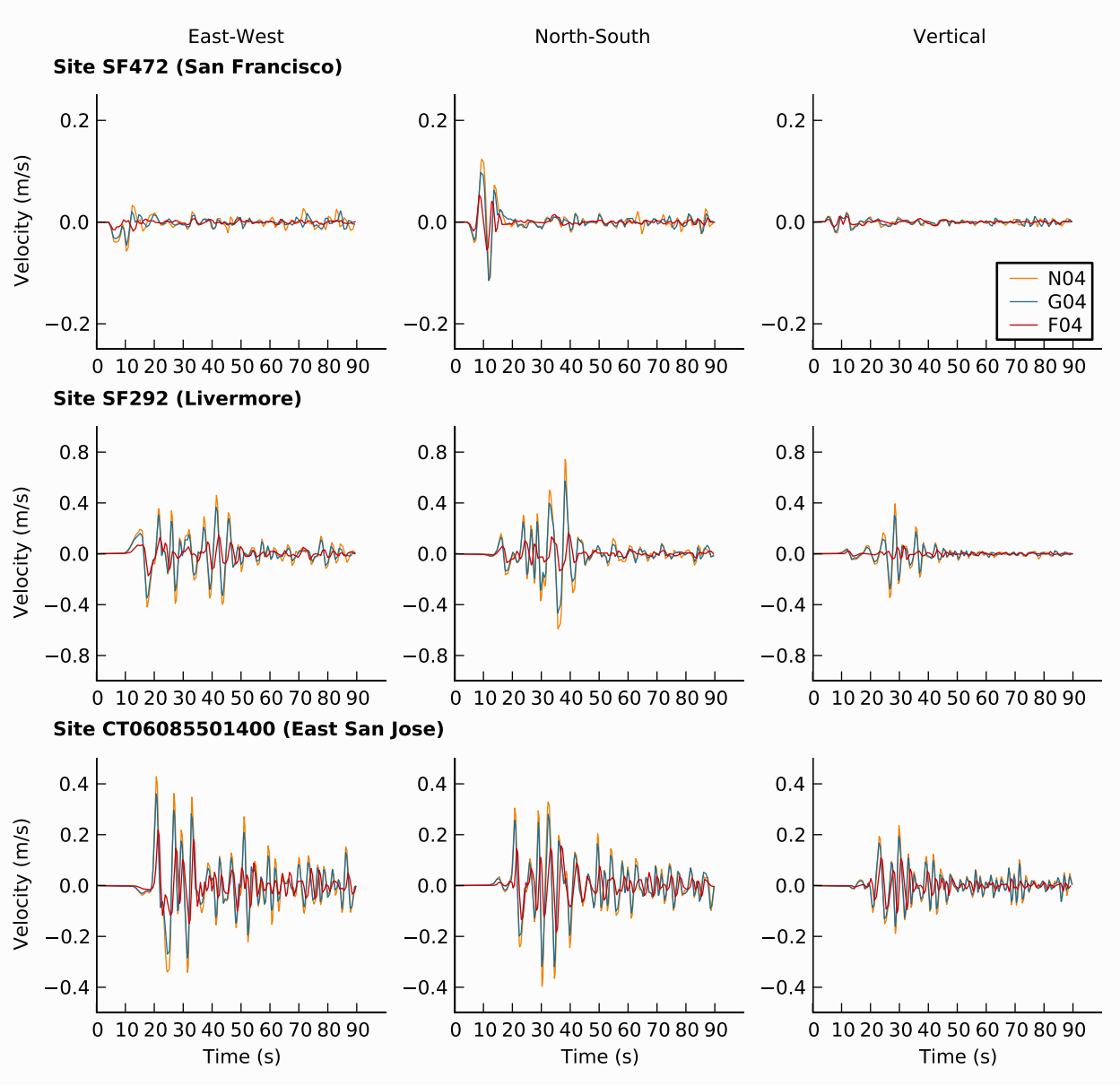

Figure 15. Velocity waveforms from Aagaard's long-period (T > 2.0 s) simulations of three scenario earthquakes with different vertical gradients in the slip distribution in creeping regions. The scenarios are identified by the slip distributions and include HS+HN N04, HS+HN G04 HypoO, and HS+HN F04. Creep reduces the coseismic slip in creeping regions, which lowers the magnitude and decreases the efficiency of radiating surface waves.

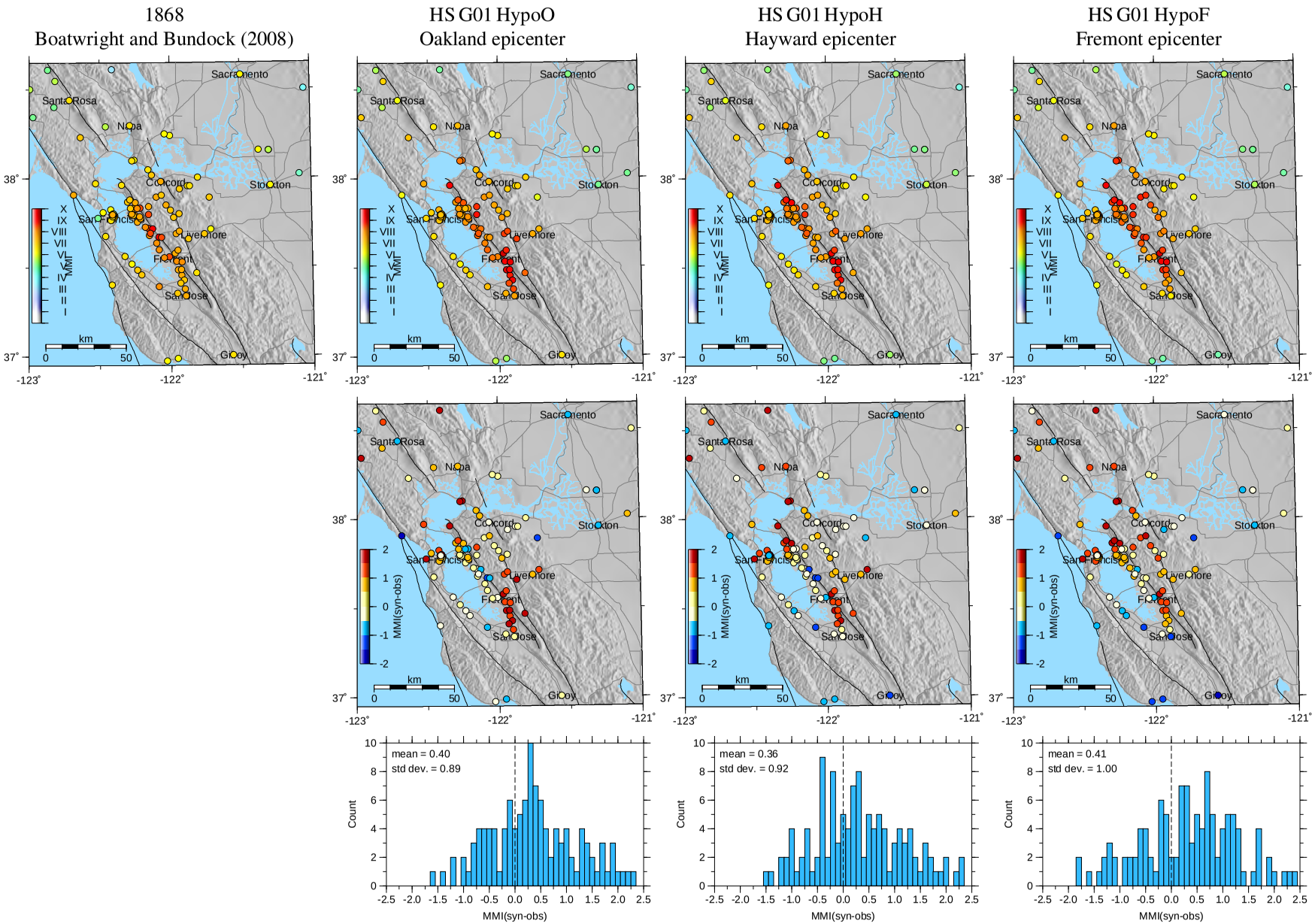

Figure 16. Comparison of MMI from Graves's broadband simulations of Hayward South scenario earthquakes with Boatwright and Bundock's compilation from the 1868 earthquake with the residuals for the synthetics shown in the bottom two rows. The bilateral rupture gives the lowest mean residual.

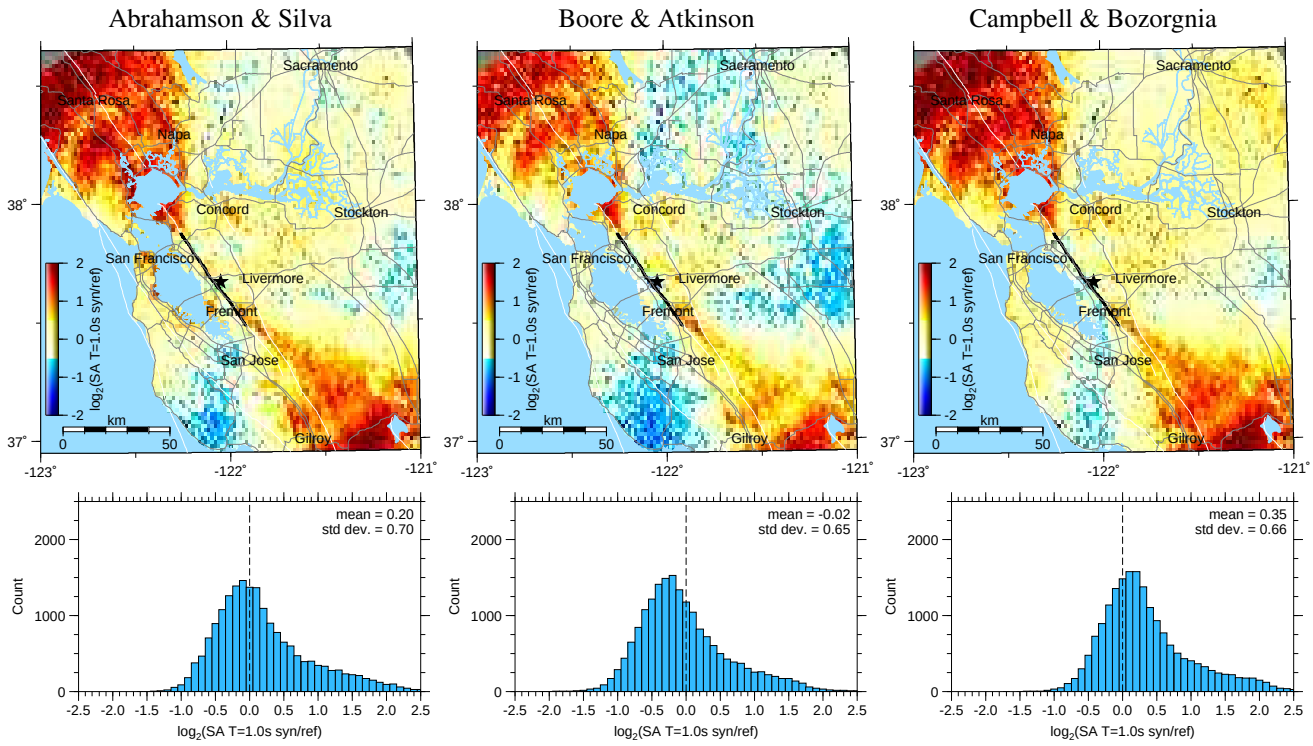

Figure 17. Comparison of spectral acceleration (SA) at 1.0 s from Graves's broadband (T > 0.1 s) simulation of scenario HS G01 HypoH with the Abrahamson and Silva, Boore and Atkinson, and Campbell and Bozorgnia NGA ground-motion prediction equations. Residuals are low along the length of the rupture and perpendicular to the fault. The simulation predicts higher spectral accelerations off the ends of the rupture due to rupture directivity, which is not explicitly included in the NGA models.

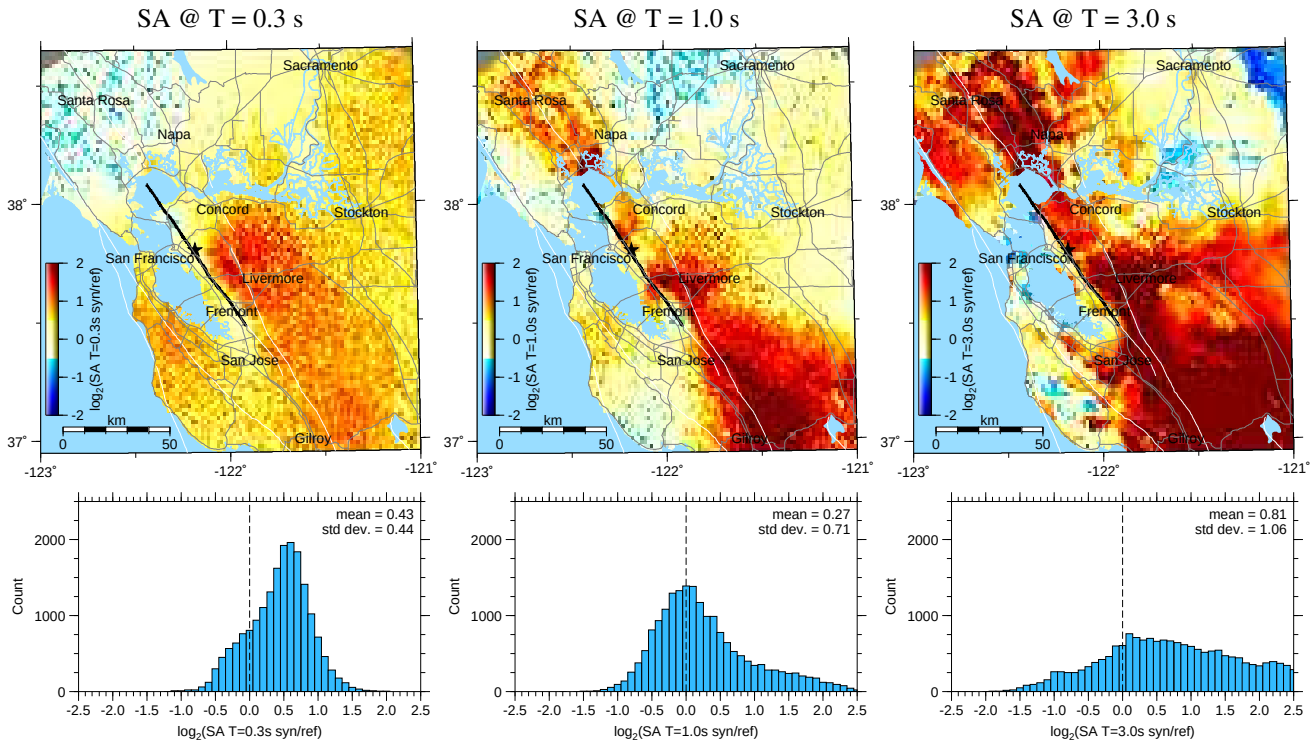

Figure 18. Comparison of spectral acceleration at 0.3 s, 1.0 s, and 3.0 s from Graves's broadband ($T > 0.1$ s) simulation of scenario HS+HN G04 HypoO with the Boore and Atkinson NGA ground-motion prediction equations. Residuals are generally low along the length of the rupture and perpendicular to the fault. The simulation predicts higher spectral accelerations off the ends of the rupture due to rupture directivity, especially at periods of 1.0 s and longer. The NGA models do not explicitly include directivity effects.

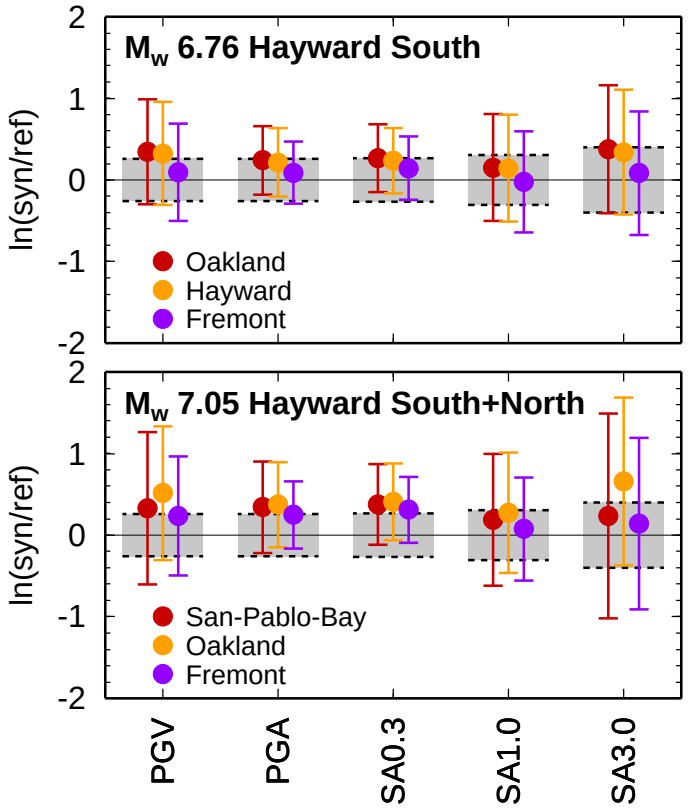

Figure 19. Summary of of the median residuals and variances for Graves's six broadband (T > 0.1 s) simulations of six scenario earthquakes averaged across the Abrahamson and Silva, Boore and Atkinson, and Campbell and Bozorgnia NGA ground-motion prediction equations. The gray shaded regions indicate the one standard deviation inter-event variability in the NGA relations. The average median residuals are within one standard deviation in most cases, indicating strong consistency between the 3-D ground-motion synthetics and the NGA relations.

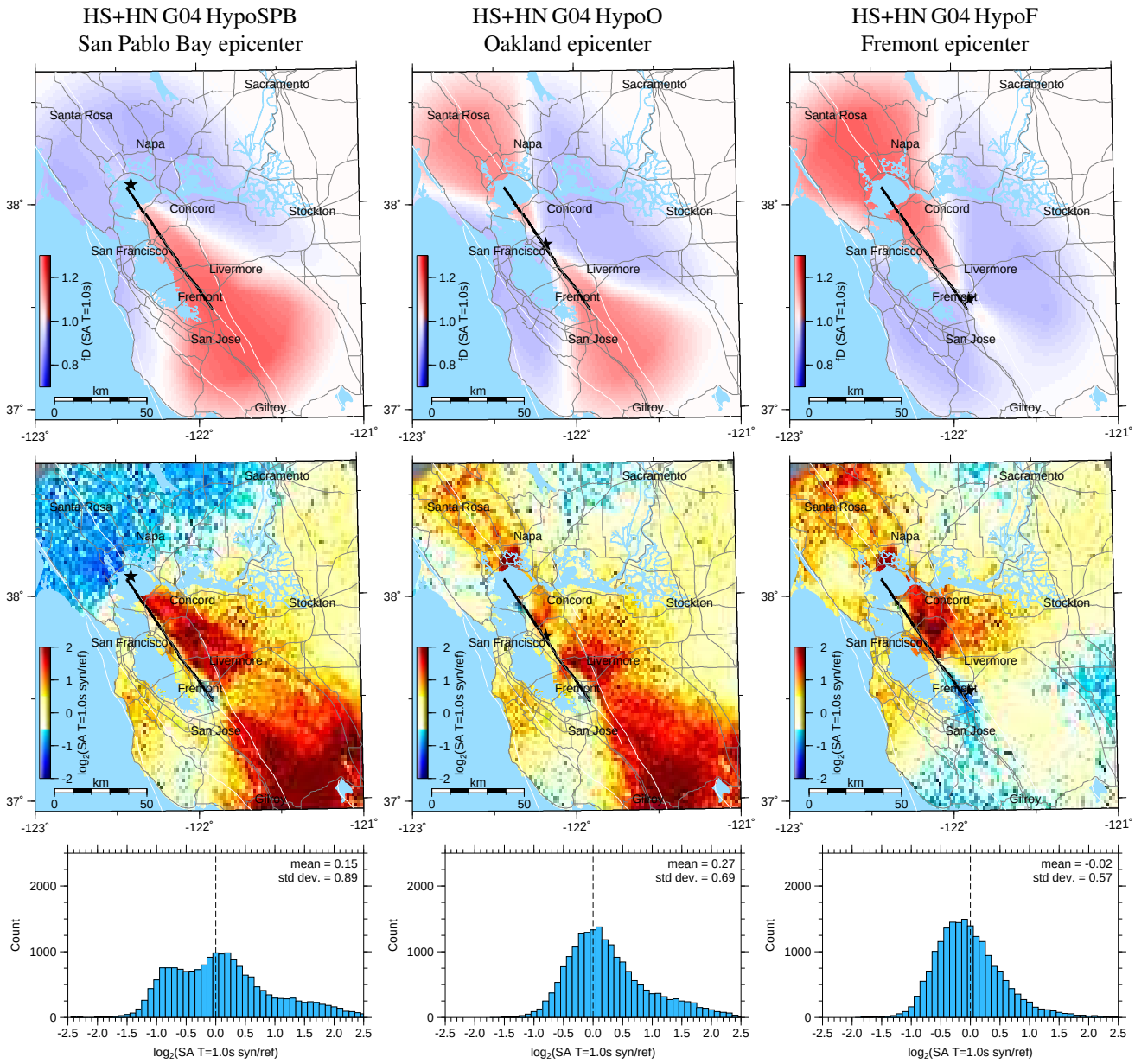

Figure 20. Comparison of spectral acceleration at 1.0 s from Graves's broadband (T > 0.1 s) simulations of scenario earthquakes with the Boore and Atkinson NGA ground-motion prediction equations (bottom two rows) adjusted by the Spudich-Chiou directivity correction (shown in the top row). The black line indicates the rupture and the black star identifies the epicenter. The directivity correction leads to a slight decrease in the standard deviation of the residuals. The 3-D simulations predict stronger directivity and extend it to greater distances than that predicted by the Spudich-Chiou directivity model.

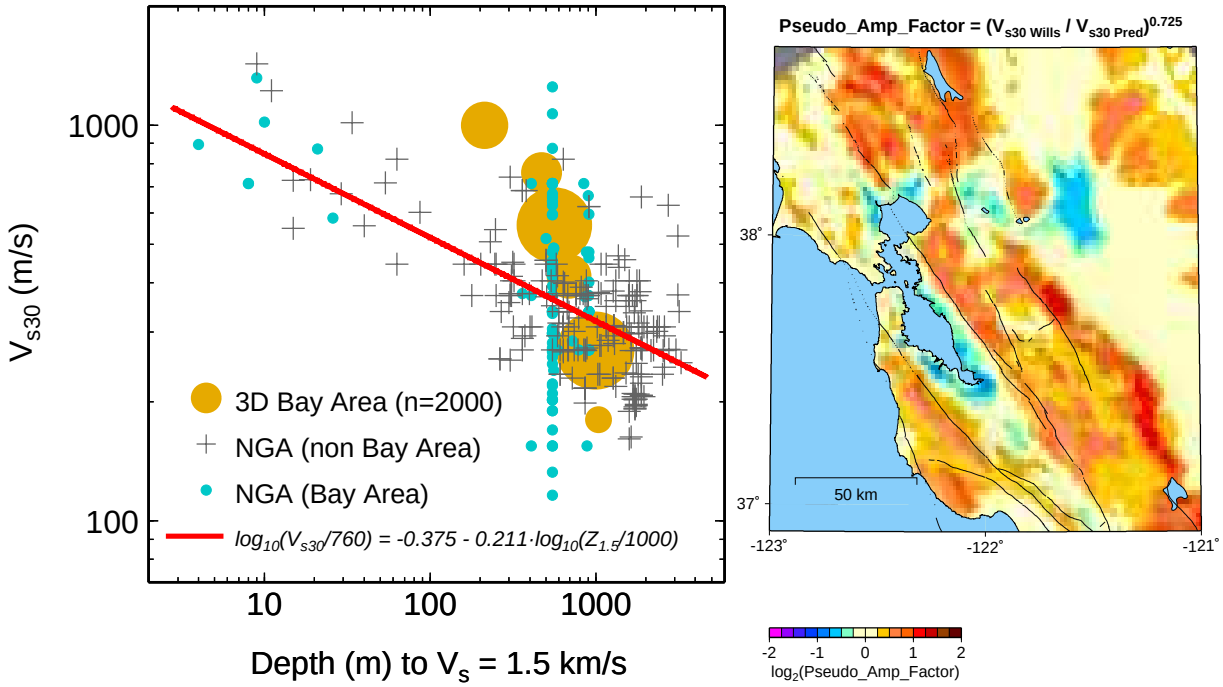

Figure 21. The left panel compares the correlation between Vs30 and depth to the 1.5 km/s isosurface for the USGS 3-D Bay Area Velocity Model with sites in the NGA ground-motion database. Sites in the San Francisco Bay area do not exhibit the same correlation as those in the NGA database as a whole. The right panel shows a map of the amplification correction factor that attempts to capture the potential differences in spectral amplitude predicted by the Boore and Atkinson NGA model with those expected based on the depth to the Vs 1.5 km/s isosurface.